Evaluation of Single-Molecule Magnetic Properties and Surface Structure of Terbium Porphyrin Double-Dekcker Complexes

Tomoko Inose

2015

Deparment of Chemistry, Graduate School of Science
Osaka University

Acknowledgment

This thesis presents the research that the author performed at Graduate School of Science, Osaka University from 2010 to 2015 under direction of Professor Takuji Ogawa. First of all I would like to express my sincere gratitude to Professor Takuji Ogawa for his continuing guidance, many helpful suggestion and warm encouragement. I had a precious experience for discussions, flexibility, and understanding. Special thanks to Professor Hirofumi Tanaka in Kyusyu Institute of Technology and Professor Daisuke Tanaka in Kwansei-gakuin University for their numerous helpful suggestions and many kind help for my experiments.

I would like to thank Mr. Naoya Inazumi for the measurement of NMR and Mr. Ken-ichi Iijima and Ms. Tomomi Hirai for elemental analysis. I would also like to thank Dr. Akihiro Ito for the measurement of mass spectra and Mr. Kazushi Kawamura for the measurement of IR spectra and Raman spectra.

I gratefully acknowledge JSPS Research Fellowship for Young Scientists and the JSPS International Training Program (ITP) for the financial support of my research.

I am grateful to my collaborators in Japan and Belgium. I would like to thank Prof. Naoto Ishikawa, Dr. Takamitsu Fukuda, and Mr. Shohei Sakaue in Osaka University for their helpful discussions for magnetic measurement. I want to say special thanks to Prof. Steven De Feyter and Dr. Oleksandr Ivasenko in KU Leuven for the STM measurement and many helpful discussions. Also thanks to all staffs and students in the laboratory for the warm welcome in Belgium and the many kindness. I would like to thank Prof. Toshi Nagata in Meijo University for performing the MM calculation and many valuable discussions. I would also like to express my gratitude to Prof. Yoshito Tobe and Dr. Kazukuni Tahara in Osaka University for the synthesis of the DBA derivatives and fruitful discussions. I would like to thank Dr. Tatsuhiko Ohto for kind discussion about DFT Calculation. I am grateful for Prof. Tadahiro Komeda, Dr. Liu Jie, Dr. Puneet Mishra, Ms. Mizu Kajihara, Mr. Qi Zhikun, and Mr. Ryuki Sato for many helpful discussions and experiments for UHV-STM. It would be much more difficult to complete my thesis without their kind support.

I wish to thank all the members of Ogawa laboratory for their heartfelt friendship and helpful discussions. Especially, I would like to thank Mr. Yusuke Ohta, Mr. Nobuto Sumitani, Mr. Satsuki Shimono, Ms. Sunri Lee, Mr. Naoya Sakata, Mr. Takashi Sakai, Mr. Yudai Yamamoto, and Ms. Yukiko Okimura, a member of SMM group, and Mr. Minoru Fukumori, Ms. Murni Hadayani, Mr. Takashi Tamaki, and Mr. Ahmed Ibrahim Ahmed for valuable discussions and friendly competition. I would also like to thank Ms. Ryoko Takeda and Ms. Takako Abe, a secretary of Ogawa laboratory.

Finally, I express my special thanks to my parents and all my family for constant care and encouragement.

Tomoko Inose

Department of Chemistry, Graduate School of Science

Osaka University

September, 2015

Contents

Chapter I General Introduction

Molecular spintronics, a technology developing both charge and spin degrees of freedom at the single-molecule scale, attracts increasing attention as a promising topic toward single-molecule magnets at both the fundamental and applied levels of study.[1] One of the most promising materials in the field of molecular spintronics is single-molecule magnets (SMMs).[2-11] SMMs can behave like nanoscale magnetic molecules in one molecule because of the large magnetic anisotropy. The major design strategy first employed for SMM studies was to use polymetallic transition-metal complexes with strong intramolecular exchange coupling. Longer magnetization relaxation times can be induced due to their large anisotropy and high-spin ground state. Since 2003, however, lanthanide-based SMMs have been getting a lot more attention as attractive molecules because of the extremely large anisotropy of lanthanide ions.[12] Among many lanthanide complexes which show SMM properties, the family of phthalocyanine (Pc)-based Tb^{III} double-decker compounds ($TbPc_2$) show comparatively higher blocking temperatures.[13]

Previously, the main topic in this field is the study to design new SMMs which show higher blocking temperature, and many SMMs with transition metals or lanthanide ions have been reported.[2,4-7,11,13] As another interesting topic of SMMs, SMM behavior on a surface has been studied with enthusiasm,[14-17] especially nanocarbon/SMM composites have great attention in these days.[18,19] In this study, the idea of molecular spin-valve is very important and the magnetic state of SMMs by electrical signals has already been successfully detected. Nanocarbon/SMM composites seem great potential to realize future molecular spintronic devices like high-density memory devices. On the other hand there are a few studies about precise molecular alignment on a surface.[20] To achieve the most appropriate molecular spintronic devices, investigating supramolecular structure of SMMs and controlling the SMM properties on a surface at molecular level is very important.

Among many powerful tools to investigate surface structures, scanning tunneling microscopy (STM) is superior for measuring surface structure at single-molecule level or

single-atom level.[21-38] In STM study, it is possible not only to observe supramolecular structure on a surface with high resolution image but also to manipulate the electronic state of a molecular at single-molecule level by injecting electrons from an STM tip.[21-30] Indeed the electronic structure of $TbPc_2$ on an Au(111) has already been successfully changed from an anionic form to a radical form at a single-molecule level precisely under ultra high vaccum condition by injecting tunneling electrons.[39] STM is one of the very important and advantageous tools to investigate surface behavior of molecules including SMMs.

On the basis of these recent SMM works, new results described from Chapter II to Chapter VI were obtained in my study. Through all chapters, porphyrin-based Tb^{III} double-decker complexes ($TbPor_2$) were used. Because porphyrin can be chemically modified easier than phthalocyanine, it is expected to find new attractive SMM functions. The main results in this thesis are below.

1) Proton-induced switching of the magnetic property of SMMs in bulk state.
2) Fabricating stable 2D supramolecular structures of SMMs on a carbon surface
3) Molecular manipulation of a porphyrin-Tb^{III} double-decker complex on Au(111) at single-molecule level.

In previous studies, the memory function of $TbPc_2$ SMMs was observed by detecting magnetic property of nanocarbon/$TbPc_2$ SMMs composites. This study can use as a reading function of memory devices. On the other hand writing function is also an essential function to realize memory devices of SMMs although there are no reports about writing function of SMMs. Here I proposed one direction to realize writing function of SMMs for future molecular memory devices.

In Chapter II both a protonated form and an anionic form tetraphenylporphyrin-Tb^{III} double-decker complexes were isolated to realize drastic magnetic switching of SMMs. Magnetic switching is very important for the writings function of memory devices. In Chapter III a porphyrin double-decker complex with quinone dyad was designed to occur proton coupled electron transfer (PCET). If PCET occurs, SMM switching in solid state can be achieved. Energy barrier between the ground state of both before and after PCET and transition

state was estimated from DFT calculations. In Chapter IV, an octaethyporphyrin-Tb^{III} double-decker complex with ethyl groups was designed to observe supramolecular structure of SMMs on a surface. Octaethylporphyrin double-decker complexes with three different electronic structures were synthesized and the SMM property was measured. Furthermore stable ordered 2D supramolecular structures of complexes with three electronics structures on a carbon surface were observed by STM measurement. In Chapter V, one method to fabricate new 2D supramolecular structure of SMMs by using a template molecule was suggested. Realizing many kinds of 2D supramolecular structures of SMMs is very important to find the most suitable 2D design for molecular spintronics devices. In Chapter VI, single molecular manipulation of octaethylporphyrin double-decker complexes on Au(111) was demonstrated by STM. The electronic state of an octaethylporphyrin double-decker complex was changed at sinlge-molecule level from a protonated form which does not show the SMM property to a radical form which show the SMM property. From this study basic perception to realize SMM switching on a surface was suggested.

More detail about keywords in this thesis is described below.

Single-Molecule Magnets (SMMs)

Single-molecule magnets (SMMs) seem particularly attractive and potential molecules because of their unique energy barrier to slow relaxation of the magnetization at low temperatures. SMMs have inner magnetic cores that are surrounded by organic ligands. The famous Mn_{12} cluster is the first reported SMMs by R. Sessoli *et al*. in 1993.[8] The magnetic SMM magnetic properties can be written by a spin Hamiltonian below,

$$H = DS^2_z + E(S^2_x - S^2_y) + g\mu_B\mu_0\mathbf{S}\cdot\mathbf{H} \quad (1)$$

where S_x, S_y, and S_z are the spin components, D is the parameter which means the zero-field splitting, E is the constant number of magnetic anisotropy, and $g\mu_B\mu_0\mathbf{S}\cdot\mathbf{H}$ means the Zeeman energy when the magnetic field **H** is applied. SMMs have $D < 0$ and magnetic anisotropy along S_z. When an energy barrier between two spin states ("spin-up" $S_z = S$ and "spin-down" $S_z = -S$) exists, it means a double-well potential is formed by an axial zero-field splitting of the SMMs. The height of the energy barrier U_{eff} is written by $U_{eff} = |D|S^2_z$. The spin must overcome U_{eff} to reverse the magnetization. Since the first SMM was reported, strongly-coupled transition metal clasters with high-spin were regarded as the most promising molecules and many studies are still reported in this field now.[40]

On the other hand, first lanthanide based SMMs –Tb^{III} based phthalocyanine (Pc) sandwich type complex [$TbPc_2$] – with a higher blocking temperature was reported in 2003.[12] Since then many mononuclear complexes which show SMM property have been reported.[7]

Lanthanide SMMs

Since 2003, SMMs based on the lanthanides tale on a growing importance that have high potential to realize large spin values in a well isolated ground state. In 3d transition metals, the main effect to ligand field is spin-orbit coupling. On the other hand bistable ground state of lanthanide SMMs (Ln-SMMs) is quite different from transition metal SMMs. The large and unquenched orbital contribution to the magnetic moment exist for lanthanide ions, and ligand field is considered as a small but non-negligible perturbation. In case of SMMs with transition metal, ground-state bistability is doped on the total spin S and the ensuring $[2S + 1]$ m_S substates.[7] Contrary to transition metal SMMs, ground-state bistability of Ln-SMMs comes from the $[2J + 1]$ m_J microstates within the spin-orbit-coupled ground term, ${}^{2S+1}L_J$.[7,12] Furthermore the ground state of Ln-SMMs have a large m_J value, which gives an appreciable magnetic moment. Because of these reasons, the most common used lanthanide ions in SMMs are Tb^{III}, Dy^{III}, Er^{III}, and Ho^{III}. Especially among them, the electronic structures of Tb^{III} and Dy^{III} ions have large and strong anisotropy because 4f orbitals depend on angle strongly. Furthermore Tb^{III}-SMMs show some of the larger U_{eff} values than that of Dy^{III}-SMMs because magnetic anisotropy and Δm_J gaps of Tb^{III} is larger than Dy^{III}. On the other hand, the number of reported Tb^{III}-SMMs is fewer than Dy^{III}-SMMs because Tb^{III} is a non-Kramers' ion. In case of non-Kyamers' ion, axial anisotropy of the ligand field is very important to realize bistability of ground-state.[7]

The very basic characterized method for most of the SMMs in bulk state is the measurement by SQUID magnetometers. One of the certain methods to identify an SMM is to investigate the variation of in-phase magnetic susceptibility (χ') and out-of-phase magnetic susceptibility (χ") with temperature at several different frequencies. When the spin flip is disturbed, the gradual increasing of χ" as the temperature decreases and decreasing of χ" at lower temperature after reaching the maximum is observed. The χ"(ν) (ν; the frequency of the ac field) isotherms give the most certain anisotropy energy barrier, U_{eff}. An average relaxation time τ can be gotten from each χ"(ν) curve. Moreover the relationship between τ and temperature is written by Arrhenius-type relationship:

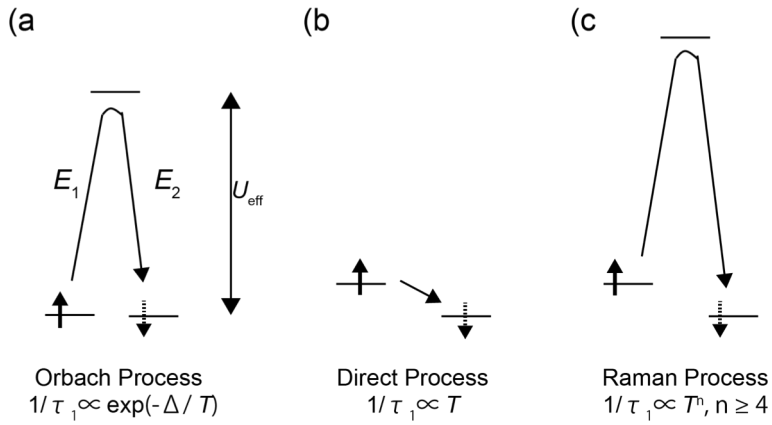

Figure 1. Mechanisms of three kinds of magnetic relaxation processes caused by spin-phonon coupling and their temperature dependence.

$$\tau = \tau_0 \exp(U_{eff} / k_B T) \quad (2)$$

It is possible to determine the anisotropy barrier U_{eff} from equation (2). The magnetization in the SMM relaxes through a thermally assisted mechanism. It is known that there are several kinds of relaxation process – Orbach process, direct process, and Raman process for Ln-SMMs (Figure 1).[3,7] In Orbach process, energy difference between two low-lying degenerate states and an excited state of the lanthanide ion can be described by U_{eff}. (Figure 1(a)). When the lanthanide ion in the ground state adsorbs a phonon whose frequency is equivalent to U_{eff}, the low-lying state with $m_J = + J$ can change to $m_J = - J$ through the excited state. This temperature dependent process results in magnetic relaxation. As other possible relaxation processes, the direct process and the Raman process can occur. In these relaxation processes, a spin flip is induced by phonons within the two degenerate ground states (Figure 1 (b), (c)).

For majority number of Ln-SMMs, the Arrhenius plots at lower temperature range often show a series of continuous data points and $\ln\tau$ is unrelated to the temperature. To take terbium as an example, the zero gradient in an Arrhenius plot prove for the direct magnetic relaxation form $m_J = + 6$ to $m_J = - 6$, through quantum tunneling of magnetization (QTM). Sometimes Arrhenuis plot shows two processes in the plot region and it means the thermal relaxation processes and the QTM mechanisms can happen simultaneously.

It is common matter that same SMM shows a number of thermally activated mechanisms and it can also happen that almost all magnetic relaxation processes occur via QTM.

Investigating multiple relaxation process of SMMs is comparatively easy by fitting of the ac magnetic susceptibility data including χ' vs. χ" (Cole-Cole plot).

Phthalocyanine (Pc) based Tb^{III} double-decker complexes ($TbPc_2$)

The family of mononuclear complexes $[TbPc_2]^n$, $[DyPc_2]^n$, $[HoPc_2]^n$ (n = -1, 0, +1) was reported as first lanthanide SMMs, especially $TbPc_2$ and its derivatives remain show the highest anisotropy barriers (Figure 2(a)).[12,41] The double-decker structure with $[LnPc_2]^n$ usually shows a D_{4d}-symmetric square-antiprismatic phthlocyaninate ligand or substituted analogue. The possible electronic state of the molecule can be an anion, uncharged, and a cation by the specific redox active properties.[12,13]

The in-phase and the out-of-phase magnetic susceptibility of polycrystalline powder sample of $[TbPc_2]^-$ showed temperature dependence in a small ac magnetic field of 3.5 G oscillating at 10, 100, and 997 Hz. To prove an intrinsic molecular property of the slow magnetization relaxation, sample of $[LnPc_2]^-$ doped in diamagnetic host $[YPc_2]^-$ with the molar ratio, $[TbPc_2]^-$: $[YPc_2]^-$ = 1 : 4 was also measured.[42] Yttrium(III) with very similar ionic radius to that of the midlate lanthanides was selected because the slow dynamics of the magnetization can be lead by diamagnetic host lattices. In dilute sample, the susceptibility curves was shifted to higher temperatures. It means the dipolar interactions between nearest neighbor Tb^{III} ions is removed and a slowing of the magnetization reversal rate occurs. This indicates that the slow magnetic relaxation in $[TbPc_2]^-$ is a specific property of this molecule.

Low-lying electronic structure of $[LnPc_2]^-$ was determined by the simulataneous least squares fitting of both paramagnetic ^{1}H-NMR shifts ($\Delta\delta$) and magnetic susceptibility data (χ_M). In the $[TbPc_2]^-$, it was assigned that $J_z = \pm 6$ was the lowest substates. The values of $J_z = \pm 6$ are

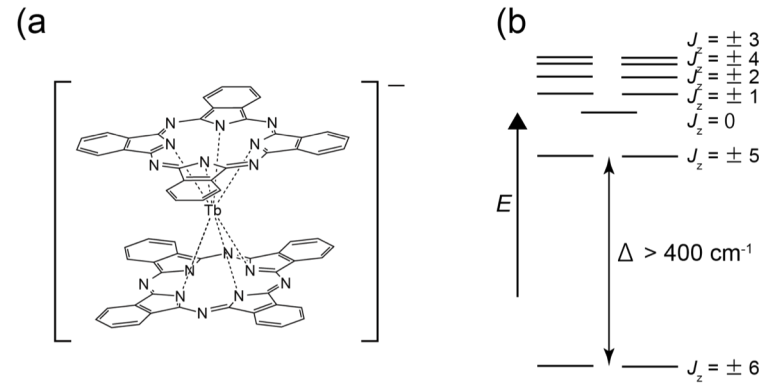

Figure 2. (a) Structure of $[TbPc_2]^-$. (b)Energy diagram for the ground multiplets of $[TbPc_2]^-$.

the maximum ("spin-up" state) and minimum ("spin-down" state) values in the $J = 6$ ground multiplet (Figure 2).[43] There are more than 400 cm^{-1} energy separation between $J = 6$ ground multiplet and the rest of the substates. In case the relaxation process occurs one by one from J_z to $J_z = \pm 1$ states, transition from the ground state of $J_z = 6$ to the next energy state of $J_z = 5$ (or from -6 to -5), can be the "rate-determining step" because of the large energy barrier (Figure 2(b)). Arrhenius analysis of $[TbPc_2]^-$ revealed Orbach process was dominant from 25 K to 40 K. Estimated value of the energy barrier of $[TbPc_2]^-$ which the Orbach process occurs was 2.6×10^2 cm^{-1}. This value can be a support data that the Orbach process is the dominant relaxation process because it is close to the magnitude of the energy barrier between $J_z = 6$ and $J_z = 5$.

Molecular Spin-Valve

Recently molecular spintronics using SMMs shows a significant improvement that make a suggestion to manipulate the magnetic and quantum information stored in these molecules.[1,18,19,44,45] One of the interesting researches in this field is investigation of electrical conductivity of $TbPc_2$ derivatives on a surface at the single-molecule level by nanogap electrodes and scanning tunneling spectroscopy (STS).[39,44] Other attractive approach in the study of molecular spintronics of SMMs is the ideas of molecular spin-valve.[19,20,45] Figure 3 shows the image of molecular spin-valve. If only one molecular magnet exist between gold electrodes, detecting spin state (up-spin or down-spin) of magnetic molecule is difficult (Figure 3(a)). Figure 3(b) shows parallel configuration of the two molecular magnets between gold electrodes. Molecular magnetization does not affect most of the spin-up carriers, on the other hand a few spin-down carriers are partially reflected back. This configuration leads to higher conductance. Figure 3(c) shows anti-parallel configuration of the two molecular magnets

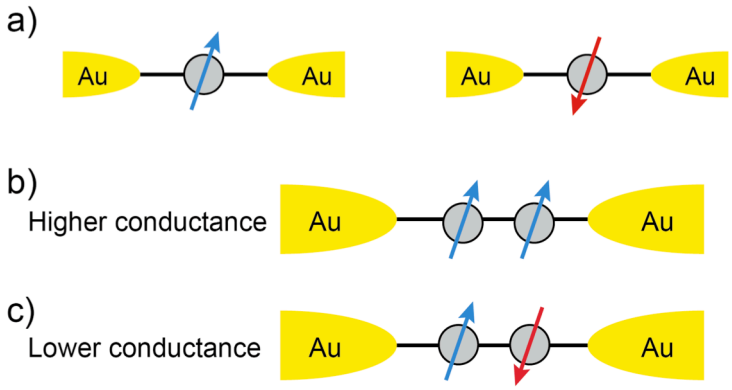

Figure 3. Spin valve systems of molecular magnets. Blue and red arrows is the magnetizations of molecules.

between gold electrodes. When electrons transmit from a left gold electrode to a right gold electrode, the different poralized molecule disrupts the transmission of most parts of spin-up electrons. In case of transmission of spin-down electrons is totally the opposite. This configuration results in lower conductance.

The attractive spin-valve materials in spintronic field recently is nanocarbon/SMM composites (Figure 4). Nanocarbon/SMM composites –$TbPc_2$ derivatives on nanocarbon materials like graphene sheet or carbon nanotube- contain at least two SMM centers on the graphene sheet or carbon nanotube; the relative direction of the SMM magnetic moments strongly affect the conductance of the electrons passing through the nanocarbon material. Indeed nanocarbon/SMM composites have received considerable attention in recent years and the magnetic state of SMMs by electrical signals have already been successfully detected. Thus the idea of molecular spin-valve has great potential for future spintornic devices, especially high-density data storage and so on.

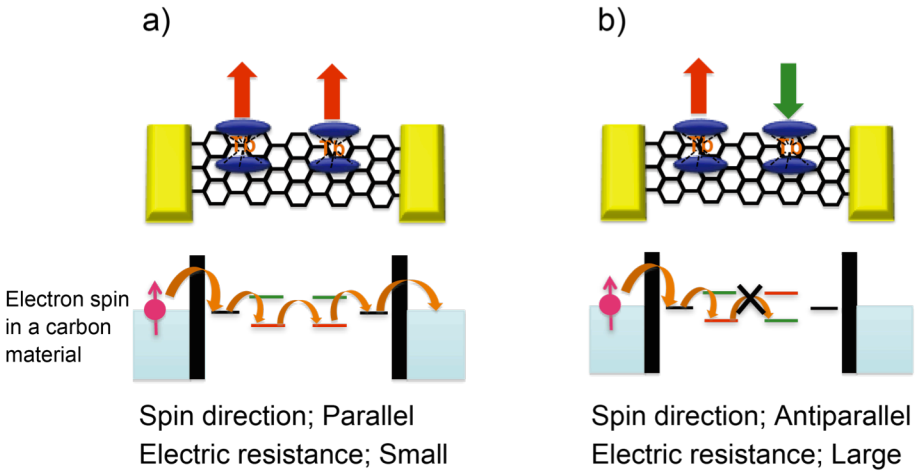

Figure 4. Schematic representation of nanocarbon/SMM composites. (a) With increasing magnetics field, it leads to a parallel configuration of the spinvalve, and this configuration leads to high conductance. (b) When one molecule switches, this leads to an antiparallel configuration of the spin valve with highest conductance.

Scanning Tunneling Microscopy (STM)

Scanning tunneling microscopy (STM) was devised by Binnig and Rohrer *et al*. in 1982.[22] A STM can draw topography mapping and the DOS of a surface. A detailed 2 dimensional (2D) supramolecular structure on a surface at single molecular level or single atom level can be observed by high-quality STM. Figure 5 shows a schematic of STM measurement setup. In STM measurement, we use very sharp metal tip to probe a surface. The tunneling current between tip and surface substrate is detected as physical quantity. The position of a tip is controlled to keep the current value is constant and scan the surface. By this mechanism it is possible to draw topography of a surface and we can observe supramolecular structures on a surface.

In case of the sample bias is sufficiently small, the tunneling current is described by following equation,

$$I_t \propto V \cdot n_t(E_f) \cdot \exp(2\kappa R)\, n_s(E_f, \boldsymbol{r}_0) \tag{3}$$

Here, $n_t(E_f)$ is density of states (DOS) of Fermi energy of STM tip. $n_s(E_f, \boldsymbol{r}_0)$ means DOS of sample side when the position of the tip is r_0 and it can be described by following equation,

$$n_s(E_f, \boldsymbol{r}_0) = \Sigma\, |\psi_v(\boldsymbol{r}_0)|^2 \delta(E_v - E_f)$$

κ is the decay of the wave function in the potential barrier and described by $\kappa = 2m\phi/\hbar$, and ϕ is the potential barrier. These equations show that the tunneling current describes DOS distribution around Fermi level of a sample at the center position of a tip. Figure 6 shows the energy state of tip-sample junction. When the bias voltage is applied to the sample, the Fermi

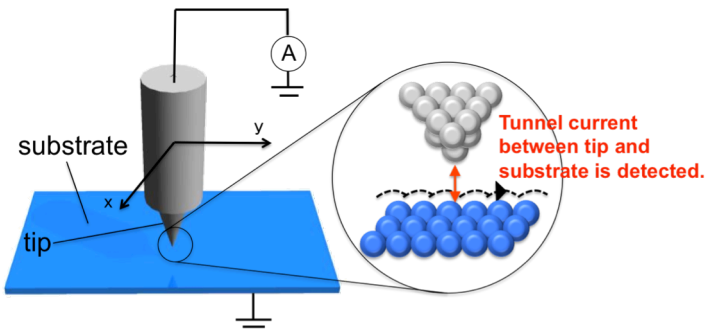

Figure 5. Schematic of STM measurement setup.

level of a sample shifts against the Fermi level of a tip. When zero bias is applied to a sample (V_s = 0, equilibrium state) in Fig. 6 (a), the tunneling current is zero. When the positive sample bias is applied to a sample (V_s < 0) in Fig. 6 (b), tunneling electrons flow from the highest occupied molecular orbital (HOMO) state of a sample into the unoccupied state (LUMO state) of a tip. On the contrary, when negative sample bias is applied to a sample (V_s > 0) in Fig. 6 (c), tunneling electrons flow from the LUMO state of a sample into the occupied state (HOMO state) of a tip. In this way STM can draw the precise 2D space distribution image of HOMO state or LUMO state of a surface.

Scanning tunneling spectroscopy (STS)

STM measurement can obtain the information of electronic states of molecules on a surface by sweeping the bias voltage and measuring the corresponding tunneling current. The high resolution of STM can reveal the electronic states of the local structures and vibrational modes of single molecule on a surface. Such attractive measurement can be achieved only by using STM.

Here we use a model of the tunneling junction depicted in Fig. 6. In this model, a vacuum gap exists between a tip and a metallic substrate, and tip-substrate distance "d" is less than 1 nm. When molecules are adsorbed on a metal substrate, hybridization of molecular orbitals and conduction electrons of a metal surface was observed. This hybridization causes resonant states and the states lead to a broadened DOS of molecules. When a negative bias voltage V_s is applied to the sample, the Fermi level of the sample increase against the Fermi level of the tip (Figure 6(c)). In this case the tunneling current is written by the following equation,

$$I(V) \propto \int_{E_f}^{E_f + eV_s} \rho(E)\mathrm{dE}$$

Here, $\rho(E)$ means the DOS of the sample and we can know the tunneling current is proportional to the integral of the DOS of the sample between the Fermi level (E = 0) and E = eV_s. Furthermore there is a proportional relationship between dI/dV and the DOS of the resonant states of the sample as shown in following equation,

$$\mathrm{d}I/\mathrm{d}V \propto \rho(E)$$

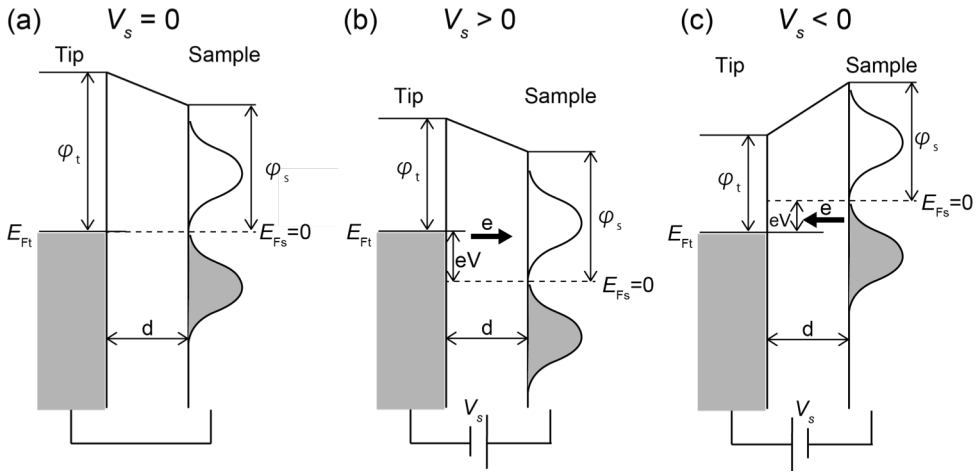

Figure 6. Energy state of tip-sample junction. (a) No bias is applied ($V_s = 0$)., (b) Positive sample bias is applied ($V_s > 0$)., (c) Negative sample bias is applied ($V_s < 0$).

If molecules exist under the tip, it is expected that specific dI/dV can be observed, which is attributed to the molecular orbitals. This is called scanning tunneling spectroscopy (STS) and can detect the molecular orbitals of individual molecules on a surface.[46-49]

Inelastic tunneling spectroscopy (IETS)

Inelastic electron tunneling spectroscopy (IETS) is basically one of the electron spectroscopy measurement same as STS measurement. Vibrational spectrum of molecules between tip-substrate junction can be detected by IETS.[50-54]

An elastic tunneling shows a linear relationship between the tunneling current (I) and the bias voltage (V) on metallic surface. In case an electron passes through a molecule, a phonon or a molecular vibration with the energy of $\hbar\omega$ may be excited and finally the electron loses its energy (Figure 7(a)).[55] This process occurs only when the energy of electrons exceeds the vibrational energy $\hbar\omega$ because of the dissipation of its energy. The appearance of the new channel by this inelastic process leads to the increment of the conductance. The change of this conductance is usually very small and it is difficult to detect it directly in I-V curves. On the other hand peaks with the Gaussian shape can be observed in the second derivative d^2I/dV^2. The simplified schematic of the tunneling spectrum is shown in Figure 7(b).

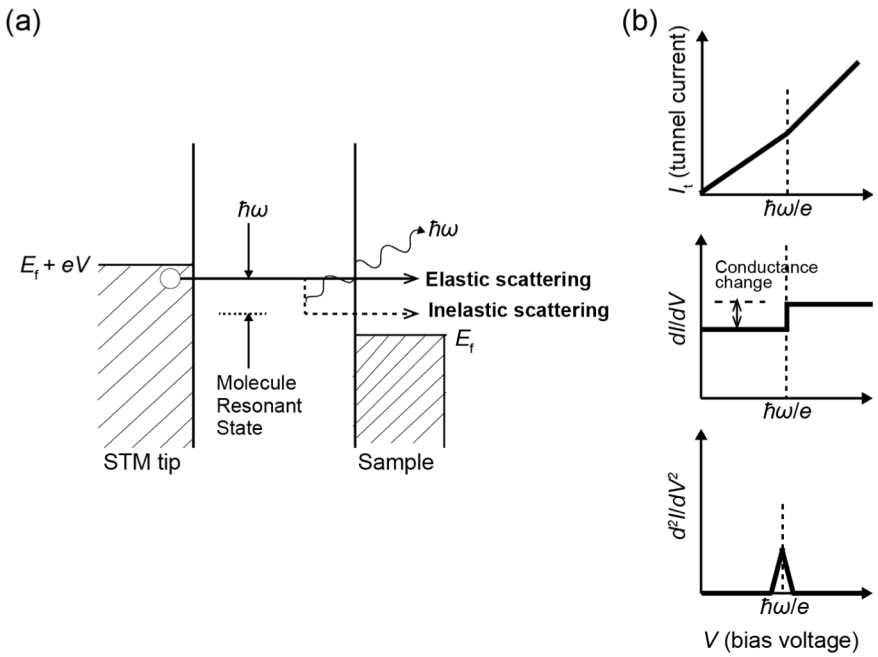

Figure 7. (a) Energy diagram of inelastic process by STM. (b) A typical tunneling spectra.

Kondo Effect

We can observe an exceptional phenomenon that an increase in resistance of some metals with the presence of magnetic impurities at low temperatures.[56] This phenomenon was discovered in 1930s and Jun Kondo successfully explained this resistance anomaly and reported the theory in 1964.[57] Today this theory is well known as the Kondo effect. The s-d exchange interaction between the magnetic moments of the impurity and conduction electrons is the cause of Kondo effect. At low temperature, the magnetic moments of the impurity are hampered by many conduction electrons around the impurity which are called Kondo cloud and singlet ground state (Kondo singlet) is formed (Figure 8 (a), (b)).[58] Because of this, the magnetic moments of the impurity disappear.

A spin singlet is the ground state of the conjugation system of the magnetic impurity and conduction electrons. The Kondo effect is based on strong electron-electron repulsion and Pauli exclusion principle. When a spin- 1/2 of impurity exists, conduction electron and the spin of the local moment make one pair, and this pair forms a singlet. Higher order tunneling processes have a potential to cause quenching of localized magnetic moment by a polarization of the delocalized conduction electrons. By these higher order processes, the quenching of the magnetic moment forms a new state whose total spin 0.

Only when a spin 1/2 of impurity and delocalized conduction electrons are coupled, the Kondo effect is observed. The detailed system of Kondo effect can be explained by the Anderson single-level impurity model. In this model one energy level is occupied by the magnetic impurity and this level exists at ε_0 (Figure 8(c)). Both the levels above (unoccupied state) and below (fully occupied with electrons) ε_0 do not contribute to the Kondo resonance. When the energy level of ε_0 exists under the Fermi level, the unpaired electron of the magnetic impurity is trapped. If additional energy does not exist, put the electron out of the impurity is impossible. However there are some possibilities that this transition of electron can occur through an exchange coupling by the uncertainty principle. By this, getting out of the impurity of the electron can occur and electron can move to the energy level of an electrode (Figure 8(d)). During the process, another conduction electron must come into the impurity to cover the

vacant (Figure 8(e)). The direction of the spin of this new electron has two possibilities of both spin-up and spin-down. The shielding of the local spin is caused by the coherent superposition and it produces the Kondo resonance.[58] We can use Kondo resonance to detect molecular spin on a surface.[39,59-62]

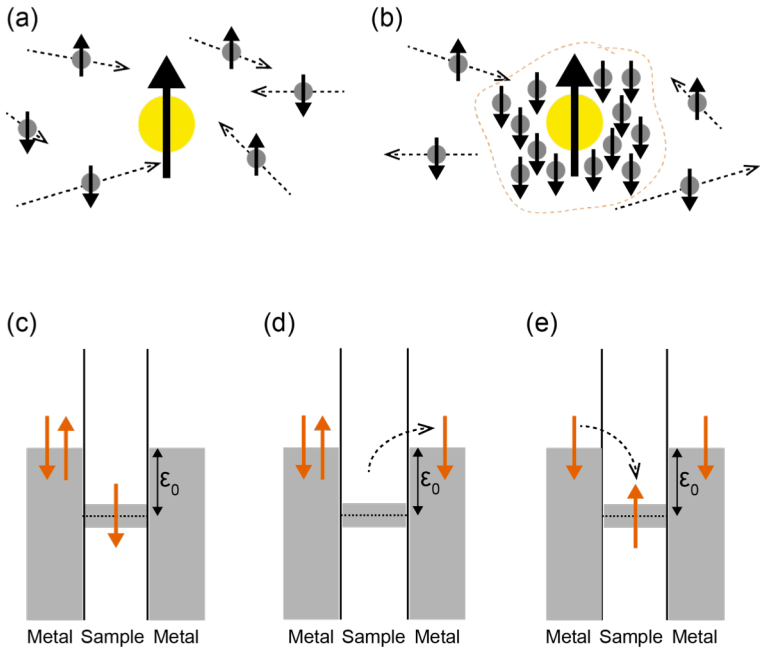

Figure 8. The relationship between the magnetic impurity and a sea of conduction electrons (a) $T > T_K$. (b) $T < T_K$ (Kondo cloud is formed). Mechanism of the observation of the Kondo resonance: (c) initial state, (d) intermediate state, (e) final state.

References

(1) Bogani, L.; Wernsdorfer, W. *Nat. Mater.* **2008**, *7*, 179.

(2) Christou, G.; Gatteschi, D.; Hendrickson, D. N.; Sessoli, R. *Mrs Bull* **2000**, *25*, 66.

(3) Dreiser, J. *J. Phys. Condens. Matter* **2015**, *27*, 183203.

(4) Habib, F.; Murugesu, M. *Chem. Soc. Rev.* **2013**, *42*, 3278.

(5) Miller, J. S.; Gatteschi, D. *Chem. Soc. Rev.* **2011**, *40*, 3065.

(6) Rinehart, J. D.; Long, J. R. *Chem. Sci.* **2011**, *2*, 2078.

(7) Woodruff, D. N.; Winpenny, R. E.; Layfield, R. A. *Chem. Rev.* **2013**, *113*, 5110.

(8) Sessoli, R.; Gatteschi, D.; Caneschi, A.; Novak, M. A. *Nature* **1993**, *365*, 141.

(9) Glaser, T. *Chem. Commun.* **2011**, *47*, 116.

(10) Sanvito, S. *Chem. Soc. Rev.* **2011**, *40*, 3336.

(11) Sorace, L.; Benelli, C.; Gatteschi, D. *Chem. Soc. Rev.* **2011**, *40*, 3092.

(12) Ishikawa, N.; Sugita, M.; Ishikawa, T.; Koshihara, S. Y.; Kaizu, Y. *J. Am. Chem. Soc.* **2003**, *125*, 8694.

(13) Takamatsu, S.; Ishikawa, T.; Koshihara, S. Y.; Ishikawa, N. *Inorg. Chem.* **2007**, *46*, 7250.

(14) Cornia, A.; Mannini, M.; Sainctavit, P.; Sessoli, R. *Chem. Soc. Rev.* **2011**, *40*, 3076.

(15) Domingo, N.; Bellido, E.; Ruiz-Molina, D. *Chem. Soc. Rev.* **2012**, *41*, 258.

(16) Kyatskaya, S.; Mascaros, J. R.; Bogani, L.; Hennrich, F.; Kappes, M.; Wernsdorfer, W.; Ruben, M. *J. Am. Chem. Soc.* **2009**, *131*, 15143.

(17) Mannini, M.; Bertani, F.; Tudisco, C.; Malavolti, L.; Poggini, L.; Misztal, K.; Menozzi, D.; Motta, A.; Otero, E.; Ohresser, P.; Sainctavit, P.; Condorelli, G. G.; Dalcanale, E.; Sessoli, R. *Nat. Commun.* **2014**, *5*, 4582.

(18) Candini, A.; Klyatskaya, S.; Ruben, M.; Wernsdorfer, W.; Affronte, M. *Nano Lett* **2011**, *11*, 2634.

(19) Urdampilleta, M.; Klyatskaya, S.; Cleuziou, J. P.; Ruben, M.; Wernsdorfer, W. *Nat. Mater.* **2011**, *10*, 502.

(20) Gonidec, M.; Biagi, R.; Corradini, V.; Moro, F.; De Renzi, V.; del Pennino, U.; Summa, D.; Muccioli, L.; Zannoni, C.; Amabilino, D. B.; Veciana, J. *J. Am. Chem. Soc.* **2011**, *133*, 6603.

(21) Binnig, G.; Quate, C. F.; Gerber, C. *Phys. Rev. Lett.* **1986**, *56*, 930.

(22) Binnig, G.; Rohrer, H.; Gerber, C.; Weibel, E. *Phys. Rev. Lett.* **1982**, *49*, 57.

(23) Blunt, M. O.; Russell, J. C.; Champness, N. R.; Beton, P. H. *Chem. Commun.* **2010**, *46*,

7157.

(24) Griessl, S. J.; Lackinger, M.; Jamitzky, F.; Markert, T.; Hietschold, M.; Heckl, W. M. *Langmuir* **2004**, *20*, 9403.

(25) Gyarfas, B. J.; Wiggins, B.; Zosel, M.; Hipps, K. W. *Langmuir* **2005**, *21*, 919.

(26) Lackinger, M.; Heckl, W. M. *Langmuir* **2009**, *25*, 11307.

(27) Lei, S.; Tahara, K.; De Schryver, F. C.; Van der Auweraer, M.; Tobe, Y.; De Feyter, S. *Angew. Chem. Int. Ed.* **2008**, *120*, 3006.

(28) Otsuki, J. *Coord. Chem. Rev.* **2010**, *254*, 2311.

(29) Samori, P. *Chem. Soc. Rev.* **2005**, *34*, 551.

(30) Stepanow, S.; Lingenfelder, M.; Dmitriev, A.; Spillmann, H.; Delvigne, E.; Lin, N.; Deng, X.; Cai, C.; Barth, J. V.; Kern, K. *Nat. Mater.* **2004**, *3*, 229.

(31) Katsonis, N.; Lacaze, E.; Feringa, B. L. *J. Mater. Chem.* **2008**, *18*, 2065.

(32) Elemans, J. A. A. W.; De Cat, I.; Xu, H.; De Feyter, S. *Chem. Soc. Rev.* **2009**, *38*, 722.

(33) Elemans, J. A. A. W.; Lei, S. B.; De Feyter, S. *Angew. Chem. Int. Ed.* **2009**, *48*, 7298.

(34) Tahara, K.; Lei, S. B.; Adisoejoso, J.; De Feyter, S.; Tobe, Y. *Chem. Commun.* **2010**, *46*, 8507.

(35) Takami, T.; Ye, T.; Pathem, B. K.; Arnold, D. P.; Sugiura, K.; Bian, Y. Z.; Jiang, J. Z.; Weiss, P. S. *J. Am. Chem. Soc.* **2010**, *132*, 16460.

(36) Tierney, H. L.; Murphy, C. J.; Jewell, A. D.; Baber, A. E.; Iski, E. V.; Khodaverdian, H. Y.; McGuire, A. F.; Klebanov, N.; Sykes, E. C. H. *Nat. Nanotechnol.* **2011**, *6*, 625.

(37) Mali, K. S.; Adisoejoso, J.; Ghijsens, E.; De Cat, I.; De Feyter, S. *Acc. Chem. Res.* **2012**, *45*, 1309.

(38) Miyake, Y.; Nagata, T.; Tanaka, H.; Yamazaki, M.; Ohta, M.; Kokawa, R.; Ogawa, T. *ACS Nano* **2012**, *6*, 3876.

(39) Komeda, T.; Isshiki, H.; Liu, J.; Zhang, Y. F.; Lorente, N.; Katoh, K.; Breedlove, B. K.; Yamashita, M. *Nat. Commun.* **2011**, *2*, 217.

(40) Juan Bartolome, S., Luis, Fernando, Fernández, Julio F. (Eds.) *Molecular Magnets -Physics and Applications*; Springer, 2014.

(41) Ishikawa, N.; Sugita, M.; Wernsdorfer, W. *J. Am. Chem. Soc.* **2005**, *127*, 3650.

(42) Naoto Ishikawa, M. S., Tadahiko Ishikawa, Shin-ya Koshihara, Youkoh Kaizu *J. Phys. Chem. B* **2004**, *108*, 11265.

(43) Ishikawa, N.; Sugita, M.; Okubo, T.; Tanaka, N.; Iino, T.; Kaizu, Y. *Inorg. Chem.* **2003**, *42*, 2440.

(44) Vincent, R.; Klyatskaya, S.; Ruben, M.; Wernsdorfer, W.; Balestro, F. *Nature* **2012**, *488*, 357.

(45) Urdampilleta, M.; Klayatskaya, S.; Ruben, M.; Wernsdorfer, W. *ACS Nano* **2015**, *9*, 4458.

(46) Becker, R. S.; Golovchenko, J. A.; Hamann, D. R.; Swartzentruber, B. S. *Phys. Rev. Lett.* **1985**, *55*, 2032.

(47) Hamers, R. J.; Tromp, R. M.; Demuth, J. E. *Phys. Rev. Lett.* **1986**, *56*, 1972.

(48) Lu, X.; Grobis, M.; Khoo, K. H.; Louie, S. G.; Crommie, M. F. *Phys. Rev. Lett.* **2003**, *90*.

(49) Repp, J.; Meyer, G.; Stojković, S. M.; Gourdon, A.; Joachim, C. *Phys. Rev. Lett.* **2005**, *94*.

(50) Jaklevic, R. C.; Lambe, J. *Phys. Rev. Lett.* **1966**, *17*, 1139.

(51) Lambe, J.; Jaklevic, R. C. *Phys Rev* **1968**, *165*, 821.

(52) Kim, Y.; Komeda, T.; Kawai, M. *Phys. Rev. Lett.* **2002**, *89*.

(53) B. C. Stipe, M. A. R., W. Ho *Science* **1998**, *280*, 1732.

(54) B. C. Stipe, M. A. R., W. Ho *Phys. Rev. Lett.* **1998**, *81*, 1263.

(55) Komeda, T. *Progress in Surface Science* **2005**, *78*, 41.

(56) De Haas, W. J. d. B., J. W.; van den Berg, G. J. *Physica* **1934**, 1115.

(57) Kondo, J. *Prog Theor Phys* **1964**, *32*, 37.

(58) Scott, G. D.; Natelson, D. *ACS Nano* **2010**, *4*, 3560.

(59) Iancu, V.; Deshpande, A.; Hla, S.-W. *Phys. Rev. Lett.* **2006**, *97*.

(60) Iancu, V.; Deshpande, A.; Hla, S. W. *Nano Lett* **2006**, *6*, 820.

(61) Wu, F.; Liu, J.; Mishra, P.; Komeda, T.; Mack, J.; Chang, Y.; Kobayashi, N.; Shen, Z. *Nat. Commun.* **2015**, *6*, 7547.

(62) Aidi Zhao, Q. L., Lan Chen, Hongjun Xiang, Weihua Wang, Shuan Pan, Bing Wang, Xudong Xiao, Jinlong Yang, J. G. Hou, Qingshi Zhu *Science* **2005**, *309*, 1542.

Chapter II Switching of Single-Molecule Magnetic Properties

Tanaka, D.; Inose, T.; Tanaka, H.; Lee, S.; Ishikawa, N.; Ogawa, T. *Chem. Commun.* **2012**, *48*, 7796.

2-1 Introduction

Single-molecule magnets (SMMs) have attracted wide scientific attention owing to their unique energy barrier to magnetic relaxation and their application to molecular spintronics.[1,2] In the last two decades, polymetallic transitionmetal complexes with strong intramolecular exchange coupling have been the typical research target because their high-spin ground state and large anisotropy may give rise to a higher energy barrier than single metal ion complexes.[2-4] Since one of the authors reported single lanthanide ion based SMMs in 2003, many mono nuclear complexes showing slow magnetic relaxation have been reported.[5-13] In particular, the family of phthalocyanine (Pc) based TbIII double-decker compounds displays a higher blocking temperature, below which the magnetic relaxation becomes slow.[9] Moreover, the magnetic relaxation behavior of the double-decker complexes is sensitive to their coordination mode, which can be tuned easily due to their flexible structures. This variation in their coordination modes makes it possible to control their magnetic properties by some external stimulus such as with a redox reaction or pulse current from a STM chip, resulting in unique switching properties.[14,15]

One of the origins of the coordination variety is the stability of various valence states. It is known that some tetrapyrrole (mainly, Pc or porphyrin) based M^{III} double-decker complexes are stable with an unpaired electron in their ligand π-orbital. Because the complexes are composed of one M^{III} ion and two dianions of tetrapyrrole rings (total net charge -1), one electron oxidation of the ligand is required for neutralization, providing the redox active property. On the other hand, since protonation also makes anionic M^{III} double-decker complexes neutral, protonation and deprotonation can alter the properties of a double-decker complex as well.[16] Theoretical research and NMR study have suggested that the proton would exist on the nitrogen of a pyrrole ring and the coordination mode would be changed by protonation and deprotonation.[17-19] However, the position of the proton has not yet been determined by crystal

structure analysis and the effect of a proton on a double-decker complex is still unclear. Herein, we synthesized a tetraphenylporphyrin (TPP) based Tb^{III} double-decker complex and the crystal structures of both the protonated form {[$Tb^{III}H(TPP)_2$], (**1**)} and the anionic form ({[$Tb^{III}(TPP)_2$](H-DBU)}, DBU = 1,8-diazabicyclo[5.4.0] undec-7-ene, (**2**)) were determined by single crystal structure analysis. The crystal structure analysis revealed that the proton in **1** is located on the nitrogen atom of the TPP pyrrole ring, leading to a hepta-coordinated Tb^{III}. In contrast, the anionic complex **2** has a symmetric squareantiprism octa-coordination. The alternating current (ac) magnetic susceptibilities on **1** and **2** demonstrated that **2** showed a slow magnetization relaxation, whereas **1** did not. To the best of our knowledge, this is the first report on double-decker type complexes whose magnetic relaxation behavior is changed by a single proton.

2-2 Experiments

Synthesis of [$Tb^{III}H(TPP)_2$] (1)

Tetraphenylporphyrin (H_2TPP) was prepared according to literature procedures.[1] The powder crystalline sample of **1** was prepared by treating $Tb^{III}(acac)_3 \cdot xH_2O$ (0.276 g), H2TPP (0.124 g) in 1,8-diazabicyclo[5.4.0]undec-7-ene (DBU, 500 μL) at 350 ˚C for 1.5 h. The obtained residue was purified by passing it through an alumina column (CH_2Cl_2) to give a dark purple solid (0.174 g, 62.1%). The powder sample for magnetic measurements was obtained by the same procedure. Crystals suitable for single-crystal X-ray crystallography were obtained by recrystallization from $CHCl_3$/MeOH. MALDI-TOF MS (m/z): M^+ calcd for $C_{88}H_{57}N_8Tb$, 1384.4960; found 1385.7; Anal. Calcd for [$Tb^{III}H(TPP)_2(CH_2Cl_2)_2$]: C, 69.50; H, 3.95; Cl, 9.12; N, 7.20; Tb, 10.22. Found C, 69.09; H, 4.02; N, 7.08.

Synthesis of {[Tb^{III} $(TPP)_2$](H-DBU)} (2)

DBU (60 μL, $4x10^{-4}$ mol) was added to a solution of **1** (9.5 mg, $6.9x10^{-6}$ mol) in $CHCl_3$ (10 mL). Then, methanol was slowly added to the solution resulting in crystalline powder **2**. Crystals suitable for single-crystal X-ray crystallography and the powder sample for magnetic measurements were obtained by the same procedure. MALDI-TOF MS (m/z): M^+ $C_{88}H_{56}N_8Tb$,

1383.39; found 1385.3; Anal. Calcd for {[$Tb^{III}(TPP)_2$](H-DBU)$(CHCl_3)_2$}: C, 66.94; H, 4.26; Cl, 11.97; N, 7.89; Tb, 8.95. Found C, 66.58; H, 4.32; N, 7.83.

Synthesis of {[$Tb^{III}(TPP)_2$]($n$$Bu_4N$)} (3).

A solution of **1** (32.6 mg, 2.4×10^{-5} mol), $n$$Bu_4NBr$ (9.3 mg, 2.4×10^{-5} mol) and triethylamine (1 mL, 7.2×10^{-3} mol) in acetone (10 mL) was evaporated and the dark purple precipitate of **3** was recrystallized in Acetone/Methanol. MALDI-TOF MS (m/z): M^+ $C_{88}H_{56}N_8Tb$, 1383.39; found 1385.3; Anal. Calcd for {[$Tb^{III}(TPP)_2$]($n$$Bu_4N$)($H_2O$)}: C, 75.94; H, 5.76; Cl, 11.97; N, 7.66; Tb, 9.66. Found C, 75.82; H, 5.49; N, 7.79.

Single Crystal X-ray Diffraction.

X-ray structure determination was conducted on a Rigaku VariMax RAPID / FR-E system with $Mo_{K\alpha}$ radiation. In all cases, the structure was solved by direct methods (SHELXS-97)[2] and refined by full-matrix least-squares techniques on F^2 (SHELXL-97).[3]

Crystal data for **1**, C92 H61 Cl12 N8 Tb, M_r = 1862.81, monoclinic, space group $P2_1/c$, (#14), a = 16.0300(5) Å, b = 17.0927(5) Å, c = 30.0170(8) Å, β = 91.7771(8), V = 8220.6(4) $Å^3$, Z = 4, T = 150 K. ρ_{calcd} = 1.505 g/cm^3, $\mu(Mo_{K\alpha})$ = 1.304 cm^{-1}, $2\theta_{max}$ = 50°, λ(MoKα) = 0.71075 Å, 62010 reflections measured, 14442 unique, 9945 > 2σ(I) were used to refine 1010 parameters, 12 restraints, $R(R_w)$ = 0.0800 (0.2367), GOF = 1.034.

Crystal data for **2**, C99 H75 Cl6 N10 Tb, M_r = 1776.31, tetragonal, space group $I4/mmm$, (#139), a = 14.6111(12) Å, c = 19.3957(16) Å, V = 4140.7(6) $Å^3$, Z = 2, T = 150 K. ρ_{calcd} = 1.425 g/cm^3, $\mu(Mo_{K\alpha})$ = 1.104 cm^{-1}, $2\theta_{max}$ = 55°, λ(MoKα) = 0.71075 Å, 20354 reflections measured, 1377 unique, 1376 > 2σ(I) were used to refine 114 parameters, 6 restraints, $R(R_w)$ = 0.0373 (0.1074), GOF = 1.125.

We obtained a non-disordered model of **2** in the space group of $I/422$. However, in the non-disorderd model, inter-molecular distance is too short and unreasonable inter-atom distance was found (H-H distance is 1.42Å). To avoid such unexplainable crowding, we employed the disordered model.

2-3 Results and Discussions

Protonated complex **1** was synthesized by the reaction of H_2TPP, [$Tb^{III}(acac)_3$], and DBU at 350 °C for 1.5 h. The single crystal structure analysis revealed that **1** has a Tb^{III} ion sandwiched between two TPPs as shown in Fig. 1a and b. Seven Tb–N bond distances (Tb–N1, N2, N3, N4, N6, N7, and N8) in **1** varied in the range of 2.430(7)–2.627(7) Å, which are similar to those of reported tetrapyrrole double-decker complexes. However, the distance between Tb and N5 is 2.840(6) Å, which is longer than any other reported distances in tetrapyrrole based double-decker Tb^{III} complexes. Since the distance is even longer than the sum of the ionic radius of Tb^{III} (1.18 Å) and van der Waals radius of N (1.55 Å), no significant interaction between N5 and Tb^{III} exists. The pyrrole ring with N5 is almost parallel to the plane formed from the four *meso*-carbons. The dihedral angle between the pyrrole ring with N5 and the plane from the four meso-carbons (4.1°) is smaller than that of the other pyrrole rings (9.4°–19.0°). Although there are several reports on crystal structures of protonated tetrapyrrole double-decker complexes, the proton is delocalized and no one has yet located the hydrogen atom of the proton

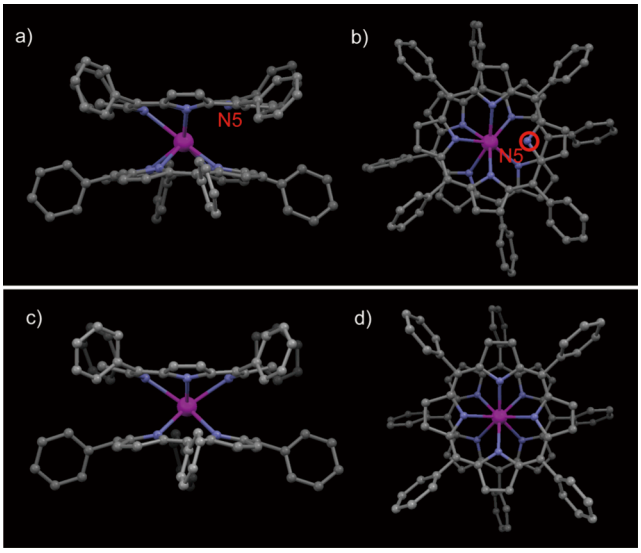

Figure 1. Crystal structures of **1** viewed from the side (a), and from above (b). The proton locates on N5, highlighted with a red circle in (b). Crystal structures of 2 viewed from the side (c), and from above (d). The gray, purple and pink colors represent C, N, and Tb, respectively. Protons are omitted for clarity. Reprinted with permission from ref. 25. Copyright 2012, Royal Society of Chemistry.

by crystal structure analysis.[16,20,21] Because the crystal structure analysis and the elemental analysis of **1** demonstrated that an organic cation, such as protonated DBU (H-DBU), is not included in **1**, we believe that a proton is localized on N5 for charge balance. Moreover, the twisted angle between the two rings was determined to be 35°. Due to the twisted angle and the longer bond distance between Tb^{III} and N5, 1 crystallized in the low symmetry space group, $P2_1/c$.

When the organic proton acceptor, DBU, is added to a solution of **1**, deprotonation occurs to produce the anionic form, **2**. Fig. 2(a) shows the results of the titration of **1** with DBU in CH_2Cl_2. The UV-vis spectra are changed with isosbestic points at 528, 559, 578, 604, and 656 nm, indicating the formation of a deprotonated anionic complex. In addition, the original absorption peak of **1** reappears when acetic acid is added to the anionic complex solution, and thus the protonation/deprotonation process is reversible (Fig. 2(b)). The anionic complex was crystallized with (H-DBU)+ in $CHCl_3$–MeOH solution, and single crystals suitable for X-ray crystal structure analysis were obtained. The crystal structure analysis demonstrated that **2** crystallized in a higher symmetric space group, $I4/mmm$. Although H-DBU is highly disordered

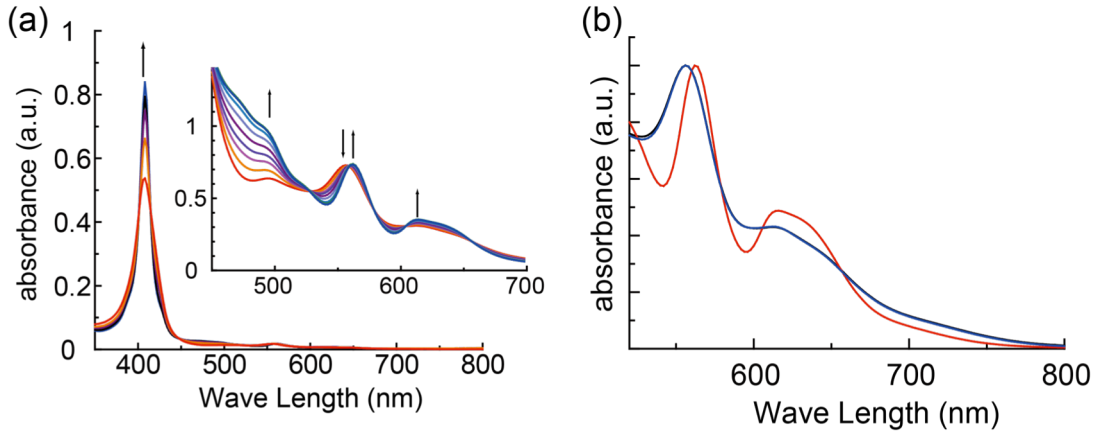

Figure 2. (a) UV-visible spectral changes of **1** during a titration with DBU in CH_2Cl_2. (b) UV-visible spectra of **1** (black), **2** (red) and **2** re-protonated with acetic acid (blue) in CH_2Cl_2. The absorbances are normalized to the maximum peaks. The original absorption peak of **1** reappears upon adding acetic acid to the solution of anion complex, **2**. Reprinted with permission from ref. 25. Copyright 2012, Royal Society of Chemistry.

and the position cannot be determined, the crystal structure of the anionic form of the double-decker complex was determined. The Tb^{III} in the complex exists in a square antiprism coordination environment (Fig. 1c and d). The twisted angle between the two TPP rings is 45°. The eight Tb–N coordination bonds in **2** are crystallographically identical and the bond length is 2.513(4) Å , which is longer than that of a Pc based anionic double-decker complex (2.42–2.45 Å).[22] Considering the low symmetric hepta-coordination mode in **1**, our results showed that a single proton can induce drasticchange in the coordination environment of the TPP based double-decker complex.

Although the crystal structure analysis indicates that the proton in **1** is located on a pyrrole ring, the results of the spectroscopic studies are even more striking. We collected infrared (IR) spectra of **1**, **2**, and an anionic complex with tetrabutylammonium cation (**3**, $\{[Tb^{III}(TPP)_2](n Bu_4N)\}$) prepared by cation exchange. The IR spectra of **1** and **2** in Fig. 3 exhibited strong ν_{N-H} absorptions at 3290 cm^{-1} and 3400 cm^{-1}, respectively. These absorption bands are assigned to the N–H bond of a pyrrole ring of **1** and that of a $(H\text{-}DBU)^+$ cation of **2**, respectively. In contrast, the ν_{N-H} absorption disappeared in **3**, which is consistent with the proton free structure of **3**.

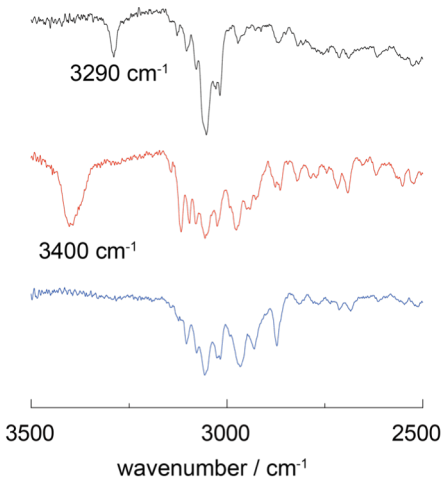

Figure 3. IR spectra of **1** (black), **2** (red), and **3** (blue). The peaks between 2900 and 3150 cm^{-1} are due to C-H stretching of TPP and organic cation. The peaks at 3290 cm^{-1} and 3400 cm^{-1} are from N-H stretching of TPP and $[H\text{-}DBU]^+$, respectively. Reprinted with permission from ref. 25. Copyright 2012, Royal Society of Chemistry.

Cyclic voltammetric (CV) studies of **1**, **2** and **3** in CH_2Cl_2 showed that a multi-step oxidation process occurs for both the protonated and deprotonated complexes (Fig. 4). The detailed analysis demonstrated that six oxidation peaks (E=0.073, 0.42, 0.59, 0.88, 1.29, and 1.62 V *vs*. SCE) appeared in **1** although in the case of anionic complexes **2** and **3**, only four peaks were observed (**2**: E = 0.01, 0.34, 1.21 and 1.58 V *vs.* SCE, **3**: E = 0.16, 0.49, 1.37 and 1.72 V *vs.* SCE). Previous work has indicated that the missing peaks at $E_{1/2}$ = 0.59 and 0.88 V *vs.* SCE can be attributed to the oxidation process of the protonated double-decker complex.[14] This result confirms the presence of the protonated complexes even in solution and the effect of the protonation on the electrochemical properties.

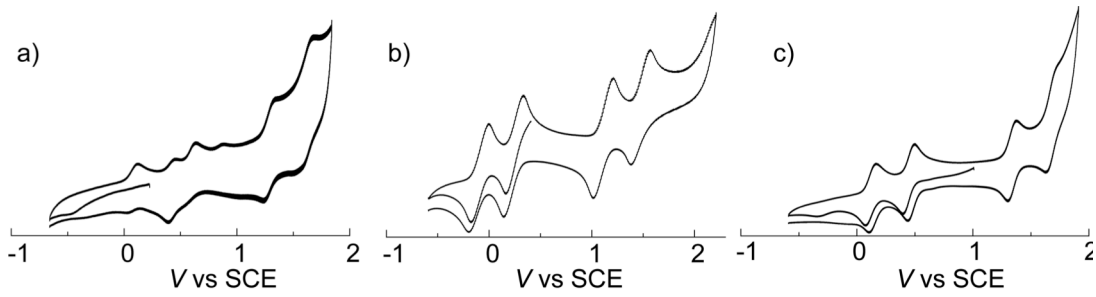

Figure 4. Cyclic voltammograms of (a) **1** in CH_2Cl_2, (b) **2** in CH_2Cl_2, and (c) **3** in CH_2Cl_2 recorded at room temperature (0.10 M n-Bu_4NPF_6, scan rate = 0.10 V/s*)*. Reprinted with permission from ref. 25. Copyright 2012, Royal Society of Chemistry.

To estimate their magnetization relaxation behavior, alternating current (ac) magnetic susceptibility measurements were carried out on a Quantum Design MPMS-XL7AC SQUID magnetometer. Fig. 5a and b show temperature dependences of ac susceptibilities of a polycrystalline powder sample of protonated compound **1**. Frequency dependence on in-phase (χ'_M) and out-of-phase (χ''_M) signals for **1** was not observed at frequencies up to 1000 Hz and temperatures down to 2 K, demonstrating that the protonated complex does not act as an SMM. In contrast, the deprotonated complex **2** exhibited a clear temperature and frequency dependence on ac magnetic susceptibilities as shown in Fig. 5c and d. There was a sharpdrop in χ'_M and χ''_M peaks observed at 18, 21, and 24 K with ac frequencies of 10, 100, and 1000 Hz, respectively, indicating that **2** is an SMM. The χ''_M peak temperature for an ac field of 1000 Hz (24 K) is about the same order of magnitude as that of previously reported Tb^{III} double-decker

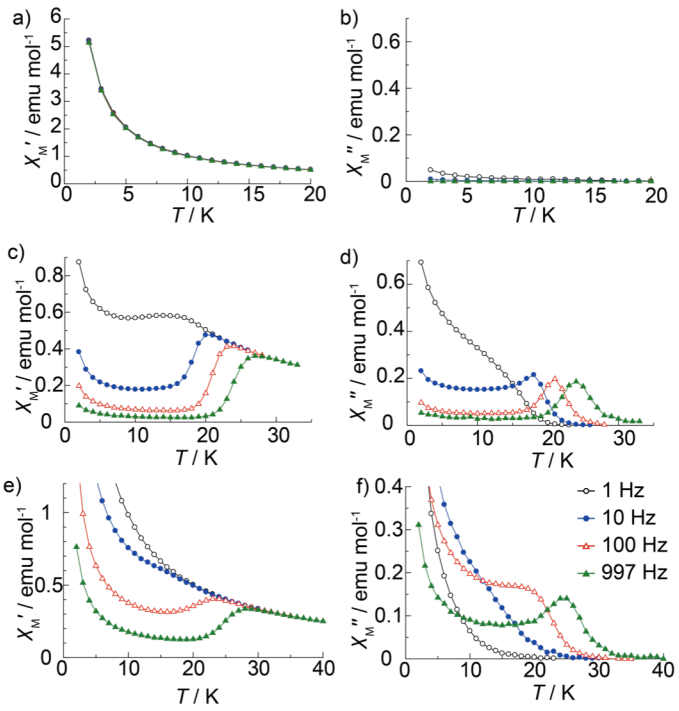

Figure 5. Plots of (a) in-phase (χ'_M) and (b) out-of-phase (χ''_M) signals against temperature T for a powder sample of **1**, and plots of (c) χ'_M and (d) χ''_M against T for a powder sample of **2**, and plots of (e) χ'_M and (f) χ''_M against T for a powder sample of **3.** All are measured in zero dc magnetic field with a 3.9 G ac field oscillating at the indicated frequencies. Reprinted with permission from ref. 25. Copyright 2012, Royal Society of Chemistry.

complexes. The deprotonated complex **3** also showed a clear temperature and frequency dependence although the peaks in the lower temperature region are not clear (Fig. 5e and f). These results have demonstrated that the existence of a proton induces the SMM property switching.

When the dc magnetization of **2** is measured at 1.8 K within ±20 kOe, a butterfly shape is observed (Fig. 6). The butterfly-shaped loop should be attributed to the fast magnetization tunneling process occurring near zero field assisted by nuclear spin $I = 3/2$ of terbium, which was first observed for the structurally analogous $[Tb^{III}(Pc)_2]^-$.[23]

Generally, application of a dc magnetic field can suppress a quantum tunneling relaxation process. The ac magnetic susceptibility measurements of **1** under an applied field of 2000 Oe, however, showed no out-of-phase signal (χ''_M) (Fig. 7). This result indicates that there are other

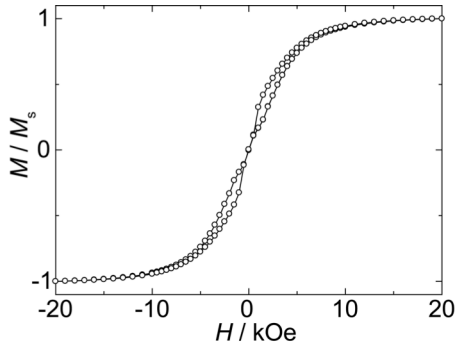

Figure 6. Hysteresis loop for **2** at 1.8 K. Reprinted with permission from ref. 25. Copyright 2012, Royal Society of Chemistry.

factors causing the fast relaxation of 1 than the quantum tunneling process, which dominates the relaxation in the low magnetic field region. In contrast, application of the 2000 Oe dc magnetic field can change the relaxation dynamics of **2**, especially in the measurement with low frequency; the χ''_M signal showed sharper peaks. A similar tendency was observed in the case of **3**. These results suggest that the tunneling process is dominant in the low temperature range at zero dc field. The Argand plot for **2** shows a near-semicircle shape, which is reproduced by the generalized Debye model with a smaller value (Figure 8). This indicates that the magnetic relaxation is dominated by one process. The data for **2** measured under the 2000 Oe dc field were fit to the Arrhenius law to give an effective barrier height for reversal of the magnetic moment of $U_{eff} = 283$ cm^{-1} and a lifetime of $\tau_0 = 6.8 \times 10^{-12}$ s, which is similar to the value estimated from the data under zero dc field with 100 and 997 Hz ($U_{eff} = 269$ cm^{-1} and $\tau_0 = 1.6 \times 10^{-11}$ s, see Fig. 9).

The SMM behavior of Tb^{III} ion in the double-decker complexes is due to the strong Ising-type magnetic anisotropy, which is generated by the axial symmetry of the eight-coordinate environment.[5,6,24] If the local environment of the Tb^{III} ion has an ideal D_{4d} symmetry, the ligand field potential gives no off-diagonal term that would mix the $J_z = +6$ and $J_z = -6$ states.[24] The SMM behavior of **2** is well understood assuming that it has a similar ground multiplet structure as the analogous $[Tb^{III}(Pc)_2]^-$ in which the $J_z = \pm 6$ states are the lowest. In contrast, the protonated complex **1** adopts the heptacoordinated environment with a

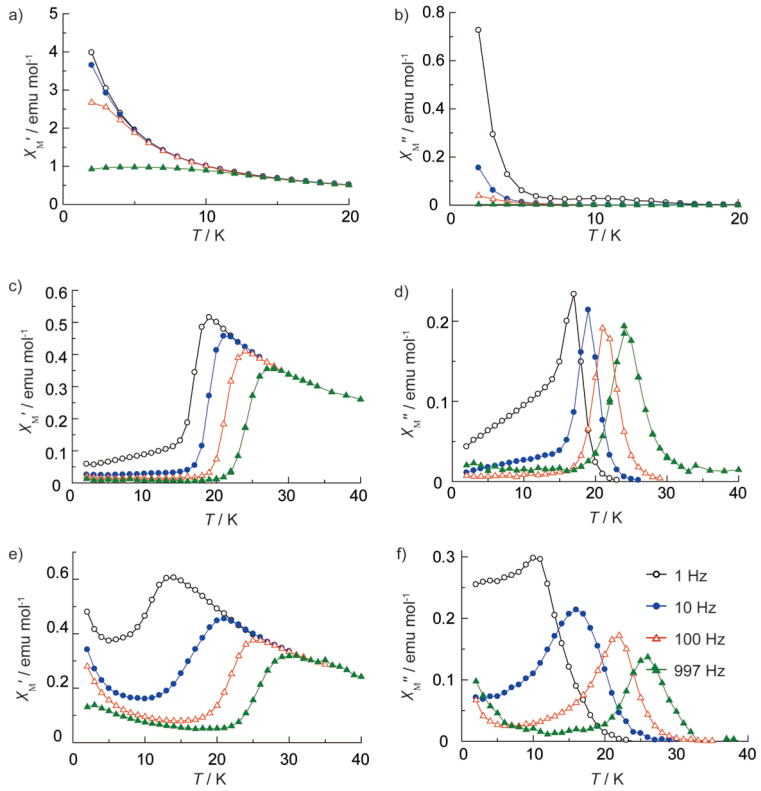

Figure 7. AC susceptibility measured in 2000 Oe dc magnetic field with a 3.9 G ac field oscillating at the indicated frequencies. Plots of (a) in-phase (χ_M') and (b) out-of-phase (χ_M'') against temperature T for a powder sample of **1**, plots of (c) χ_M' and (d) χ_M'' against T for a powder sample of **2**, and plots of (e) χ_M' and (f) χ_M'' against T for a powder sample of **3**. Reprinted with permission from ref. 25. Copyright 2012, Royal Society of Chemistry.

lowered symmetry, which gives substantially large off-diagonal ligand field terms. These terms mix the $J_z = +6$ and $J_z = -6$ states, leading to an acceleration of the magnetic relaxation.[23] Another factor is that the energetic order of the sublevels of the ground multiplet may be significantly different than the eight-coordination environment. The substrates composed of $J_z = \pm 6$ can no longer be the lowest in energy, which should lead to a loss of Ising-type magnetic anisotropy and SMM behavior.

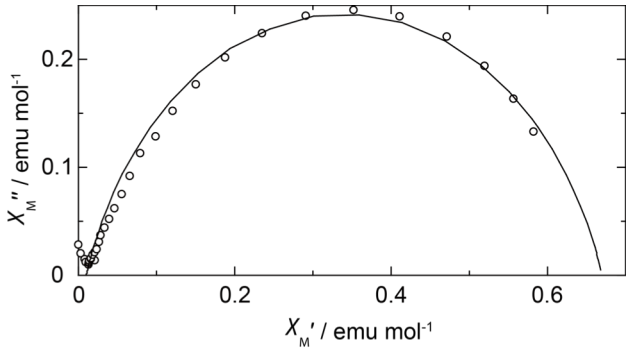

Figure 8. The Argand diagram at 16 K under 2000 Oe for **2**. The solid line represents the least-squares fit obtained with a generalized Debye model with α = 0.19. Reprinted with permission from ref. 25. Copyright 2012, Royal Society of Chemistry.

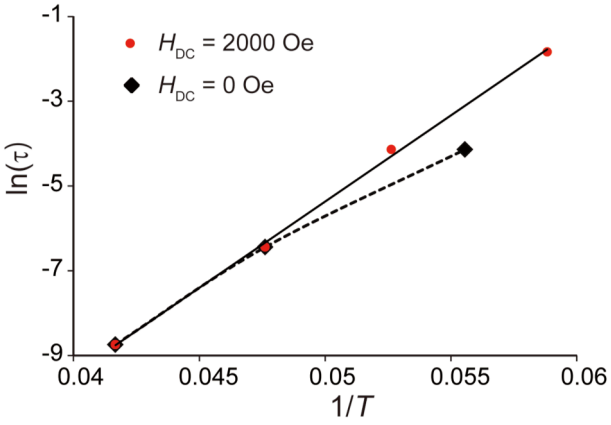

Figure 9. The relaxation time (τ) of **2** under represented dc magnetic field. Black line represents the least-square fit of the data under 2000 Oe dc field to Arrhenius equation. Reprinted with permission from ref. 25. Copyright 2012, Royal Society of Chemistry.

2-4 Conclusions

Our results demonstrate that a single proton is able to delete the stored information on SMM. We expect that our protondriven SMM system will provide us with a new design strategy for SMM based molecular devices.

References

(1) Bogani, L.; Wernsdorfer, W. *Nat Mater* **2008**, *7*, 179.

(2) Brooker, S.; Kitchen, J. A. *Dalton Trans.* **2009**, 7331.

(3) Christou, G.; Gatteschi, D.; Hendrickson, D. N.; Sessoli, R. *MRS Bulletin* **2000**, *25*, 66.

(4) Aromi, G.; Brechin, E. K. *Struct Bond* **2006**, *122*, 1.

(5) Ishikawa, N.; Sugita, M.; Ishikawa, T.; Koshihara, S.-y.; Kaizu, Y. *J. Am. Chem. Soc.* **2003**, *125*, 8694.

(6) Ishikawa, N.; Sugita, M.; Ishikawa, T.; S.Koshihara; Y.Kaizu *J. Phys. Chem. B* **2004**, *108*, 11265.

(7) AlDamen, M. A.; Clemente-Juan, J. M.; Coronado, E.; Marti-Gastaldo, C.; Gaita-Arino, A. *J. Am. Chem. Soc.* **2008**, *130*, 8874.

(8) Rinehart, J. D.; Long, J. R. *J. Am. Chem. Soc.* **2009**, *131*, 12558.

(9) Ishikawa, N. *Struct Bond* **2010**, *135*, 211.

(10) Jiang, S.-D.; Wang, B.-W.; Sun, H.-L.; Wan, Z.-M.; Gao, S. *J. Am. Chem. Soc.* **2011**, *133*, 4730.

(11) Magnani, N.; Apostolidis, C.; Morgenstern, A.; Colineau, E.; Jean-Christophe Griveau; Bolvin, H.; Walter, O.; Caciuffo, R. *Angew. Chem. Int. Ed.* **2011**, *50*, 1696

(12) Weismann, D.; Sun, Y.; Lan, Y. H.; Wolmershauser, G.; Powell, A. K.; Sitzmann, H. *Chem.Eur. J.* **2011**, *17*, 4700.

(13) Yamashita, A.; Watanabe, A.; Akine, S.; Nabeshima, T.; Nakano, M.; Yamamura, T.; Kajiwara, T. *Angew. Chem. Int. Ed* **2011**, *50*, 4016.

(14) Takamatsu, S.; Ishikawa, T.; Koshihara, S.-y.; Ishikawa, N. *Inorg. Chem.* **2007**, *46*, 7250.

(15) Komeda, T.; Isshiki, H.; Liu, J.; Zhang, Y.-F.; Lorente, N.; Katoh, K.; Breedlove, B. K.; Yamashita, M. *Nature Commun.* **2011**, DOI: 10.1038/ncomms1210.

(16) Spyroulia, G. A.; Raptopoulou, C. P.; Montauzon, D. d.; Mari, A.; Poilblanc, R.; Terzis, A.; Coutsolelos, A. G. *Inorg. Chem.* **1999**, *38*, 1683.

(17) Spyroulias, G. A.; Coutsolelos, A. G. *Inorg. Chem.* **1996**, *35*, 1382.

(18) Zhang, Y.; Cai, X.; Yao, P.; Xu, H.; Bian, Y.; Jiang, J. *Chem. Eur. J.* **2007**, *13*, 9503.

(19) Ogi, S.; Ikeda, T.; Wakabayashi, R.; Shinkai, S.; Takeuchi, M. *Chem.Eur. J.* **2010**, *16*, 8285.

(20) Moussavi, M.; Decian, A.; Fischer, J.; Weiss, R. *Inorg. Chem.* **1988**, *27*, 1287.

(21) Spyroulias, G. A.; Coutsolelos, A. G.; Raptopoulou, C. P.; Terzis, A. *Inorg. Chem.* **1995**,

34, 2476.

(22) Loosli, C.; Liu, S. X.; Neels, A.; Labat, G.; Decurtins, S. *Z. Kristallogr. - New Cryst. Struct.* **2006**, *221*, 135.

(23) Ishikawa, N.; Sugita, M.; Wernsdorfer, W. *Angew. Chem. Int. Ed.* **2005**, *44*, 2931.

(24) Ishikawa, N.; Sugita, M.; Okubo, T.; Tanaka, N.; Iino, T.; Kaizu, Y. *Inorg. Chem.* **2003**, *42*, 2440.

(25) Tanaka, D.; Inose, T.; Tanaka, H.; Lee, S.; Ishikawa, N.; Ogawa, T. *Chem. Commun.* **2012**, *48*, 7796.

Chapter III Controlling of Single-Molecule Magnetic Properties by Proton-Coupled Electron Transfer

Inose, T.; Tanaka, D.; Ogawa, T.; *Heterocycles* **2012**, *86*, 1549.

3-1 Introduction

Single-molecule magnets (SMMs) are a unique class of compounds that show superparamagnetic behavior on the single-molecule scale. They have been attracting much attention because of the potential they have for applications such as nanoscale memory devices or quantum computers.[1-5] In particular, a family of phthalocyanine (Pc)-based Tb^{III} double-decker compounds is known to have a high blocking temperature (~50 K) and these compounds are therefore regarded as the most promising set of molecules.[6-13]

We have previously reported the synthesis of protonated and deprotonated (anionic) forms of porphyrin–Tb^{III} double-decker complexes. Their X-ray crystallographic structures were determined for the first time, and their SMM properties were studied.[14] The essential coordination structure of a porphyrin double-decker complex is similar to that of the Pc analog. The most significant finding is that only the deprotonated form of the porphyrin double-decker complex showed single-molecule magnetism (Figure 1). This result indicates that the SMM

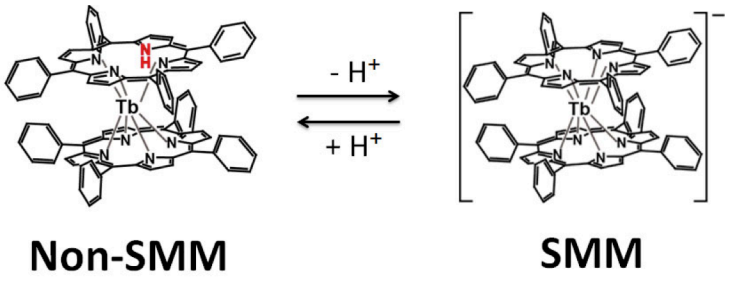

Figure 1. Single-molecule magnetic property switching in porphyrin–Tb double-decker complex. Reprinted with permission from ref. 26. Copyright 2012, The Japan Institute of Heterocyclic Chemistry.

property can be controlled by merely manipulating a single proton.

Here, the porphyrin–quinone dyad shown in Figure 2 is proposed for achieving photo-stimulated SMM switching by forming a double-decker complex with Tb. In this dyad,

the porphyrin is an electron donor and the quinone works as an acceptor, therefore photo-induced electron transfer from the porphyrin to the quinone occurs.[15-17] In addition, there is the possibility that proton-coupled electron transfer (PCET) or excited-state intramolecular proton transfer (ESIPT) can result.[18 19-24] If ESIPT is possible in the porphyrin–quinone dyad, SMM switching in the corresponding Tb double-decker complex can be expected.

3-2 Experiments

In the excited state, CI-Singles (CIS) calculations were performed and their S1 states were revealed. For both in the ground and excited states, time-dependent density functional theory (TDDFT) method was used to calculate vertical excitation energy with the B3LYP parametrization and 6-311G++ basis set. Furthermore the likelihood of ESIPT is discussed based on these results.The DFT calculations were performed using the Gaussian09 software package, and the graphics were generated with the help of the Gauss View software.

3-3 Results and Discussions

For double-decker complex, to have a D_{4d} symmetry for the local environment of the Tb^{III} ion is important to show SMM property so the designed molecule can show SMM property. Although there are several experimental and theoretical papers reporting on ESIPT,[21] its

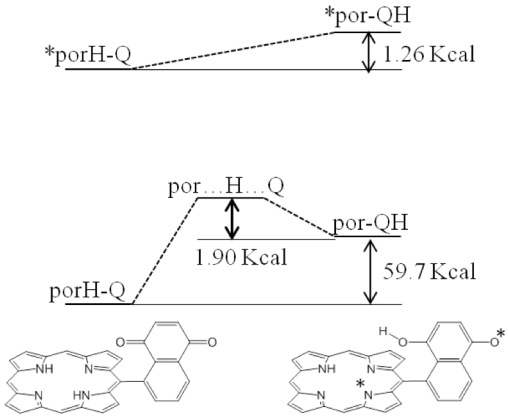

Figure 2. Energy level diagram before (porH-Q) and after (por-QH) ESIPT and the transition state (por···H···Q) of the porphyrin–quinone dyad. Reprinted with permission from ref. 26. Copyright 2012, The Japan Institute of Heterocyclic Chemistry.

occurrence in the molecular system proposed here has so far been unconfirmed.

In this work, density functional theory (DFT)-based calculations were performed relating to the molecular system shown in Figure 2, in the ground state.

Five structures were optimized with (U)B3LYP/6-311G++, and are shown in Figure 2, along with the corresponding energies. PorH-Q and por-QH indicate the ground states before and after ESIPT, respectively, and *porH-Q and *por-QH represent the excited states before and after ESIPT, respectively. Por···H···Q indicates the transition state between porH-Q and por-QH, which was obtained by the QST2 procedure in the Gaussian09[25] program package, and optimized for the transition state. The assignment of the transition structure was confirmed by the presence of one imaginary harmonic frequency in the force calculation.

Figure 3 shows the calculated optimized structure of the transition state. As shown, the N–H distance is 2.20 Å, the O–H distance is 1.01 Å, and the angle formed by N–H–O is 157°.

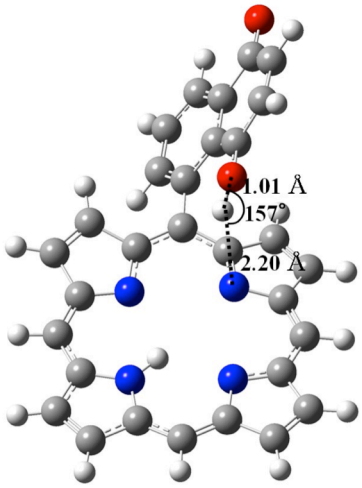

Figure 3. Structure of the optimized transition state in the ground state obtained by UB3LYP/6-311G++. Reprinted with permission from ref. 26. Copyright 2012, The Japan Institute of Heterocyclic Chemistry.

This structure indicates that the transition state is more similar to por-QH than to the starting porH-Q.

Figure 4 illustrates the highest occupied molecular orbitals (HOMOs) and lowest unoccupied molecular orbitals (LUMOs) of the four states of the porphyrin–quinone dyads. Figure 4(a) shows the ground state before ESIPT (porH-Q). The HOMO can be assigned to

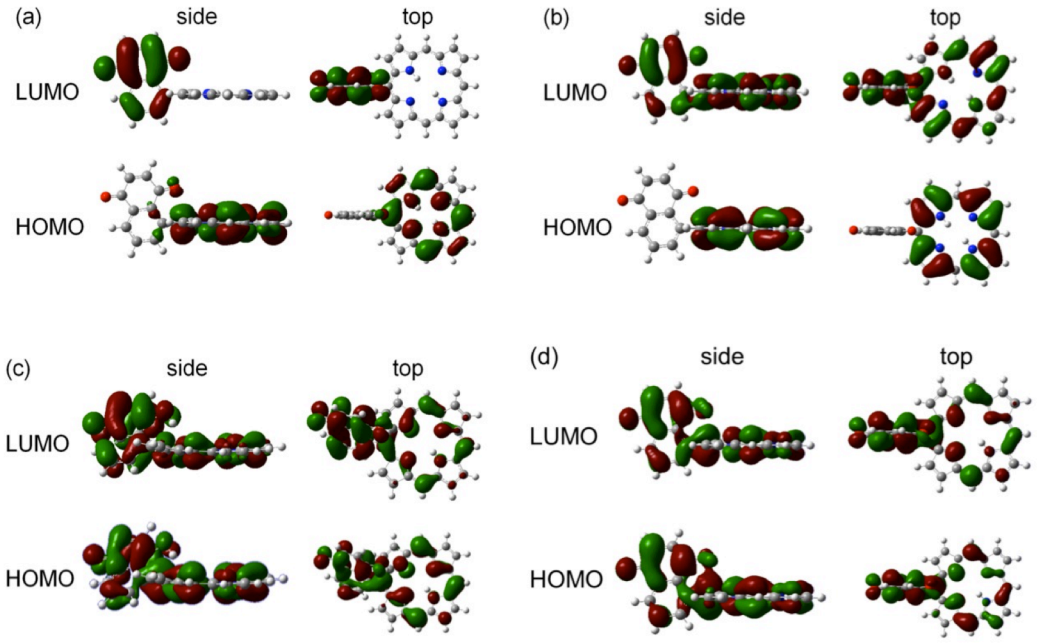

Figure 4. B3LYP/6-311G++ calculated frontier HOMO and LUMO orbitals of (a) ground state of porH-Q, (b) excited state of porH-Q, (c) ground state of por-QH, and (d) excited state of por-QH. Reprinted with permission from ref. 26. Copyright 2012, The Japan Institute of Heterocyclic Chemistry.

the p-orbital located mostly on the porphyrin of the dyad, and the LUMO to the p-orbital located entirely on the quinone of the dyad. Figure 4(b) shows the excited state before ESIPT (*porH-Q). Here, the HOMO p-orbital was located entirely on the porphyrin of the dyad, but the LUMO p-orbital was partially placed on the quinone. Figures 4(c) and (d) show the ground and excited states after ESIPT has occurred (por-QH and *por-QH). The electron was spread over the entire porphyrin–quinone dyad.

In the ground state, the structure after the ESIPT (por-QH) is 59.7 kcal/mol less stable than the starting structure (porH-Q). However, in the excited state, the energy difference decreases to only 1.26 kcal/mol, which can be easily overcome by thermal activation at room temperature. The activation energy for the backward reaction in the ground state was

estimated from the energy of the transition state (por···H···Q) to be 1.90 kcal/mol. From the TDDFT calculations, the excitation energy of porH-Q was 824 nm (34.7 kcal) and por-QH was 1022 nm (28.0 kcal) in the ground state. In the excited state, the energy of *porH-Q was 1390 nm (20.6 kcal) and *por-QH was 2310 nm (12.4 kcal).

The above energy estimations mean that although the por-QH is less stable than the starting porH-Q, the proton transfer reaction can readily proceed as a result of photo-excitation, and the ground state of por-QH has some life-time because of the activation energy of 1.90 kcal/mol. If this activation energy can be increased by molecular design, the por-QH state could have a long enough life-time to be used as an optical memory molecule. In this calculation, we couldn't clear whether only proton transfer occurred or electron transfer also occurred because there were no differences between α spin and β spin. Moreover, in our previous research, using infrared (IR) spectroscopy, it was shown that the strength of the N–H bond of the porphyrin double-decker was weaker than that of a single porphyrin molecule.[14] In combination, these results suggest that SMM switching in the solid state can be expected for this Tb^{III}–porphyrin double-decker complex using a porphyrin–quinone dyad.

3-4 Conclusions

In this study a porphyrin double-decker complex with quinone dyad was designed to achieve the SMM switching in solid state. In this molecule it is expected to occur PCET. To confirm the possibility to occur PCET, energy barrier between the ground state of both before and after PCET and transition state of a porphyrin with quinone dyad was estimated from TD-DFT calculations. From the calculation results, it was suggested the possibility of PCET in this double-decker complex.

References

(1) Seneor, P.; Bernand-Mantel, A.; Petroff, F. *J. Phys.: Condens Matter* **2007**, *19*, 165222.

(2) Stepanenko, D.; Trif, M.; Loss, D. *Inorg. Chim. Acta* **2008**, *361*, 3740.

(3) Katoh, K.; Yoshida, Y.; Yamashita, M.; Miyasaka, H.; Breedlove, B. K.; Kajiwara, T.; Takaishi, S.; Ishikawa, N.; Isshiki, H.; Zhang, Y. F.; Komeda, T.; Yamagishi, M.; Takeya, J. *J. Am. Chem. Soc.* **2009**, *131*, 9967.

(4) Friedman, J. R.; Sarachik, M. P. In *Annual Review of Condensed Matter Physics, Vol 1*; Langer, J. S., Ed. 2010; Vol. 1, p 109.

(5) Katoh, K.; Isshiki, H.; Komeda, T.; Yamashita, M. *Chem. Asian J.* **2012**, *7*, 1154.

(6) Ishikawa, N.; Sugita, M.; Ishikawa, T.; Koshihara, S.; Kaizu, Y. *J. Am. Chem. Soc.* **2003**, *125*, 8694.

(7) Ishikawa, N.; Mizuno, Y.; Takamatsu, S.; Ishikawa, T.; Koshihara, S. Y. *Inorg. Chem.* **2008**, *47*, 10217.

(8) Sessoli, R.; Powell, A. K. *Coord. Chem. Rev.* **2009**, *253*, 2328.

(9) Ishikawa, N. In *Functional Phthalocyanine Molecular Materials*; Jiang, J., Ed. 2010; Vol. 135, p 211.

(10) Fukuda, T.; Kuroda, W.; Ishikawa, N. *Chem. Commun.* **2011**, *47*, 11686.

(11) Katoh, K.; Isshiki, H.; Komeda, T.; Yamashita, M. *Coord. Chem. Rev.* **2011**, *255*, 2124.

(12) Katoh, K.; Kajiwara, T.; Nakano, M.; Nakazawa, Y.; Wernsdorfer, W.; Ishikawa, N.; Breedlove, B. K.; Yamashita, M. *Chem. Eur. J.* **2011**, *17*, 117.

(13) Sakaue, S.; Fuyuhiro, A.; Fukuda, T.; Ishikawa, N. *Chem. Commun.* **2012**, *48*, 5337.

(14) Tanaka, D.; Inose, T.; Tanaka, H.; Lee, S.; Ishikawa, N.; Ogawa, T. *Chem. Commun.* **2012**, *48*, 7796.

(15) Tabushi, I.; Koga, N.; Yanagita, M. *Tetrahedron Lett.* **1979**, 257.

(16) Joran, A. D.; Leland, B. A.; Felker, P. M.; Zewail, A. H.; Hopfield, J. J.; Dervan, P. B. *Nature* **1987**, *327*, 508.

(17) Osuka, A.; Maruyama, K.; Hirayama, S. *Tetrahedron* **1989**, *45*, 4815.

(18) Paul, B. K.; Guchhait, N. *Comput. Theor. Chem.* **2011**, *972*, 1.

(19) Okamura, M. Y.; Paddock, M. L.; Graige, M. S.; Feher, G. *Biochim. Biophys. Acta* **2000**, *1458*, 148.

(20) Stubbe, J.; Nocera, D. G.; Yee, C. S.; Chang, M. C. Y. *Chem. Rev.* **2003**, *103*, 2167.

(21) Karr, P. A.; Zandler, M. E.; Beck, M.; Jaeger, J. D.; McCarty, A. L.; Smith, P. M.; D'Souza,

F. *Theochem-J. Mol. Struct.* **2006**, *765*, 91.

(22) Huynh, M. H. V.; Meyer, T. J. *Chem. Rev.* **2007**, *107*, 5004.

(23) Hammes-Schiffer, S. *J. Phys. Chem. Lett.* **2011**, *2*, 1410.

(24) Warren, J. J.; Mayer, J. M. *J. Am. Chem. Soc.* **2011**, *133*, 8544.

(25) Frisch, M. J.; Trucks, G. W.; Schlegel, H. B.; Scuseria, G. E.; Robb, M. A.; Cheeseman, J. R.; Scalmani, G.; Barone, V.; Mennucci, B.; Petersson, G. A.; Nakatsuji, H.; Caricato, M.; Li, X.; Hratchian, H. P.; Izmaylov, A. F.; Bloino, J.; Zheng, G.; Sonnenberg, J. L.; Hada, M.; Ehara, M.; Toyota, K.; Fukuda, R.; Hasegawa, J.; Ishida, M.; Nakajima, T.; Honda, Y.; Kitao, O.; Nakai, H.; Vreven, T.; Montgomery, J. A.; Jr.; Peralta, J. E.; Ogliaro, F.; Bearpark, M.; Heyd, J. J.; Brothers, E.; Kudin, K. N.; Staroverov, V. N.; Kobayashi, R.; Normand, J.; Raghavachari, K.; Rendell, A.; Burant, J. C.; Iyengar, S. S.; Tomasi, J.; Cossi, M.; Rega, N.; Millam, J. M.; Klene, M.; Knox, J. E.; Cross, J. B.; Bakken, V.; Adamo, C.; Jaramillo, J.; Gomperts, R.; Stratmann, R. E.; Yazyev, O.; Austin, A. J.; Cammi, R.; Pomelli, C.; Ochterski, J. W.; Martin, R. L.; Morokuma, K.; Zakrzewski, V. G.; Voth, G. A.; Salvador, P.; Dannenberg, J. J.; Dapprich, S.; Daniels, A. D.; Farkas, Ö.; Foresman, J. B.; Ortiz, J. V.; Cioslowski, J.; Fox, D. J.; Gaussian 09, Revision C.1 ed.; Gaussian, Inc.: Wallingford, CT, 2009.

(26) Inose, T.; Tanaka, D.; Ogawa, T.; *Heterocycles* **2012**, *86*, 1549.

Chapter IV Observation of the Supramolecular Structure of Tb^{III}-octaethylporphyrin Double-Decker Complexes with Three Different Electronic Structures

Inose, T.; Tanaka, D.; Tanaka, H.; Ivasenko, O.; Nagata, T.; Ohta, Y.; De Feyter, S.; Ishikawa, N.; Ogawa, T.; *Chem. Eur. J.* **2014**, *20*, 11362.

4-1 Introduction

Molecular spintronics, a technology exploiting both charge and spin degrees of freedom at the single-molecule scale, has emerged as a promising topic toward single-molecule magnets at both the fundamental and applied levels of study.[1] Some of the more promising materials in the field of molecular spintronics are single-molecule magnets (SMMs).[2-11] SMMs behave like nanoscale magnetic molecules because of the slow relaxation of magnetization under blocking temperature. Since 2003 it has been expected that lanthanide-based SMMs are one of the most attractive materials due to the intensely large magnetic anisotropy of lanthanide ions although many transition metal SMMs have been reported.[12] One of the most famous and attractive SMMs is the family of phthalocyanine (Pc)-based Tb(III) double-decker compounds ($TbPc_2$) because this compounds show higher blocking temperatures, among many mono- or multinuclear lanthanide SMMs, and many studies of $TbPc_2$ SMMs have been reported.[13-18]

Designing of SMMs as active units is one of the interesting themes for spintronic devices recently. Scanning tunneling spectroscopy (STS) techniques and nanogap electrodes has high potential to reveal the electric property of molecules at the single-molecule level and used to detect electrical conductance of $TbPc_2$ derivatives recently.[19-23] Further, another interesting research to detect the magnetic state of SMMs is using $TbPc_2$ derivatives on nanocarbon materials and the magnetic state is detected by electrical signals.[24,25] Spin-valve effects is an essential tool on magnetization in nanocarbon/SMM composite materials, and the electrical detection of the magnetization reversal of $TbPc_2$ has been demonstrated. Nanocarbon/SMM composites contain at least two SMM centers on the graphene sheet or carbon nanotube; the relative direction of the SMM magnetic moments strongly affect the conductance of the electrons passing through the nanocarbon material. This composite spin-valve system is very

attractive for future spintronics devices; however, the relationship between the supramolecular structure of SMMs on carbon materials and the resultant magnetoresistance remains unknown. Moreover, although previous reports strongly suggest that an organic π radical on phthalocyanine plays a crucial role in charge–spin coupling, double-decker complexes without π radicals such as reduced anionic forms have not been studiedin such composite systems, and thus the effect of the π radical on the charge–spin coupling remains unclear. We reason that the control of these two parameters – namely the 2D supramolecular structure and the oxidative state of the ligand – is critically important for fabrication of nanocarbon/SMM composites.

Suitable design strategies for 2D supramolecular structure of SMMs on carbon materials have not been proposed, on the other hand the attention is currently focused on the SMM properties on surfaces.[3,9,26-30] We thought studying about the 2D supramolecular structures of SMMs on carbon materials is important to establish SMMs as reliable spin-valve devices. Generally, it regarded fabrication of a 2D structure on solid surfaces based on self-assembly is a very interesting subject owing to the perspective of many applications in the field of nanoscience and nanotechnology.[31-35] Scanning tunneling microscopy (STM) has high potential to observe controlled 2D supramolecular structure on a surface at single-molecule level.[36-46] Many STM studies used HOPG as a substrate have been reported because it is known that alkyl chain can interact with carbon materials strongly. So it is expected that introducing many alkyl groups can fabricate well-ordered 2D supramolecular structures on HOPG. Desired 2D surface structures of SMMs on carbon materials will be achieved by designing SMMs with alkyl groups.

Another important factor to design active units for molecular spin-valve system is the difference of the electronic structures of Tb^{III} double-decker complexes. Radical form phthalocyanineato or porphyrinato M^{III} based double-decker complexes has a spin of a π radical and these molecules exist in stable state. Neutral complexes can be obtained by one-electron oxidation of the ligand. The double-decker complexes show redox-active properties because total net charge of the summing of one M^{III} ion and two tetrapyrrole rings as dianions is -1. Additionally, the electronic structures of double-decker complexes can be changed by

protonation and deprotonation, because protonation of the anionic form double-decker complexes also can occur neutralization of the double-decker complexes. Moreover their magnetic relaxation behaviors can be affected by the electronic states of double-decker complexes. In our past study it was revealed that isolating both protonated and anionic form tetraphenylporphyrin (TPP)-Tb^{III} double-decker complexes induced drastic switching of the SMM property.[47] Moreover, it is suggested suggested that the Tb^{III} magnetic moment and the organic π radical is coupled weakly, and the conductive electron through coupling can be affected by the magnetic information on the Tb^{III} ion. Although there are a few reports about 2D supramolecular structures of radical form double-decker complexes, it is strongly expected to achieve controlling of electrical structures of double-decker complexes in 2D supramolecular structures for well-designed systems of molecular spin-valve.

Previously, we have paid attention on porphyrin–Tb^{III} double-decker SMMs due to their high designability and unique properties of their proton-induced magnetic switching.[47,48] Here, we show the synthesis of a 2,3,7,8,12,13,17,18-octaethylporphyrin (OEP)-Tb^{III} double-decker complex ($Tb(oep)_2$) because it is expected that ethyl groups of this molecule can enhance the interaction between a carbon surface and the molecule. We chose HOPG as a substrate and revealed the 2D surface structures of each molecule on HOPG by STM. HOPG is an ideal substrate for use in STM measurements because the surface structure is identical with that of graphene. $Tb(oep)_2$ of protonated (**1**), anionic (**2**), and radical (**3**) forms were prepared (Scheme 1).[48]

We measured the magnetic properties of all $Tb(oep)_2$ and revealed drastic magnetic

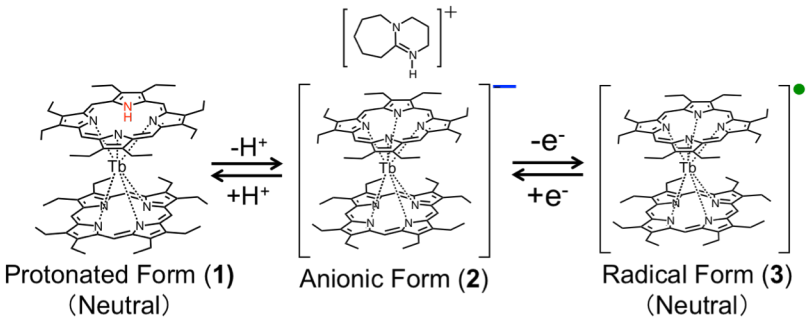

Scheme 1. Molecular structures of $Tb(oep)_2$ double-decker complexes with three different electronic states. Copyright 2014, Wiley.

switching was possible by changing the electronics structures. Moreover we have successfully observed the 2D surface structures of $Tb(oep)_2$ with different electronic structures.

4-2 Results and Discussions

Synthesis.

First we got a protonated complex **1** in yield 37.4 % by mixing H_2OEP, $[Tb^{III}(acac)_3]$ (acac = acetylacetonate), and DBU and heating at 330 ºC for 1.5 h. To get an anionic form double-decker complex **2**, DBU was added as a base to a solution of **1** in chloroform. The objective was obtained in yield 86.9 %. Moreover radical form double-decker complex **3** was synthesized by adding $NOBF_4$ as an oxidation agent to a solution of **2** in distilled dichloromethane under nitrogen, in yield 55.2 %. The colors of all powder samples were dark red-purple and it is stable under ambient conditions.

We could also get a protonated complex **4** by mixing H_2BDP, $[Tb^{III}(acac)_3]$ and DBU, and heating at 300 ºC for 1.5 h, it is almost the same reaction condition compared to protonated form complex **1**. The pure powder sample of **4** with red-brown color was gotten in yield of 50 %.

UV-Visible Spectroscopy.

Figure 1 shows the UV-vis spectra of each double-decker complex. The Soret bands of three double-decker complexes were compared. Radical complex **3** (374.0 nm) was blue shifted compared to that of a protonated complex **1** (386.0 nm) and an anionic complex **2** (387.0 nm). Additionally complex **3** also showed near-infrared absorption band (1190 nm). The blue shifts of the Soret band are discussed in terms of "excitonic interactions". Because an electron of radical complex **3** was removed from an antibonding orbital of the highest occupied molecular orbitals (HOMO), it is expected that this leads to an enhancement in the electronic ground state π–π interaction of the sandwich complexes, to diminish the cofacial distance between two π electronic systems.[49-53] Consequently, the increasing of excitonic interaction causes the observed blue shifts of the Soret band.

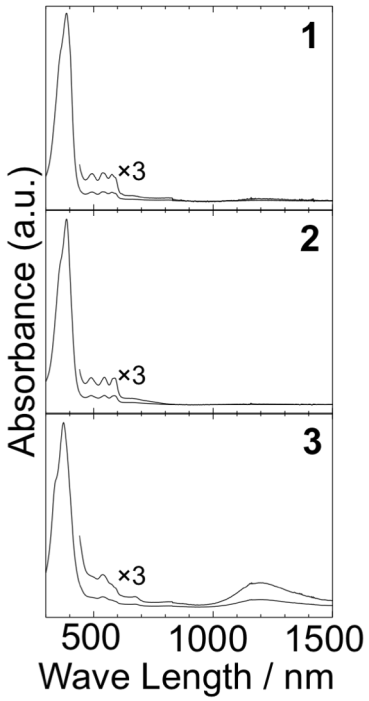

Figure 1. UV-vis spectra of a protonated form **1**, an anionic form **2**, and radical form **3** in dichloromethane. Reprinted with permission from ref. 60. Copyright 2014, Wiley.

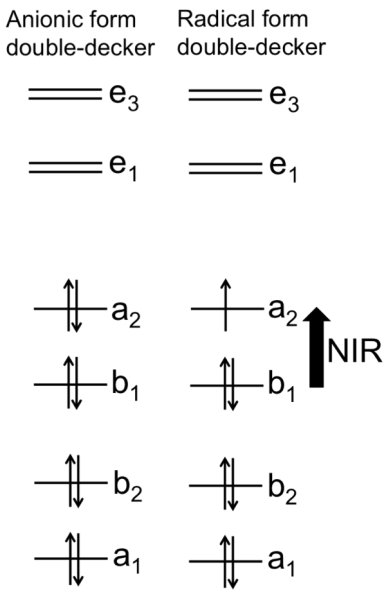

Figure 2. A partial energy diagram for anionic form **2** and radical form **3** double-decker complexes. Reprinted with permission from ref. 60. Copyright 2014, Wiley.

Figure 2 shows a part of molecular orbital diagrams to explain the NIR absorption feature of **3**. In this figure, transition of an electron from the filled bonding orbital of b_1 to the half-filled antibonding orbital of a_2 occurs and it leads the NIR absorption.

Electrochemistry.

Cyclic Voltammetric (CV) measurements of a protonated form **1** and an anionic form **2** in CH_2Cl_2 was shown in Figure 3. A number of steps of oxidation process which occured for both the protonated form and anionic form complexes were observed. The detailed analysis showed that a protonated complex **1** showed six oxidation peaks (E = -0.49, -0.11, 0.058, 0.63, 1.04 and 1.40 V vs. ferrocene/ferrocenium (Fc/Fc^+)). On the other hand, an anionic complex **2** showed only four peaks (E = -0.44, -0.10, 1.03, 1.40 V vs. Fc/Fc^+). From the past study, redox status of the protonated form double-decker complex shows two specific oxidation peak and it corresponds to peaks of E = 0.058 V, 0.63 V in a protonated complex **1**. This result can be one proof that the protonated complexes can exist stable even in solution state and the protonation affects the electrochemical properties.

In the past study, the CV data display freebase octaethylporphyrin (OEP) is oxidized easier than that of freebase tetraphenylporphyrin (TPP).[54,55] The first oxidation potential of a

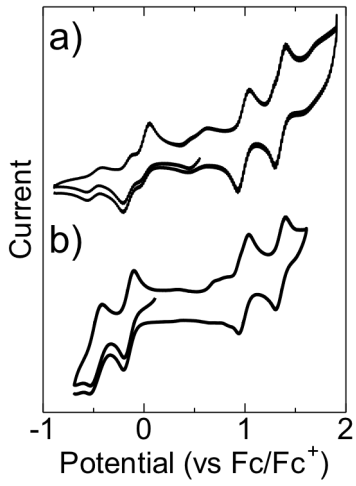

Figure 3. Cyclic voltammograms of (a) protonated form **1**, and (b) anionic form **2** in CH_2Cl_2, measured at room temperature (0.10 M n-Bu_4NPF_6, scan rate = 0.10 V/s). Reprinted with permission from ref. 60. Copyright 2014, Wiley.

freebase OEP is 0.29 V (vs. Fc/Fc^+). On the other hand, the first oxidation potential of TPP is 0.49 V (vs. Fc/Fc^+) and the value is 0.20 V higher than that of freebase OEP. In double-decker complex, it can say the same thing for an anionic form double-decker complex, that is, -0.44 V (vs. Fc/Fc^+) of the first oxidation potential is also more susceptible to that of -0.37 V (vs. Fc/Fc^+) of oxidation than an anionic form TPP double-decker complex.[47]

Magnetic measurement.

Alternating current (ac) magnetic susceptibility measurements of three kinds of complexes revealed their magnetization relaxation behavior (Figure 4 and Figure 5). Figure 4(a) and (b) shows temperature dependence of ac susceptibility of a protonated complex **1** in powder sample under zero dc field and frequency dependence of in-phase (χ_M') and out-of-phase (χ_M") for **1** were not observed at frequencies up to 1000 Hz and temperatures down to 2 K. From this result it was revealed that a protonated complex **1** was non-SMM. Even magnetic field of 2000 Oe was applied in the measurement of ac magnetic susceptibility of **1**, out-of phase signal (χ_M") was not observed as shown in Figure 5 (a), (b). These results indicate that there are another factors which cause the fast relaxation process of a protonated form double-decker complex

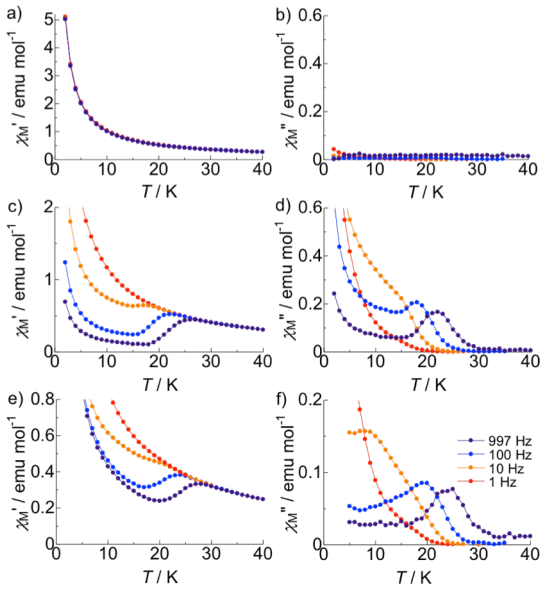

Figure 4. Temperature dependence of the in-phase (χ_M') and out-of-phase (χ_M") ac susceptibility of (a, b) protonated form **1**, (c, d) anionic form **2**, and (e, f) radical form **3** under zero dc magnetic field. Reprinted with permission from ref. 60. Copyright 2014,

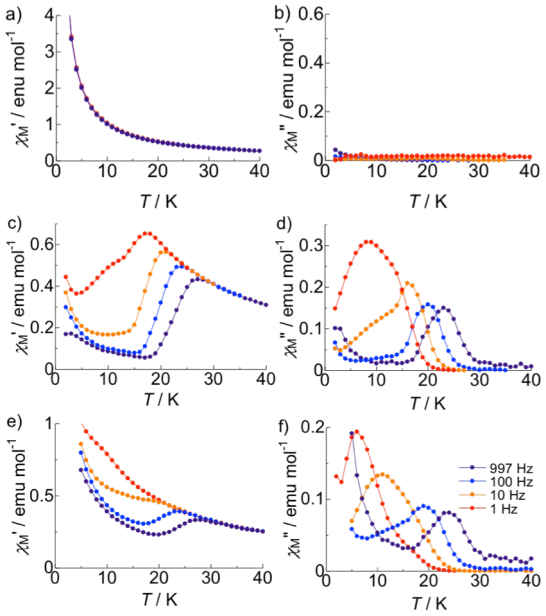

Figure 5. Temperature dependence of the in-phase (χ_M') and out-of-phase (χ_M") ac susceptibility of (a, b) protonated form **1**, (c, d) anionic form **2**, and (e, f) radical form **3** under 2000 Oe magnetic field. Reprinted with permission from ref. 60. Copyright 2014, Wiley.

except for the quantum tunneling process.

Previously, we showed the non-SMM property of the protonated form tetraphenylporphyrin-Tb^{III} double-decker complex because its symmetric coordination environment was low.[47] It is expected that the distortion of **1** shows almost same as that of tetraphenylporphyrin-Tb^{III} double-decker complex although to determine the molecular structure of **1** from the X-ray single crystal analysis was difficult. And it seems the same reason of the case of a tetraphenylporphyrin-Tb^{III} double-decker complex that non-SMM property of protonated complex **1**. In contrast, Figure 4 (c) ~ (f) showed a clear frequency dependence of an anionic form **2** and a radical form **3** by the measurement of ac magnetic susceptibility. A sharp drop in the in-phase (χ_M') and out-of-phase (χ_M") peaks in different temperature ranges dependent on the frequency was observed, and it indicates that these two complexes **2, 3** act as an SMM. The χ_M" peak was observed for an field of 1000 Hz at 23 K in an anionic complex **2** and at 24 K in a radical complex **3**, respectively. These values seem almost same value of the magnitude of an anionic tetraphenylporphyrin-Tb^{III} double-decker complex whose χ_M" peak was observed at 24 K. In the past study it was reported that the strength of the ligand field (LF)

effected the blocking temperature.[14] As mentioned previously in section of UV-vis spectra, removal of an electron of a radical form **3** from an antibonding orbital of HOMO occurs diminishing the cofacial distance between two π electric systems, and it results in LF potential of **3**. The higher blocking temperature compared to anionic form is attributed to this stronger LF potential of radical form **3**. Figures 5 (c) ~ (f) show results of the measurements of ac magnetic susceptibility of an anionic form complex **2** and a radical form complex **3**. 2000 Oe magnetic field was applied in the measurement and this magnitude of the magnetic field can change the relaxation dynamics of the sample. These results suggest that the dominant relaxation process of **2** and **3** at low temperature under zero dc magnetic field is the tunneling process.

Variable-frequency ac magnetic susceptibility can reveal the detail of the SMM properties and Figure 6 shows the results of both **2** and **3** under zero dc magnetic field and 2000 Oe dc magnetic field. In the temperature range of this measurement, both complex **2** and **3** showed the decreasing of the in-phase (χ_M') element of the ac susceptibility, and peaks in the out-of-phase (χ_M") element appeared at the same time, which mean clear slow magnetic relaxation. Figure 7 shows Argand plots of anionic complex **2** and radical complex **3**, and the generalized Debye mode was used for their fitting. Figure 7 (a) and (b) show semicircular plots for complex **2** which were gotten below 24 K and (a) is the result under zero dc magnetic field and (b) is under 2000 Oe dc magnetic field. The α parameter of **2**, which was obtained in the fitting of extended Debye model and quantifies the width of the relaxation time (τ) distribution, was in the range of 0.16 – 0.29 at zero dc field (from 10 K to 24 K) and 2000 Oe dc field (from 14 K to 24 K). Figure 7 (c) shows semicircular plots of complex **3** which are gotten below 24 K (Figure 7 (c)) with the α parameter in the range of 0.22 – 0.29 under zero dc field (from 6 K to 24 K) and 2000 Oe dc field (from 12 K to 24 K). Here, extended Debye model is written by following equations.

$$\chi(\omega) = \chi_s + \frac{\chi_t - \chi_s}{1+(\iota\omega\tau)^{1-\alpha}}$$

$$\chi'(\omega) = \chi_s + (\chi_t - \chi_s)\frac{1+(\omega\tau)^{1-\alpha}\sin(\pi\alpha/2)}{1+2(\omega\tau)^{1-\alpha}\sin(\pi\alpha/2)+(\omega\tau)^{2-2\alpha}}$$

$$\chi''(\omega) = (\chi_t - \chi_s)\frac{(\omega\tau)^{1-\alpha}\cos(\pi\alpha/2)}{1+2(\omega\tau)^{1-\alpha}\sin(\pi\alpha/2)+(\omega\tau)^{2-2\alpha}}$$

Here χ_s is the value of the left edge of the semicircular (frequency $\omega \to \infty$) and χ_t is the value of the right edge of the semicircular (frequency $\omega \to 0$),[56] α the relaxation time distribution factor, and τ the relaxation time. In Figure 7 (c), both the values of χ_s and χ_t for complex **3** is gradually

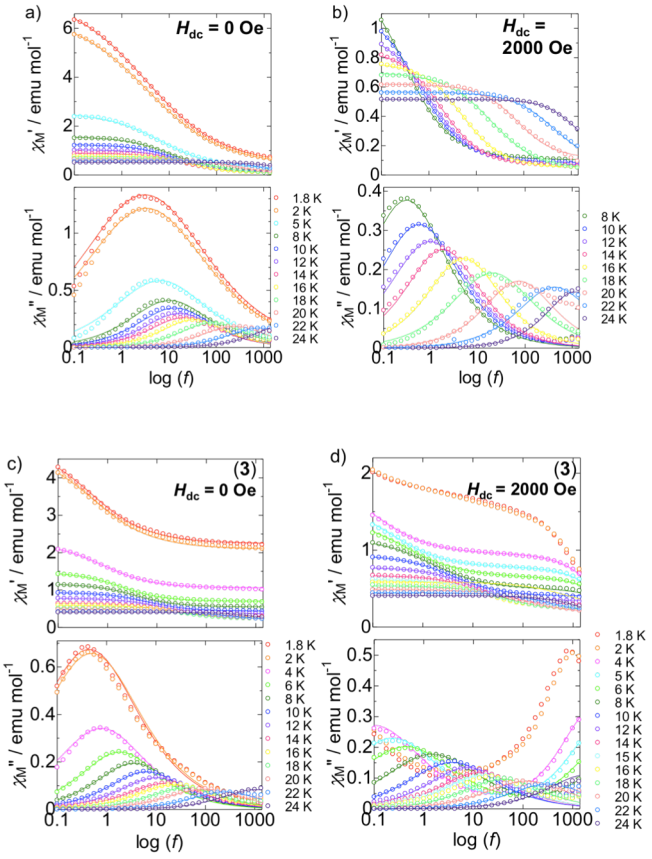

Figure 6. Frequency dependence of in-phase (χ_M') and out-of-phase (χ_M") signals of the ac magnetic susceptibility for a crystalline powder sample of **2** in (a) zero dc magnetic field and (b) 2000 Oe dc magnetic field and powder sample of **3** in (a) zero dc magnetic field and (b) 2000 Oe dc magnetic field with a 3.9 G ac field amplitude.The solid lines were fitted by using an extended Debye model. Reprinted with permission from ref. 60. Copyright 2014, Wiley.

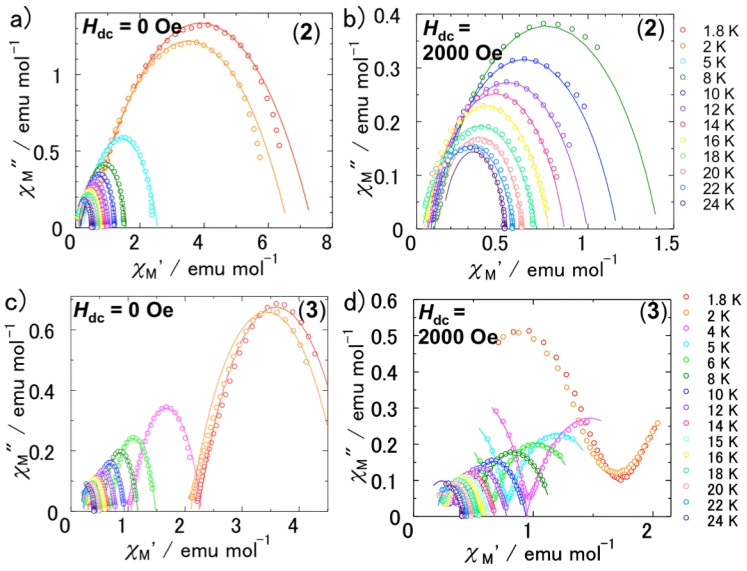

Figure 7. Argand plots for a crystalline powder sample of anionic form **2** in (a) zero dc magnetic field and (b) 2000 Oe magnetic field, and for a powder sample of radical form **3** in (c) zero dc magnetic field and (d) 2000 Oe magnetic field. The solid lines were fitted by a generalized Debye model. Reprinted with permission from ref. 60. Copyright 2014, Wiley.

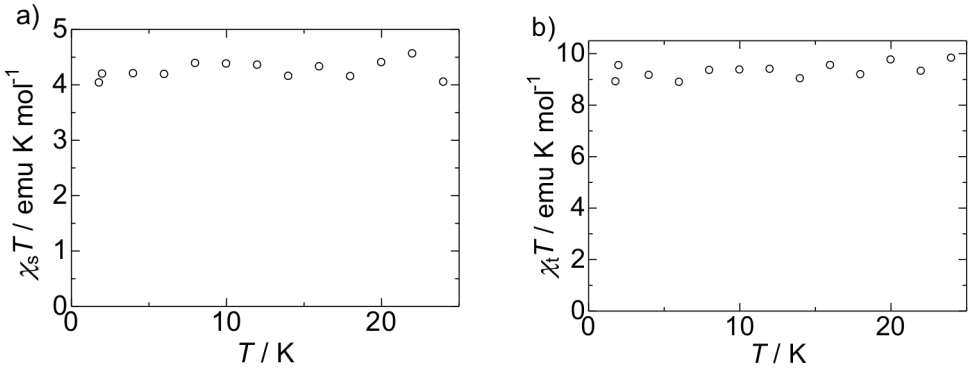

Figure 8. a) $\chi_s T$ vs. T plots and b) $\chi_t T$ vs. T plots of radical complex **3** under zero dc magnetic field. Here χ_s is the adiabatic susceptibility (high frequency regime) and χ_t is the isothermal susceptibility (low frequency regime). Reprinted with permission from ref. 60. Copyright 2014, Wiley.

increasing with increasing of the temperature although χ_t for complex **2** does not show the temperature dependency. Figure 8 shows that the $\chi_s T$ values of radical complex **3** are almost constant. This means that the shift of the χ_s in radical complex **3** is caused by a paramagnetic

component whose magnetization reversal occurs without the thermal energy barrier. The dc magnetic susceptibility measurement of anionic complex **2** and radical complex **3** was shown in Figure 9. As shown in Figure 9 the $\chi_M T$ values are constant at high temperatures, and the value of a radical form **3** is higher than that of complex **2**. The difference of the value is 0.7 emu K mol^{-1} which attributes to the presence or absence of single-electron π radical. It is expected that the π radical on the porphyrin ligands form the main paramagnetic component for χ_s. Two different kinds of relaxation process of **3** were suggested from the Argand plot under 2000 Oe dc magnetic field (Figure 7 (d)). On the other hand, an anionic complex **2** showed only one process. The unpaired π electrons which could interact with the magnetic moment of Tb^{III} center at the low temperature region might be attributed to the based species of the slow relaxation process of **3** under a dc magnetic field. The relaxation time (τ) was determined by the results of both Figure 6 and Figure 7. The estimated energy barrier between up spin state and down spin state by an Arrhenius equation $\tau^{-1} = \tau_0^{-1}\exp(-\Delta/k_B T)$ for **2** (Figure 10 (a)) was 207 cm^{-1} with a frequency factor (τ_0) of 2.38×10^{-10} s, and those for **3** were 215 cm^{-1} and 3.39×10^{-10} s (Figure 10 (b)). These values show a good agreement with the value of reported anionic form tetraphenylporphyrin double-decker complex (U_{eff} = 283 cm-1, $\tau_0 = 6.8 \times 10^{-12}$ s).

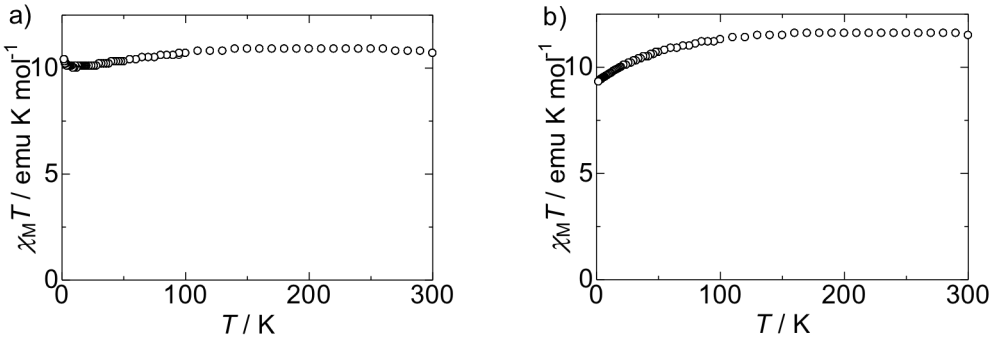

Figure 9. Temperature dependence of $\chi_M T$ for a) anionic **2** and b) radical **3** complexes. Reprinted with permission from ref. 60. Copyright 2014, Wiley.

Figure 11 shows typical butterfly shaped hysteresis which was observed by the dc magnetization measurement of both complexes **2** and **3**. The measurement condition was at 1.8 K within ± 20 kOe. The radical complex **3** showed more opened butterfly loops compared to

that of the anionic complex **2**. From the Arrhenius plot, **3** has higher energy barrier than that of **2**. This means that the relaxation time of **3** is slower than **2**, and this attributed to the shape of hysteresis.

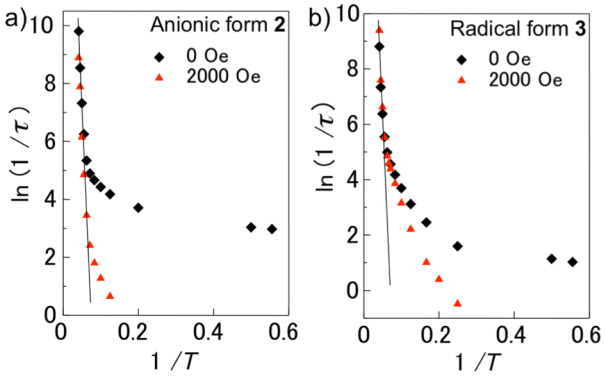

Figure 10. Arrhenius plots for (a) anionic form **2** and (b) radical form **3**. Reprinted with permission from ref. 60. Copyright 2014, Wiley.

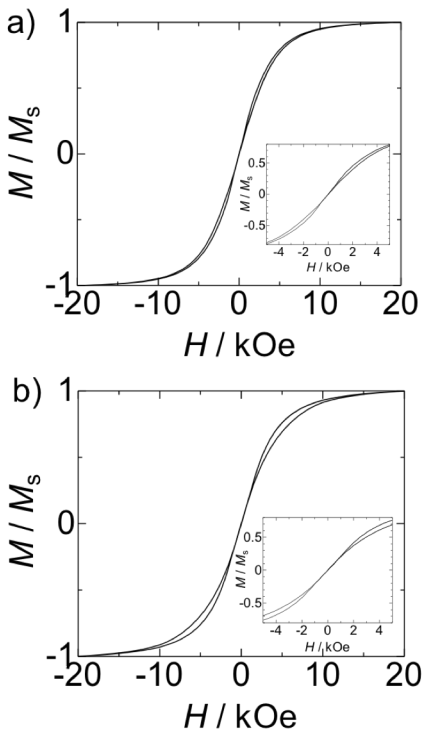

Figure 11. Hysteresis loops of the (a) anionic form **2** and (b) radical form **3** at 1.8 K. Reprinted with permission from ref. 60. Copyright 2014, Wiley.

Molecular geometry and Surface self-assembly

Fabricating homogeneous molecular thin films and controlling 2D supramolecular structures of SMMs on a surface are one of the important subjects for the future molecular spintronic devices.[57] HOPG was chosen as a substrate for the measurement in this time because the properties of HOPG are simiar to the classical nanocarbon materials, like graphene and carbon nanotubes. First, we used tetraphenylporphyrin (TPP) based double-decker complex[47] to make ordered monolayers on HOPG by the dropcasted method. However, so far we have not seen any self-assembly. There are two main conceivable factors: 1) effective adsorbate-substrate contact is reduced by non-planarity of TPP (and the adsorption strength, as a consequence), 2) gear-like topology of complex also induce further island-type growth,[47,58] especially for the protonated form ($Tb^{III}H(TTP)_2$), because of the low molecular symmetry of its double-decker core.[47] By changing $Tb(oep)_2$ as adsorbate, it is expected that realizing ordered 2D supramolecular structure of porphyrin double-decker copmlexes because 16 alkyl chains of $Tb(oep)_2$ as shown in Figure 12 would give multiple weakly-directional van der Waals interactions. This design was consequently suitable. Here we successfully observed nicely ordered molecular thin films of all three $Tb(oep)_2$ on HOPG by simple dropcasting from dichloromethane solutions. (Figure 13).

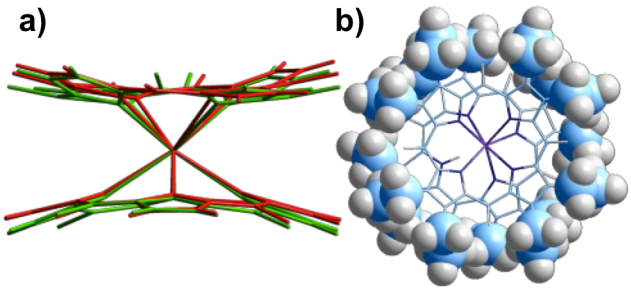

Figure 12. Molecular models of (a) differences of the double-decker cores of the protonated (red) and anionic (green) TPP-Tb^{III}double-decker complexes as dound in X-ray single crystal analysis, (b) shell of the alkyl chains in **1**. Reprinted with permission from ref. 60. Copyright 2014, Wiley.

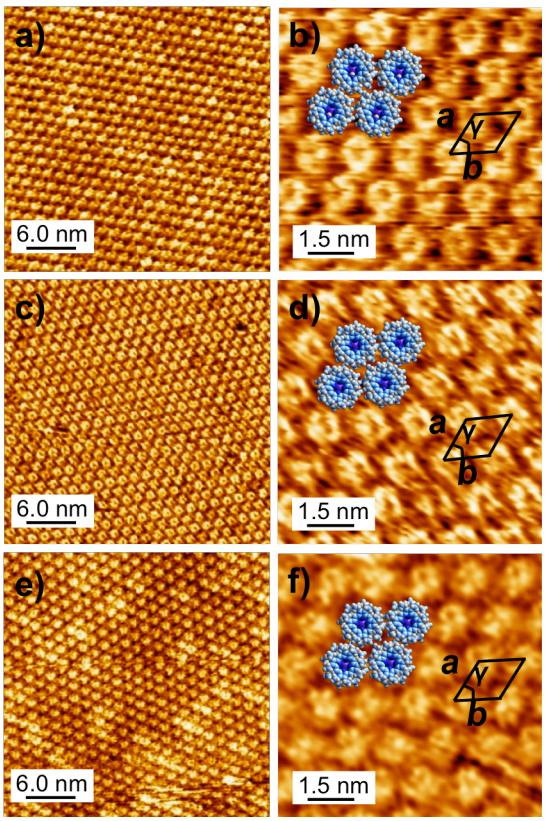

Figure 13. STM images of a), b) protonated form 1 in 7.82×10^{-5} M anhydrous CH_2Cl_2 (I = 0.200 nA, V_{sample} = −0.550 V); c), d) anionic form 2 in 5.43×10^{-5} M anhydrous CH_2Cl_2 (I = 0.220 nA, V_{sample} = 0.400 V); e), f) radical form 3 in 2.04×10^{-4} M anhydrous CH_2Cl_2 (I = 0.200 nA, V_{sample} = −0.400 V). Figures b), d) and f) also show tentative molecular models of 1, 2 and 3, respectively. Element color: hydrogens-white, carbons- light blue, nitrogens-dark blue, terbium-violet. Reprinted with permission from ref. 60. Copyright 2014, Wiley.

In STM images, **1-3** commonly appear as deformed ~1nm rings, whose shape and dimensions are good agreement with the size of one molecule and the alkyl chains. It was difficalt to recognize the difference between **1-3** from STM images because the appearance of these molecules are affected by the alkyl chains. Furthermore the counter ion of an anionic complex **2**, -protonated DBU- was not observed. However, from our solution and solid-state experiments we know that **1-3** are stable at ambient conditions. Raman spectroscopy also confirmed that the complex **2** exist stably in thin films (Figure 14).

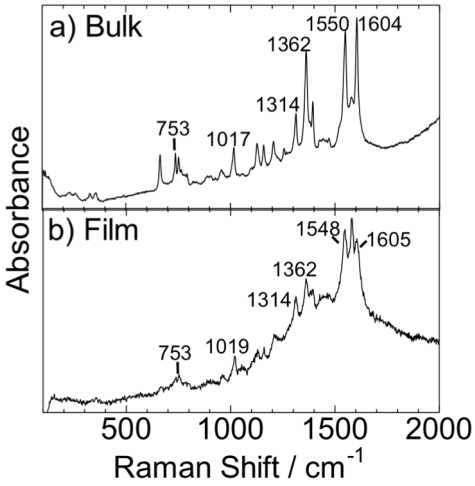

Figure 14. Raman spectra of anionic form double-decker complex measured a) in bulk state and b) on HOPG surface. Reprinted with permission from ref. 60. Copyright 2014, Wiley.

Table 1 shows the unit cells of these assemblies and **1**-**3** show essentially identical value and show close packing, because of multiple non-directional van der Waals interactions. The differences of symmetry, molecular geometry and electronic structure of the double-decker complexes are cusioned by the conformationally mobile alky chains (Figure 12).

Table 1. Lattice parameters of $Tb(oep)_2$ double-decker complexes on HOPG.

	Protonated, **1**	Anionic, **2**	Radical, **3**
a, nm	1.41 ± 0.03	1.37 ± 0.08	1.39 ± 0.04
b, nm	1.46 ± 0.05	1.41 ± 0.04	1.45 ± 0.06
γ, °	66 ± 3	64 ± 4	65 ± 3

As shown in Figure 15, it was revealed large domains of monolayers with some holes or isolated molecules in the second layer was contained in the films. Boundaries between two neighbor domains were rarely observed, and step edges or sub-monolayer coverage and defects of the underlying HOPG are the main reasons why domain borders were observed (Figure 16). Furthermore, even when we deposited mixture sample of **1** and **2**, interdomain boundaries were not observed (Figure 17).

Not only simple close packing 2D supramolecular structure of SMMs, but also other surface structures are also possible as long as strong interactions between substrate and

molecules are maintained. One example is designed molecule **4** which has long alkyl chains (Figure 18(a)). Destabilizing possible porous packing of this can remove the possibility of polymorphism.[59] Figure 18b and c shows ordered monolayers of **4** which was observed by dropcasting from dilute DCM solutions. Here self-assembly on HOPG was stabilized by long alkyl chains. Furthermore, the long alkyl chains also play an important role as a spacer to separate neighbor Tb^{III} sites.

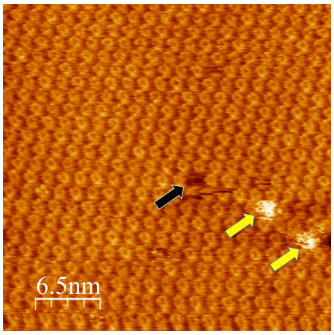

Figure 15. Representative STM image of single-molecule defects in monolayers of OEB-Tb complexes. This is self-assembly of **1** (I = 0.05 nA, V_{sample} = −0.600 V). Black and yellow arrows point to a hole and second-layer molecules, respectively. Reprinted with permission from ref. 60. Copyright 2014, Wiley.

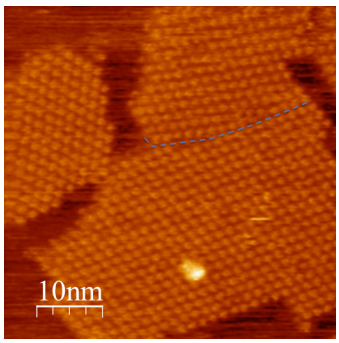

Figure 16. Rare observation of interdomain boundary (marked with blue dotted line) and multiple domain borders formed as a consequence of submonolayer coverage in OEB-Tb assemblies. This is self-assembly of **1** (I = 0.15 nA, V_{sample} = −0.800 V). Reprinted with permission from ref. 60. Copyright 2014, Wiley.

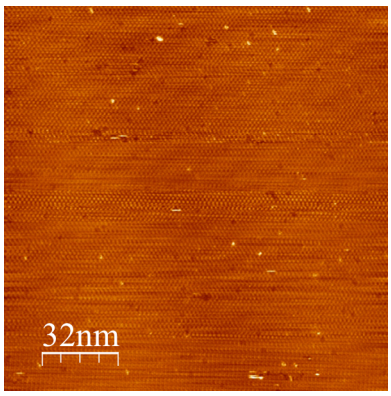

Figure 17. Very large domain of 1:1 mixture of protonated (**1**) and anionic (**2**) complexes (I = 0.15 nA, V_{sample} = −0.800 V). There is no aparent phase separation. Reprinted with permission from ref. 60. Copyright 2014, Wiley.

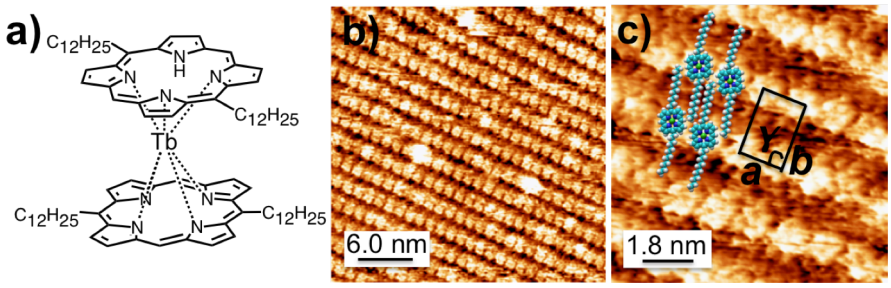

Figure 18. a) Molecular structure of BDP-Tb^{III} double-decker complex **4**. STM images of b), c) protonated BDP-Tb^{III} double-decker complex **4** in 9.26 × 10^{-5} M anhydrous CH_2Cl_2 (I = 0.080 nA, V_{sample} = 1.000 V). The lattice parameter is a = 2.16 ± 0.03 nm, b = 1.22 ± 0.02 nm and γ = 85 ± 3°. Molecular models of freebase BDP are superimposed on the image. The actual angle between upper and lower porphyrin plane is not clear, so molecular models of freebase porphyrin are shown. Reprinted with permission from ref. 60. Copyright 2014, Wiley.

4-3 Conclusions

In this report, the synthesis method and magnetic property of $Tb(oep)_2$ with three different electronic structures were performed. It was revealed that non-SMM properties of the protonated form of the $Tb(oep)_2$ from the ac magnetic susceptibility measurement. The reason of the non-SMM properties of $Tb(oep)_2$ contributes to the molecular symmetry of a protonated form double-decker complex was lower. To the best of our knowledge, such a drastic magnetic switching among three different electronic structures was reported for the first time.

As the next step towards the development of actual spintronic devices, we have studied surface self-assembly of several Tb complexes as a way to form thin films with different patterned arrangement of SMM active sites. Furthermore, rich chemistry (acid-base, redox) and close similarity between the packing of $Tb(oep)_2$ set promising foundation for the development of multifunctional and morphologically stable SMM switches and sensors. Currently, we are exploring chemical reactivity of monolayers and ultrathin films of these and other Tb complexes aiming at the *in-situ* interconversion (switching).

Finally, from the above results it is expected that our approach in this time can affect the study for future molecular spintronic devices including SMM/nanocarbon material composites.

References

(1) Bogani, L.; Wernsdorfer, W. *Nat. Mater.* **2008**, *7*, 179.

(2) Sessoli, R.; Gatteschi, D.; Caneschi, A.; Novak, M. A. *Nature* **1993**, *365*, 141.

(3) Cornia, A.; Mannini, M.; Sainctavit, P.; Sessoli, R. *Chem. Soc. Rev.* **2011**, *40*, 3076.

(4) Glaser, T. *Chem. Commun.* **2011**, *47*, 116.

(5) Miller, J. S.; Gatteschi, D. *Chem. Soc. Rev.* **2011**, *40*, 3065.

(6) Rinehart, J. D.; Long, J. R. *Chem. Sci.* **2011**, *2*, 2078.

(7) Sanvito, S. *Chem. Soc. Rev.* **2011**, *40*, 3336.

(8) Sorace, L.; Benelli, C.; Gatteschi, D. *Chem. Soc. Rev.* **2011**, *40*, 3092.

(9) Domingo, N.; Bellido, E.; Ruiz-Molina, D. *Chem. Soc. Rev.* **2012**, *41*, 258.

(10) Jeon, I. R.; Clerac, R. *Dalton Trans.* **2012**, *41*, 9569.

(11) Habib, F.; Murugesu, M. *Chem. Soc. Rev.* **2013**, *42*, 3278.

(12) Ishikawa, N.; Sugita, M.; Ishikawa, T.; Koshihara, S.; Kaizu, Y. *J. Am. Chem. Soc.* **2003**, *125*, 8694.

(13) Ishikawa, N.; Sugita, M.; Tanaka, N.; Ishikawa, T.; Koshihara, S. Y.; Kaizu, Y. *Inorg. Chem.* **2004**, *43*, 5498.

(14) Takamatsu, S.; Ishikawa, T.; Koshihara, S. Y.; Ishikawa, N. *Inorg. Chem.* **2007**, *46*, 7250.

(15) Katoh, K.; Horii, Y.; Yasuda, N.; Wernsdorfer, W.; Toriumi, K.; Breedlove, B. K.; Yamashita, M. *Dalton Trans* **2012**, *41*, 13582.

(16) Wang, H.; Wang, K.; Tao, J.; Jiang, J. *Chem Commun (Camb)* **2012**, *48*, 2973.

(17) Fukuda, T.; Matsumura, K.; Ishikawa, N. *The journal of physical chemistry. A* **2013**, *117*, 10447.

(18) Wang, K.; Qi, D.; Wang, H.; Cao, W.; Li, W.; Liu, T.; Duan, C.; Jiang, J. *Chemistry* **2013**, *19*, 11162.

(19) Heersche, H. B.; de Groot, Z.; Folk, J. A.; van der Zant, H. S. J.; Romeike, C.; Wegewijs, M. R.; Zobbi, L.; Barreca, D.; Tondello, E.; Cornia, A. *Phys. Rev. Lett.* **2006**, *96*, 206801.

(20) Zyazin, A. S.; van den Berg, J. W. G.; Osorio, E. A.; van der Zant, H. S. J.; Konstantinidis, N. P.; Leijnse, M.; Wegewijs, M. R.; May, F.; Hofstetter, W.; Danieli, C.; Cornia, A. *Nano Lett.* **2010**, *10*, 3307.

(21) Komeda, T.; Isshiki, H.; Liu, J.; Zhang, Y. F.; Lorente, N.; Katoh, K.; Breedlove, B. K.; Yamashita, M. *Nat. Commun.* **2011**, *2*, 217.

(22) Robles, R.; Lorente, N.; Isshiki, H.; Liu, J.; Katoh, K.; Breedlove, B. K.; Yamashita, M.; Komeda, T. *Nano Lett.* **2012**, *12*, 3609.

(23) Vincent, R.; Klyatskaya, S.; Ruben, M.; Wernsdorfer, W.; Balestro, F. *Nature* **2012**, *488*, 357.

(24) Urdampilleta, M.; Klyatskaya, S.; Cleuziou, J. P.; Ruben, M.; Wernsdorfer, W. *Nat. Mater.* **2011**, *10*, 502.

(25) Candini, A.; Klyatskaya, S.; Ruben, M.; Wernsdorfer, W.; Affronte, M. *Nano Lett.* **2011**, *11*, 2634.

(26) Mannini, M.; Pineider, F.; Sainctavit, P.; Danieli, C.; Otero, E.; Sciancalepore, C.; Talarico, A. M.; Arrio, M. A.; Cornia, A.; Gatteschi, D.; Sessoli, R. *Nat. Mater.* **2009**, *8*, 194.

(27) Mannini, M.; Pineider, F.; Danieli, C.; Totti, F.; Sorace, L.; Sainctavit, P.; Arrio, M. A.; Otero, E.; Joly, L.; Cezar, J. C.; Cornia, A.; Sessoli, R. *Nature* **2010**, *468*, 417.

(28) Margheriti, L.; Chiappe, D.; Mannini, M.; Car, P. E.; Sainctavit, P.; Arrio, M. A.; de Mongeot, F. B.; Cezar, J. C.; Piras, F. M.; Magnani, A.; Otero, E.; Caneschi, A.; Sessoli, R. *Adv. Mater.* **2010**, *22*, 5488.

(29) Stepanow, S.; Honolka, J.; Gambardella, P.; Vitali, L.; Abdurakhmanova, N.; Tseng, T. C.; Rauschenbach, S.; Tait, S. L.; Sessi, V.; Klyatskaya, S.; Ruben, M.; Kern, K. *J. Am. Chem. Soc.* **2010**, *132*, 11900.

(30) Gonidec, M.; Biagi, R.; Corradini, V.; Moro, F.; De Renzi, V.; del Pennino, U.; Summa, D.; Muccioli, L.; Zannoni, C.; Amabilino, D. B.; Veciana, J. *J. Am. Chem. Soc.* **2011**, *133*, 6603.

(31) Barth, J. V.; Costantini, G.; Kern, K. *Nature* **2005**, *437*, 671.

(32) Barth, J. V. *Annu. Rev. Phys. Chem.* **2007**, *58*, 375.

(33) Bartels, L. *Nat. Chem.* **2010**, *2*, 87.

(34) Tahara, K.; Lei, S. B.; Adisoejoso, J.; De Feyter, S.; Tobe, Y. *Chem. Commun.* **2010**, *46*, 8507.

(35) Joseph, E. A.; Ye, T. *ACS Nano* **2013**, *7*, 3653.

(36) Binnig, G.; Rohrer, H.; Gerber, C.; Weibel, E. *Phys. Rev. Lett.* **1982**, *49*, 57.

(37) Binnig, G.; Quate, C. F.; Gerber, C. *Phys. Rev. Lett.* **1986**, *56*, 930.

(38) Miyake, Y.; Nagata, T.; Tanaka, H.; Yamazaki, M.; Ohta, M.; Kokawa, R.; Ogawa, T. *ACS Nano* **2012**, *6*, 3876.

(39) Katsonis, N.; Lacaze, E.; Feringa, B. L. *J. Mater. Chem.* **2008**, *18*, 2065.

(40) Elemans, J. A. A. W.; De Cat, I.; Xu, H.; De Feyter, S. *Chem. Soc. Rev.* **2009**, *38*, 722.

(41) Tahara, K.; Yamaga, H.; Ghijsens, E.; Inukai, K.; Adisoejoso, J.; Blunt, M. O.; De Feyter, S.; Tobe, Y. *Nat. Chem.* **2011**, *3*, 714.

(42) Mali, K. S.; Adisoejoso, J.; Ghijsens, E.; De Cat, I.; De Feyter, S. *Acc. Chem. Res.* **2012**, *45*, 1309.

(43) Elemans, J. A. A. W.; Lei, S. B.; De Feyter, S. *Angew. Chem., Int. Ed.* **2009**, *48*, 7298.

(44) Takami, T.; Ye, T.; Pathem, B. K.; Arnold, D. P.; Sugiura, K.; Bian, Y. Z.; Jiang, J. Z.; Weiss, P. S. *J. Am. Chem. Soc.* **2010**, *132*, 16460.

(45) Tierney, H. L.; Murphy, C. J.; Jewell, A. D.; Baber, A. E.; Iski, E. V.; Khodaverdian, H. Y.; McGuire, A. F.; Klebanov, N.; Sykes, E. C. H. *Nat. Nanotechnol.* **2011**, *6*, 625.

(46) den Boer, D.; Li, M.; Habets, T.; Iavicoli, P.; Rowan, A. E.; Nolte, R. J. M.; Speller, S.; Amabilino, D. B.; De Feyter, S.; Elemans, J. A. A. W. *Nat. Chem.* **2013**, *5*, 621.

(47) Tanaka, D.; Inose, T.; Tanaka, H.; Lee, S.; Ishikawa, N.; Ogawa, T. *Chem. Commun.* **2012**, *48*, 7796.

(48) Inose, T.; Tanaka, D.; Ogawa, T. *Heterocycles* **2012**, *86*, 1549.

(49) Donohoe, R. J.; Duchowski, J. K.; Bocian, D. F. *J. Am. Chem. Soc.* **1988**, *110*, 6119.

(50) Buchler, J. W.; Scharbert, B. *J. Am. Chem. Soc.* **1988**, *110*, 4272.

(51) Buchler, J. W.; Hüttermann, J.; Löffler, J. *Bull. Chem. Soc. Jpn.* **1988**, *61*, 71.

(52) Duchowski, J. K.; Bocian, D. F. *J. Am. Chem. Soc.* **1990**, *112*, 3312.

(53) Spyroulias, G. A.; Raptopoulou, C. P.; de Montauzon, D.; Mari, A.; Poilblanc, R.; Terzis, A.; Coutsolelos, A. G. *Inorg. Chem.* **1999**, *38*, 1683.

(54) Kadish, K. M.; Morrison, M. M. *J. Am. Chem. Soc.* **1976**, *98*, 3326.

(55) Chang, C. K.; Barkigia, K. M.; Hanson, L. K.; Fajer, J. *J. Am. Chem. Soc.* **1986**, *108*, 1352.

(56) Gatteschi, D.; Sessoli, R.; Villain, J.; Oxford University Press: New York, 2006; Vol. 1.

(57) Cavallini, M.; Facchini, M.; Albonetti, C.; Biscarini, F. *Phys. Chem. Chem. Phys.* **2008**, *10*, 784.

(58) Meyer, E. A.; Castellano, R. K.; Diederich, F. *Angew. Chem., Int. Ed.* **2003**, *42*, 1210.

(59) Klymchenko, A. S.; Sleven, J.; Binnemans, K.; De Feyter, S. *Langmuir* **2006**, *22*, 723.

(60) Inose, T.; Tanaka, D.; Tanaka, H.; Ivasenko, O.; Nagata, T.; Ohta, Y.; De Feyter, S.; Ishikawa, N.; Ogawa, T. *Chem. Eur. J.* **2014**, *20*, 11362.

Chapter V Fabricating the New 2D Supramolecular Structure of Single-Molecule Magnet on a Carbon Surface

5-1 Introduction

Single-molecule magnets (SMMs) are one of the very attractive functional molecules because of their unique energy barrier to magnetic relaxation and their high possibility to apply to molecular spintronics.[1-5] In particular, the family of phthalocyanine (Pc)-based Tb^{III} double-decker complexes ($TbPc_2$) displays higher blocking temperatures and a number of studies on Pc double-decker SMMs have been reported.[6] One of the interesting researches in this field in recent years is attractive nanocarbon/SMM composites -$TbPc_2$ derivatives on nanocarbon materials- for spintronic devices.[7,8] In these studies spin valve effects play an important role and the magnetic state of SMMs on nanocarbon materials by electrical signals has already been successfully detected. Thus the research of nanocarbon/SMM composites is of great interest to realize any technological application of SMMs like high-density data storage. Controlling two-dimensional (2D) supramolecular structure on a surface seems very important for such nanocarbon/SMMs composites, although there are few reports about 2D structure of SMM at one molecular level.[9,10] Fabricating 2D supramolecular organizations properly is very important for a next step to realize SMM application.

In our past study we have focused on porphyrin-Tb^{III} double-decker (Por-DD) SMMs because of their high functional group tunability and unique proton-induced magnetic switching properties.[11] Previously we have been succeeded in making both regular 1D and 2D supramolecular structure of Por-DD complexes with such attractive magnetic switching property on highly oriented pyrolytic graphite (HOPG) surface by introducing alkyl groups to porphyrin to enhance the interaction between the molecule and HOPG surface.[12] In the previous study surface-confined 2D supramolecular structure of Por-DD on HOPG was measured by scanning tunneling microscopy (STM) under an ambient condition. STM is one of the very powerful tools to investigate 2D molecular networks for structural evaluation at submolecular level and many 2D supramolecular structures have been measured by STM under several measurement environments.[13-22] From the viewpoint of realizing new 2D supramolecular

structure on a surface, using two-component on a surface is one of the very attractive methods.[13,14,19,23-26]

Here we demonstrate new supramolecular structure of SMM on HOPG. We propose alkoxylated dehydrobenzo [12] annulene (DBA) derivatives as an attractive molecule to realize new 2D surface structure of SMM on HOPG.[23-26] A part of authors reported that DBA derivatives showed a unique porous network formation at the liquid-solid interface based on alkyl chain interdigitation interaction (van dear Waals interaction) between adjacent molecules. These 2D porous networks give the potential to immobilize functional units as guest molecules in a repetitive and spatially ordered arrangement. So two-component of SMMs and DBA molecules with appropriate alkyl chain length can make a new 2D structure on a surface. In this paper we used a radical form 2,3,7,8,12,13,17,18-octaethylporphyrin (OEP)-Tb^{III} double-decker ($Tb^{III}(oep)_2$) SMM as a guest molecule and demonstrate a method to realize new 2D supramolecular structure of SMM on a surface by using a DBA molecule. Concentration dependence of $Tb^{III}(oep)_2$ co-adsorbed with DBA cores on a surface was also observed and such results will be one possibility to control SMM density on carbon materials.

5-2 Experimental

Radical form 2,3,7,8,12,13,17,18-octaethylporphyrin (OEP)-Tb^{III} double-decker complex was synthesized by previously reported procedure.[12]

All STM measurements were performed at room temperature using a Multimode 8 setup equipped with a NanoScope V controller (Bruker Nano Inc., Nano Surfaces Devision, Santa Barbara, CA, USA). The experiments were operated in constant-current mode with the tip immersed in the supernatant liquid. STM tips were prepared by mechanical cutting of Pt/Ir wire (80%/20%, diameter 0.25 nm).

Prior to imaging, the complexes under investigation were dissolved in 1-Phenyloctane (Wako) at each concentration, and 20 ml of this solution was casted on a freshly cleaved surface of HOPG (grade ZYB, GE Advanced Ceramics). All STM images were taken in constant-current mode. The bias voltage was applied to the sample in such a way that at positive

bias voltage, electrons tunnel from the tip to the sample. All images were filtered by using NanoScope Analysis.

To investigate host-guest systems, the solution of the host molecules in 1-Phenyloctane (20ml, 3.7×10^{-5} M) was first measured to confirm the network structure, and then a 20 ml of the solution of a guest molecule (4.5×10^{-6} M, 1.3×10^{-5} M, 2.1×10^{-5} M, 2.7×10^{-5} M, 3.5×10^{-5} M) of each concentration was added to the sample. For each concentration of a guest molecule, around ten large-scale STM images (100×100 nm^2) were measured to obtain a percentage of the guest molecule to the total number of the host molecule in the area.

5-3 Results and Discussions

The systems presented here consist of combinations of DBA with octyloxy (DBA-OC8) chains and a radical form $Tb^{III}(oep)_2$ as a guest molecule at the liquid/solid interface on HOPG (see Scheme 1(a), (b) for molecular structures). In our previous study it was revealed that an anionic form and a radical form $Tb^{III}(oep)_2$ showed similar SMM property compared to other reported porphyrin double-dekcer SMMs in bulk state, and these complexes also showed unique proton-induced magnetic switching.[12] A STM study of $Tb^{III}(oep)_2$ with three different electronic

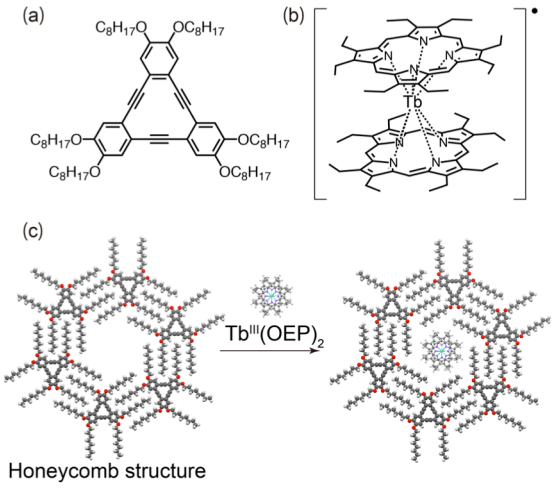

Scheme 1. Chemical structure of (a) DBA-OC8 and (b) radical form $Tb^{III}(oep)_2$. (c) Tentative models of the surface patterns. Left; one component (only DBA-OC8), Right; two components (DBA-OC8 and $Tb^{III}(oep)_2$).

structures revealed that these complexes showed stable pseudo-hexagonal packing structure with almost same lattice parameter under an ambient condition (the lattice parameter of a radical form $Tb^{III}(oep)_2$; a = 1.39 ± 0.04 nm, b = 1.45 ± 0.06 nm, g = 65 ± 3°) on HOPG. From the previous study it is expected that the radical form $Tb^{III}(oep)_2$ can be one of the appropriate SMMs as a guest molecule for DBA networks because $Tb^{III}(oep)_2$ is planar and neutral molecule. We selected a DBA molecule with octyloxy chains because the molecular modeling calculation expected that the porous size formed by a hexamer of DBA-OC8 (edge to edge distance) is 18.08 Å. This size seems to be best fitted to the size of one radical form $Tb^{III}(oep)_2$ molecule whose size on HOPG is estimated around 15 Å.[12] From the tentative model of the honeycomb structure of DBA-OC8, one radical form $Tb^{III}(oep)_2$ molecule can fit in one pore (Scheme 1(c)).

First only the solution of DBA-OC8 molecules in 1-Phenyloctane (20 ml, 3.7×10^{-5} M) was casted on HOPG (5×5 nm^2) and the 2D structure at the solid/liquid interface was measured to confirm the formation of the nanoporous network structure. Figure 2(a) shows the STM image of only DBA-OC8 on HOPG. The DBA moieties appear as bright features due to the unsaturated annulene core, and alkoxy chains appear as darker lines between adjacent DBA cores. The observed honeycomb-type network structure is similar to the one which has been observed in TCB and other solvent in the past study. Through all experiments here the concentration of DBA-OC8 solution was constant 3.7×10^{-5} M. After confirmation of honeycomb structure of DBA-OC8 on HOPG the five different kinds of concentration of a radical form $Tb^{III}(oep)_2$ in 1-Phenyloctane (guest molecule) was dropped on DBA-OC8 porous network. The concentration of a radical form $Tb^{III}(oep)_2$ solution was changed from the lowest 4.5×10^{-6} M to the highest 3.5×10^{-5} M. Figures 2(b)-(f) show STM images of two component (DBA-OC8/ $Tb^{III}(oep)_2$). Some bright spots in cavities of DBA-OC8 were observed after the $Tb^{III}(oep)_2$ solution was added to the honeycomb network structure. The number of bright spots seems to be increasing with the increasing of the concentration of radical form $Tb^{III}(oep)_2$ solution. Because only the number of

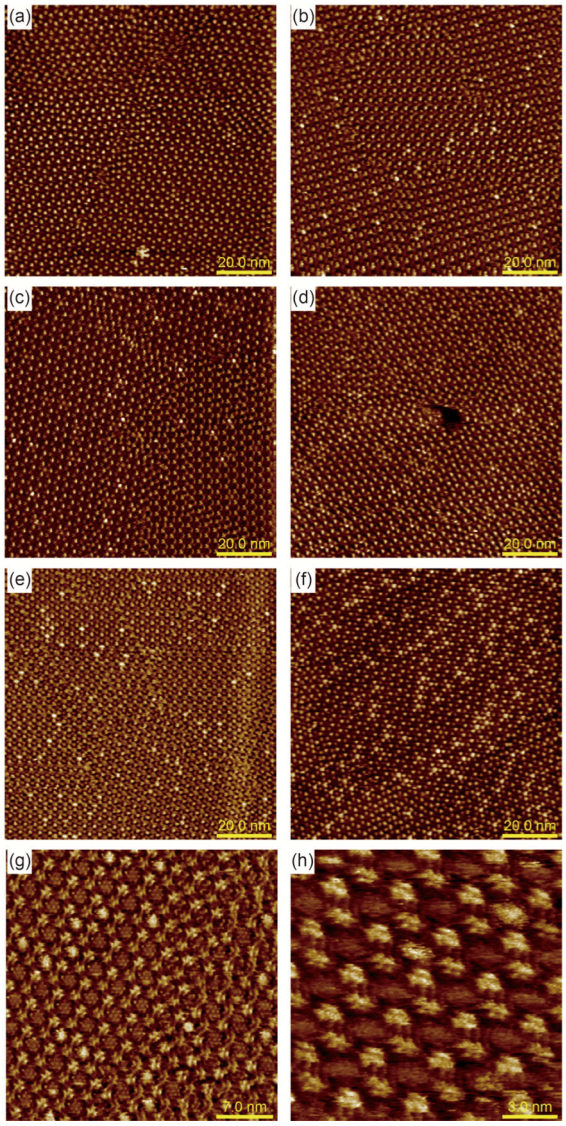

Figure 2. Large-area STM images (100 × 100 nm^2) of the network structures of DBA-OC8 with or without $Tb^{III}(oep)_2$. Same amount of the solution of DBA-OC8 in 1-Phenyloctane (20 ml, C_{DBA} = 3.7 × 10^{-5} M) was casted on HOPG through all samples. 20 ml of the solution of (a) $C_{Tb(oep)2}$ = 0 M (I_t = 66.04 pA, V_{sample} = 799.7 mV), (b) $C_{Tb(oep)2}$ = 4.5 × 10^{-6} M (I_t = 100.00 pA, V_{sample} = 649.7 mV), (c) $C_{Tb(oep)2}$ = 1.3 × 10^{-5} M (I_t = 110.00 pA, V_{sample} = 670.0 mV), (d) $C_{Tb(oep)2}$ = 2.1 × 10^{-5} M(I_t = 500.00 pA, V_{sample} = 700.0 mV), (e) $C_{Tb(oep)2}$ = 2.7 × 10^{-5} M (I_t = 70.00 pA, V_{sample} = 699.8 mV), (f) $C_{Tb(oep)2}$ = 3.5 × 10^{-5} M (I_t = 38.72 pA, V_{sample} = 713.5 mV) of $Tb^{III}(OEP)_2$ were casted on HOPG. (g), (h) Zoomed STM image of the honeycomb network of DBA-OC8 with $Tb^{III}(oep)_2$. (g) $C_{Tb(oep)2}$ = 2.5 × 10^{-5} M, 35 × 35 nm^2, (I_t = 66.04 pA, V_{sample} = 686.9 mV) (h) $C_{Tb(oep)2}$ = 4.6 × 10^{-6} M, 15 × 15 nm^2 (I_t = 44.42 pA, V_{sample} = 662.3 mV)

a radical form $Tb^{III}(oep)_2$ molecule in solution was changed, it is expected that the bright spots in cavities indicate co-adsorbed radical form $Tb^{III}(oep)_2$ molecules. Figures 2(g) and (h) show a zoomed STM image of two component (DBA-OC8/$Tb^{III}(oep)_2$). Clear DBA moieties as triangular features and brighter spots than those of DBA moieties but fuzzy spots appear in the cavities. Because the molecular height of $Tb^{III}(oep)_2$ is high more than double for that of DBA-OC8, the brighter feature inside the cavities is strong evidence for the coadsorption of radical form $Tb^{III}(oep)_2$ molecules.

The concentration dependence of the proportion of coadsorbed radical form $Tb^{III}(oep)_2$ in the cavities to all cavities in entire area (100 × 100 nm^2) is shown in Figure 3. The number of

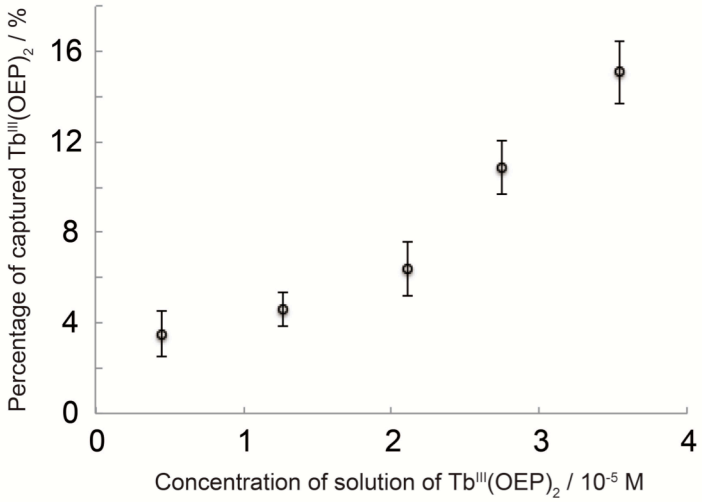

Figure 3. Plot of the ratio of captured $Tb^{III}(oep)_2$ to all cavities by formed DBA-OC8 versus the concentration of solution of $Tb^{III}(oep)_2$.

both bright spots and cavities formed by DBA-OC8 was confirmed by visual check. In Figure 3, the proportion of captured radical form $Tb^{III}(oep)_2$ apparently increases with increasing the concentration of radical form $Tb^{III}(oep)_2$ solution. When linear approximation whose Y-intercept is 0, larger deviations from the straight line was observed at the lowest concentration of 4.5×10^{-6} M. Even when the sample of one component of only DBA-OC8 solution (the concentration of a radical form $Tb^{III}(oep)_2$ is 0 M), a few bright spots in cavities were found (Figure S1). In all experiments here, only ~ 2% of DBA-OC8 are adsorbed on HOPG surface and the rest of molecules exist in 1-Phenyloctane solution. So some of the

observed bright spots in this experiments could be co-adsorbed DBA-OC8. Indeed previous study showed DBA derivatives itself in solution also could be guest molecules and captured in cavity formed by DBA.[23,27] In lower concentration range of a radical form $Tb^{III}(oep)_2$ (4.5×10^{-6} M), the effect of the number of co-adsorbed DBA-OC8 in cavity can not negligible and the percentage of captured radical form $Tb^{III}(oep)_2$ became higher than expected value from linear approximation.

In the concentration range of a radical form $Tb^{III}(oep)_2$ solution from 1.3×10^{-5} M to 3.5×10^{-5} M, the proportion of co-adsorbed radical form $Tb^{III}(oep)_2$ to all radical form $Tb^{III}(oep)_2$ in solution is around 0.07 % and it seems so much low coverage. Furthermore some radical form $Tb^{III}(oep)_2$ domains observed when the highest concentration of radical form $Tb^{III}(oep)_2$ of 3.5×10^{-5} M (Figure 4). Previously it was reported that in case of two-component of coronene (1.8×10^{-3} M) and DBA-OC6 (6.5×10^{-5} M), around 25% of the DBA-OC6 pores were occupied by coronene and monocomponent networks were never observed on HOPG.[26] It is considered coronene is one of the best molecules as a guest molecule because of its planar p-conjugated core with C_6 symmetry, which should fit into the hexagonal cavities of honeycomb network. The symmetry of downside porphyrin of $Tb^{III}(oep)_2$ is C_4 symmetry, and smaller desorption energies of $Tb^{III}(oep)_2$ molecules from HOPG effect the formation of monocomponent networks of $Tb^{III}(oep)_2$.

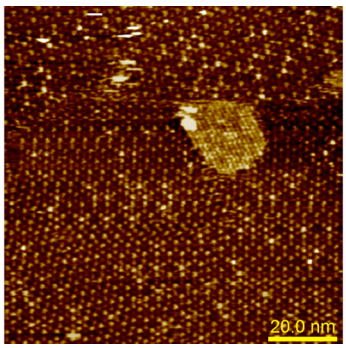

Figure 4. STM images of two domains of both DBA-OC8 and $Tb^{III}(oep)_2$.

5-4 Conclusions

In conclusion we demonstrated new 2D supramolecular structure of a radical form $Tb^{III}(oep)_2$ SMM on HOPG by using DBA molecule as a template. $Tb^{III}(oep)_2$ solution of several kinds of concentration was dropped on honeycomb-based porous network structure and the concentration dependence of radical form $Tb^{III}(oep)_2$ which was captured as guest molecules was observed. Increasing of the proportion of co-adsorbed radical form $Tb^{III}(oep)_2$ with increasing the concentration of radical form $Tb^{III}(oep)_2$ solution was successfully observed. Two-component method we showed here (DBA-OC8 as a host molecule and $Tb^{III}(oep)_2$ SMM as a guest molecule) can be one of the potential candidates to control SMM density on a surface precisely.

References

(1) Christou, G.; Gatteschi, D.; Hendrickson, D. N.; Sessoli, R. *Mrs Bull* **2000**, *25*, 66.

(2) Bogani, L.; Wernsdorfer, W. *Nat. Matter.* **2008**, *7*, 179.

(3) Rinehart, J. D.; Long, J. R. *Chem. Sci.* **2011**, *2*, 2078.

(4) Domingo, N.; Bellido, E.; Ruiz-Molina, D. *Chem. Soc. Rev.* **2012**, *41*, 258.

(5) Woodruff, D. N.; Winpenny, R. E.; Layfield, R. A. *Chem Rev* **2013**, *113*, 5110.

(6) Ishikawa, N.; Sugita, M.; Ishikawa, T.; Koshihara, S. Y.; Kaizu, Y. *J. Am. Chem. Soc.* **2003**, *125*, 8694.

(7) Candini, A.; Klyatskaya, S.; Ruben, M.; Wernsdorfer, W.; Affronte, M. *Nano Lett.* **2011**, *11*, 2634.

(8) Urdampilleta, M.; Klyatskaya, S.; Cleuziou, J. P.; Ruben, M.; Wernsdorfer, W. *Nat. Matter.* **2011**, *10*, 502.

(9) Cavallini, M.; Biscarini, F.; Gomez-Segura, J.; Ruiz, D.; Veciana, J. *Nano Lett.* **2003**, *3*, 1527.

(10) Gonidec, M.; Biagi, R.; Corradini, V.; Moro, F.; De Renzi, V.; del Pennino, U.; Summa, D.; Muccioli, L.; Zannoni, C.; Amabilino, D. B.; Veciana, J. *J. Am. Chem. Soc.* **2011**, *133*, 6603.

(11) Tanaka, D.; Inose, T.; Tanaka, H.; Lee, S.; Ishikawa, N.; Ogawa, T. *Chem. Commun.* **2012**, *48*, 7796.

(12) Inose, T.; Tanaka, D.; Tanaka, H.; Ivasenko, O.; Nagata, T.; Ohta, Y.; De Feyter, S.; Ishikawa, N.; Ogawa, T. *Chem. Eur. J.* **2014**, *20*, 11362.

(13) Griessl, S. J.; Lackinger, M.; Jamitzky, F.; Markert, T.; Hietschold, M.; Heckl, W. M. *Langmuir : the ACS journal of surfaces and colloids* **2004**, *20*, 9403.

(14) Stepanow, S.; Lingenfelder, M.; Dmitriev, A.; Spillmann, H.; Delvigne, E.; Lin, N.; Deng, X.; Cai, C.; Barth, J. V.; Kern, K. *Nat. Matter.* **2004**, *3*, 229.

(15) Gyarfas, B. J.; Wiggins, B.; Zosel, M.; Hipps, K. W. *Langmuir : the ACS journal of surfaces and colloids* **2005**, *21*, 919.

(16) Samori, P. *Chem. Soc. Rev.* **2005**, *34*, 551.

(17) Lei, S.; Tahara, K.; De Schryver, F. C.; Van der Auweraer, M.; Tobe, Y.; De Feyter, S. *Angew. Chem. Int. Ed.* **2008**, *120*, 3006.

(18) Lackinger, M.; Heckl, W. M. *Langmuir : the ACS journal of surfaces and colloids* **2009**, *25*, 11307.

(19) Blunt, M. O.; Russell, J. C.; Champness, N. R.; Beton, P. H. *Chem. Commun.* **2010**, *46*, 7157.

(20) Otsuki, J. *Coord. Chem. Rev.* **2010**, *254*, 2311.

(21) Komeda, T.; Isshiki, H.; Liu, J.; Zhang, Y. F.; Lorente, N.; Katoh, K.; Breedlove, B. K.; Yamashita, M. *Nat. Commun.* **2011**, *2*, 217.

(22) Shi, Z.; Liu, J.; Lin, T.; Xia, F.; Liu, P. N.; Lin, N. *J. Am. Chem. Soc.* **2011**, *133*, 6150.

(23) Tahara, K.; Furukawa, S.; Uji-i, H.; Uchino, T.; Ichikawa, T.; Zhang, J.; Mamdouh, W.; Sonoda, M.; De Schryver, F. C.; De Feyter, S.; Tobe, Y. *J. Am. Chem. Soc.* **2006**, *128*, 16613.

(24) Furukawa, S.; Tahara, K.; De Schryver, F. C.; Van der Auweraer, M.; Tobe, Y.; De Feyter, S. *Angew. Chem. Int. Ed.* **2007**, *119*, 2889.

(25) Tahara, K.; Lei, S.; Adisoejoso, J.; De Feyter, S.; Tobe, Y. *Chem. Commun.* **2010**, *46*, 8507.

(26) Balandina, T.; Tahara, K.; Sandig, N.; Blunt, M. O.; Adisoejoso, J.; Lei, S.; Zerbetto, F.; Tobe, Y.; De Feyter, S. *ACS Nano* **2012**, *6*, 8381.

(27) Ghijsens, E.; Cao, H.; Noguchi, A.; Ivasenko, O.; Fang, Y.; Tahara, K.; Tobe, Y.; De Feyter, S. *Chem. Commun.* **2015**, *51*, 4766.

Chapter VI Single-Molecule Manipulation of $Tb^{III}(oep)_2$ on Au(111) by STM

6-1 Introduction

Molecular spintronics is one of the promising fields for the studies of future advanced devices. In this field controlling the spin distribution precisely on a surface is very important and molecular self-assembly is one of the best ways to order spins in a molecule on a surface.[1,2] To observe supramolecular structure on a surface, scanning tunneling microscopy (STM) is powerful and promising tool. STM can also reveal spin information on the surface with atomic resolution through the detection of the Kondo resonance which is caused by the interactions between conduction electrons and localized spin[3], and manipulate the molecular properties.[2,4,5] The research of the Kondo resonance using STM has started for the observation of single magnetic atoms,[6-8] which were followed by that for adsorbed molecules.[1,2,4,5,9-15]

From the view point of materials, on the other hand, single-molecule magnets (SMMs) are attracting a great deal of attention in the field of molecular spintronics now.[16-19] With a strong magnetic anisotropy to an easy axis, SMMs behave like tiny magnets at single molecular level and can store the information of the spin direction for a certain period of time. Indeed, studies for spintronics devices with SMMs at single or several molecular levels have been reported in these days.[20,21] Furthermore studies of SMMs in the film state for future devices have demonstrated that SMM property can be maintained even in the film state.[22,23]

In our previous study we succeeded in manipulating an unpaired spin in a π-orbital of a phthalocyanine (Pc) based Tb^{III} double-decker ($Tb^{III}(Pc)_2$) SMMs in the film with a single molecular precision by STM.[4,24] We detected the spin state by the disappearance and reappearance of the Kondo resonance. However, it is not yet achieved to control SMM property on the surface in this system because the interaction between the π radical electron and Tb^{III} center is not enough strong to perturb the SMM behavior. We thought switching property of SMMs and controlling intermolecular interaction was very important to the further development for molecular spintronics. To achieve such higher intelligent systems, well-designed molecules are needed.

Here in this article we propose a 2,3,7,8,12,13,17,18-octaethylporphyrin (OEP)-Tb^{III} double-decker complex as a new attractive molecule for molecular spin patterning on the surface. This molecule has three main advantages. First advantage is unique proton-induced switching of SMM property (Scheme 1).[25,26] Only porphyrin based Tb^{III} double-decker complex can show this specific magnetic switching. This molecule can also make stable 2D supramolecular structure on the surface.[26] Based on these advantages we try to create a pattern of the SMM assembly in the film and to achieve new Kondo feature. First we make molecular film of a protonated form OEP-Tb^{III} double-decker complex (Tb^{III}(OEPH)(OEP)) , which does not show SMM behavior. Then we try dehydrogenation of Tb^{III}(OEPH)(OEP), and to make a radical form OEP-Tb^{III} double-decker complex ($Tb^{III}(OEP)_2$), which shows SMM property with a single molecular precision by injecting tunneling current from a STM tip (Scheme 1).[22,23] By this technique patterning of SMMs at the designed site in the film can be achieved.

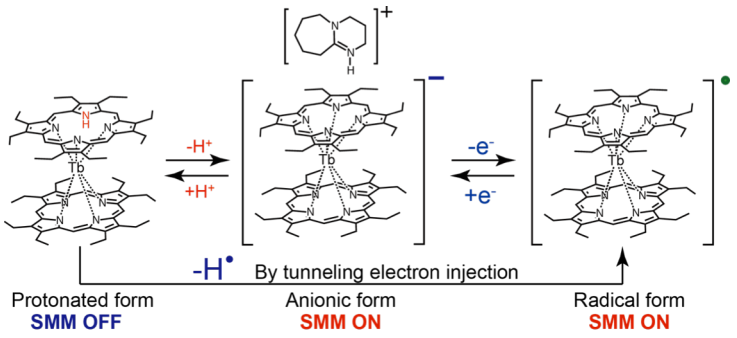

Scheme 1. Three different electronic structures of the 2, 3, 7, 8, 12, 13, 17, 18-octaethylporphyrin(OEP)-Tb^{III} double-decker complex.

6-2 Experimental

Tb^{III}(OEPH)(OEP) and $Tb^{III}(OEP)_2$ were obtained by the previous reported procedure[26]. All STM and STS measurement were done at cryogenic temperatures (4.7 K) in an ultrahigh vacuum (UHV). A gold single crystal was used for the substrate and its Au(111) surface was prepared by Ar^+ sputtering and annealing. The molecules were deposited on a clean Au(111) surface kept at room temperature by using a sublimation method in ultra-high vacuum. STS spectra were obtained using a lock-in amplifier technique with a modulation voltage of 1 mV.

First-principle calculations were performed by using VASP code, employing a plane wave basis set and PAW potentials in order to describe the behavior of the valence electrons.[27,28] A generalized gradient Perdew-Burke-Ernzerhof (PBE) exchange-correlation was used.[29]

6-3 Results and Discussions

Figure 1(a) shows the structure of the (oepH) ligand, where an H atom attached to an N atom is colored light red. The ligand of OEP corresponds to one without the H atom. The profile view of Tb^{III}(oepH)(oep) is sketched in Fig. 1(b). The azimuthal rotation angles between ligands of $Tb^{III}(oep)_2$ and Tb^{III}(oepH)(oep), determined from our previous research, are 45° and 36° respectively for an anionic form $[Tb^{III}(tpp)_2]^-$ and a protonated form Tb^{III}(tppH)(tpp), respectively[25]. Figures 1(c) and 1(d) show the occupied-state STM images of $Tb^{III}(oep)_2$ and Tb^{III}(oepH)(oep) molecules, respectively, adsorbed on Au(111). For $Tb^{III}(oep)_2$, eight protruded lobes are evenly placed in the ligand position, which shows an intriguing difference from the reported four-lobe image of a single-decker porphyrine-family molecule of TBrPP-Co [10]. On the other hand, two lobes of Tb^{III}(oepH)(oep) are missing from the evenly spaced eight lobes. Figures 1(e) and 1(f) are simulated STM images with density functional theory (DFT) calculations for the occupied state for $Tb^{III}(oep)_2$ and Tb^{III}(oepH)(oep), respectively, where the molecule as that in Fig. 1(a). Two missing lobes are reproduced in Fig. 1(f) near the position of the H atom.

When the coverage of Tb^{III}(oepH)(oep) molecules on Au(111) increases, the molecules form an ordered assembly. Figures 1(g) and 1(h) show the images of a film of Tb^{III}(oepH)(oep) obtained for the unoccupied and occupied states, respectively, on the same area of the surface. A single molecule appears to protrude out of the rest of the film in Fig. 1(g) (Note that the contrast is not obvious in the image of the unoccupied state Fig. 1(h)). We assign the protruded molecule to a $Tb^{III}(oep)_2$ molecule accidentally mixed in the Tb^{III}(oepH)(oep) film for the following reasons.

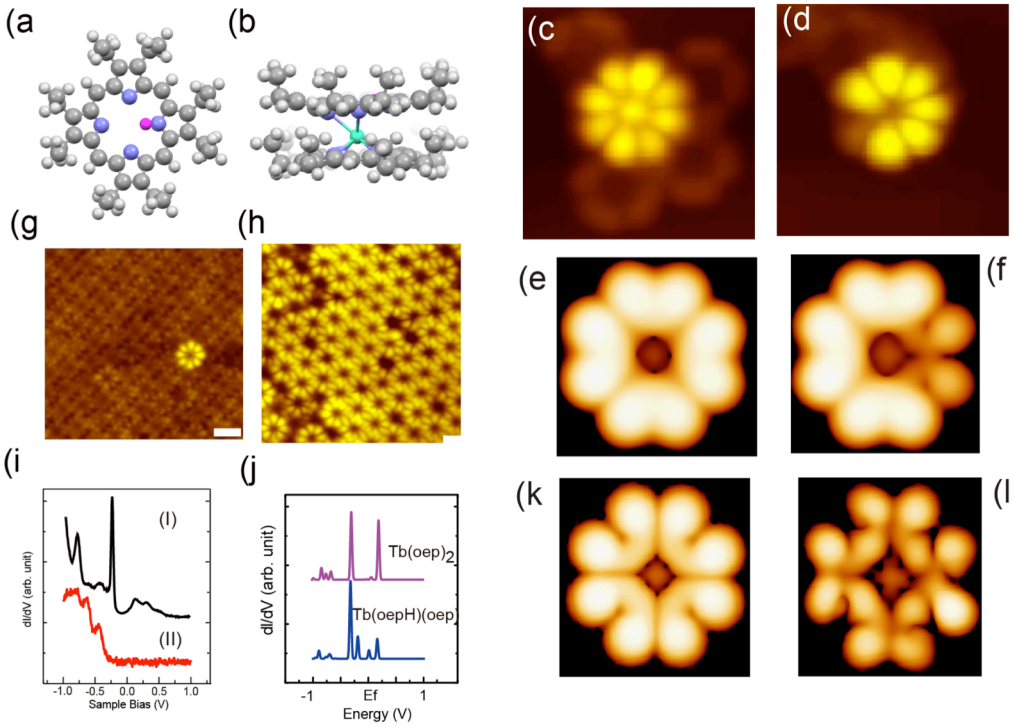

Figure 1. (a) Model of (oepH) ligand from top. Light red atom indicates H atom. (b) Side view of Tb^{III}(oepH)(oep). (c),(d) STM images of an isolated molecule of (c) $Tb^{III}(oep)_2$, and (d) Tb^{III}(oepH)(oep) on Au(111). V_s = -0.8 V, I_t = 0.2 nA. (e)(f)(k)(l), Simulated STM images of $Tb^{III}(oep)_2$, ((e) occupied, and (k) unoccupied) and Tb^{III}(oepH)(oep), ((f) occupied, and (l) unoccupied). (g)(h) STM images of Tb^{III}(oepH)(oep) film on Au(111) with (g) V_s = 0.8 V and (H) V_s=−0.8 V. I_t = 0.2 nA and scale bar = 2.0 nm. (i) STS spectra of (I) the protruded molecule (II) the molecule in the rest of the film in Fig. 1(g). (j) Calculated LDOS of $Tb^{III}(oep)_2$ and Tb^{III}(oepH)(oep).

First, we compare scanning tunneling spectroscopy (STS) data and result of the theoretical calculation of the local density of states (LDOS) for the protruded and non-protruded molecules. The STS spectra measured for the former and the latter are compared in Fig. 1(i). Almost no features of the latter molecule are observed in the $V_s > 0$ region. The calculated LDOS of the $Tb^{III}(oep)_2$ and the Tb^{III}(oepH)(oep) molecules at the N atom, to which the H atom is attached in the latter molecule, are compared in Fig. 1(j). The LDOS of the Tb^{III}(oepH)(oep) molecule in the unoccupied state is significantly smaller than that of the $Tb^{III}(oep)_2$ molecule, which can

explain the fewer features in the STS. Second, simulated images for the $Tb^{III}(oep)_2$ and $Tb^{III}(oepH)(oep)$ molecules, shown in Figs. 1(k) and 1(l), respectively, indicate a more protruded STM image of $Tb^{III}(oep)_2$. Further evidence of the assignment of the protruding molecule in the $Tb^{III}(oepH)(oep)$ film to $Tb^{III}(oep)_2$, which is shown in Fig. 1(g) of the main manuscript, could be obtained by measuring the rotation angle of the upper ligand. We can see the inner molecular structures of both the low-contrast $Tb^{III}(oepH)(oep)$ molecule and the protruding molecule in Fig. 2. We drew symmetry lines for both molecules, connecting the center of the lobes in the diagonal positions. The white line for the $Tb^{III}(oepH)(oep)$ molecule is rotated by ~10° from the green line for the protruding one. In our previous study, the top ligands should be rotated by ~9° from each other for the two molecules of $Tb^{III}(oepH)(oep)$ and $Tb^{III}(oep)_2$, if the lower ligand is fixed with respect to the substrate. This angle is close to the measured one, which is further evidence of the assignment of the protruding molecule to $Tb^{III}(oep)_2$. In addition, we could confirm the increase in the number of protruding molecules in the film, when we deposited using a source in which $Tb^{III}(oep)_2$ molecules are intentionally mixed with $Tb^{III}(oepH)(oep)$ molecules. The proportion varied almost linearly with the mixture

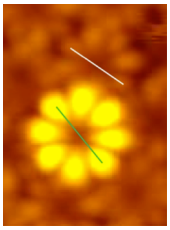

Figure 2. Comparison of the symmetry lines connecting diagonal robes of the $Tb^{III}(oepH)(oep)$ molecule with a lower height and the protruding molecule .

ratio.

We now discuss the conformational and chemical changes in the molecule when the tunneling electrons are injected into the $Tb^{III}(oepH)(oep)$ molecule. We first observed a hopping of the H atom attached to the N atom when electrons at 1.5 eV were injected into the molecule (see Figure 3). When we injected tunneling electrons into an isolated molecule of $Tb^{III}(oepH)(oep)$, the hopping of the H atom attached to the N atom was induced. We observed telegraphic noise in the tunneling current when the tip position was fixed at the position of a

ligand of the isolated Tb^{III}(oepH)(oep) molecule and the tunneling current was measured for V_s of 1.5 V. The telegraphic noise, shown in Figures 3(b) and (c), was composed of three staircases. Whenever the current corresponding to the three groups changed, we observed the rotation of the lower area of the molecule, as marked by arrows in Fig. 3(a). This can be best explained by a model in which there occurs a change in the H bonding site to one between the four equivalent positions by the injection of the tunneling electrons.

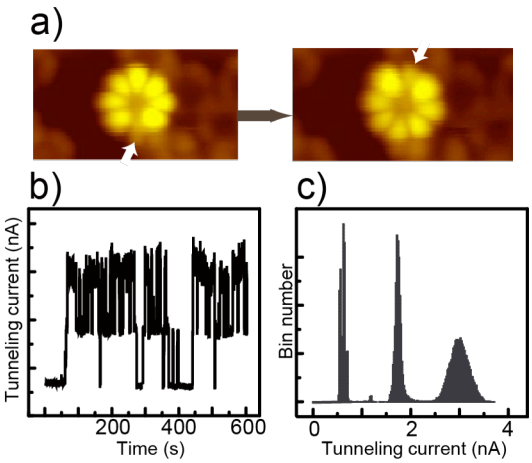

Figure 3. (a) Topographic image of the rotation of the missing lobe when the tunneling current is injected into an isolated Tb^{III}(oepH)(oep) molecule. (b) Variation in the tunneling current variation induced the rotation of (a). (c) Histogram of the residing time at the specified tunneling current.

When the energy of the injected electrons exceeded 1.5 eV, the target molecule changed into a protruded one in comparison with the rest of the molecules in the film. Two models to explain the changes caused by electron injection are shown in Fig. 4(a), which shows the detachment of a hydrogen atom and ethyl removal on the left- and right-hand sides, respectively. For the energy range 1.5-2.5 eV, the detachment of a hydrogen atom was dominant. The change in the STM image due to tunneling electron injection is shown in Fig. 4(b). The target molecule marked by a blue circle changed into a protruded molecule. The outlook of the protruded peak was similar to $Tb^{III}(oep)_2$ in the Tb^{III}(oepH)(oep) film (see Fig. 1(g)). The rotation of the upper ligand is one of the evidences of dehydrogenation. The lobes of this molecule, before and after the dehydrogenation process, are numbered from 1 to 8 (Fig. 4(c)). The line connecting lobes 1

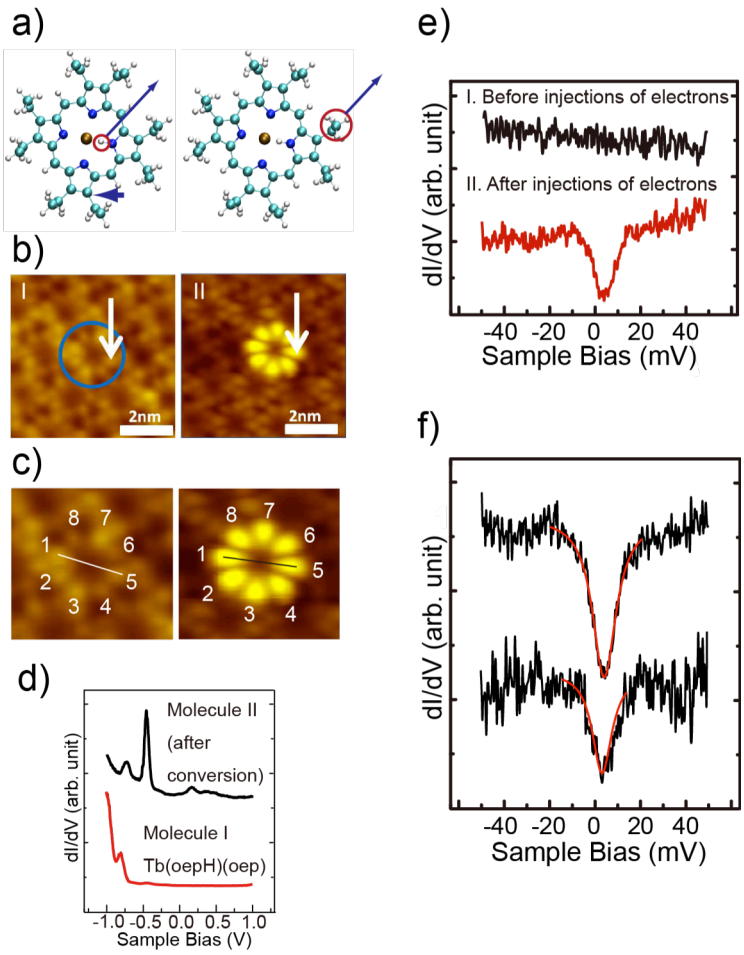

Figure 4. (a) Two models of Tb^{III}(oepH)(oep) molecule dissociation using a tunneling electron. Detachment of a hydrogen atom (left-hand side) and ethyl removal (right-hand side) from Tb^{III}(oepH)(oep) molecule. Only the upper ligand is shown. (b) STM images before (I) and after (II) injection of electrons from STM tip to Tb^{III}(oepH)(oep). (c) Measurement of the azimuthal angle of the upper ligand; a comparison of the values before and after the conversion is shown. (d) Comparison of the STS spectra of the molecules of I and II. Though there is a small shift in the energies, the shapes indicate that molecule II of Fig. 4(d) is $Tb^{III}(OEP)_2$. The shifts in the energies are likely owing to the final-state effect. (e) Appearance of the Fano dip of the Kondo resonance. (f) Comparison of Fano dip at the ligand (upper) and the center of the molecule (lower). The fitting results are highlighted by red lines.

and 5 is rotated by ~9° after the lobes have been manipulated with respect to each other. Our previous study suggested that the azimuthal angles of $Tb^{III}(oep)_2$ and Tb^{III}(oepH)(oep) are different by ~9°, which is close to the rotation angle seen in Fig. 4(c). This is further evidence

that hydrogenation did occur after the injection of tunneling electrons. Additional evidence was obtained by comparing the STS spectra of the Tb^{III}(oepH)(oep) and $Tb^{III}(oep)_2$ molecules (Fig. 1(i)) with those for the molecules of I and II shown in Fig. 4(d). Though there was a small shift in the energies, the shapes indicated that molecule II in Fig. 4(b) is $Tb^{III}(oep)_2$. The shifts in the energies are likely attributable to the final-state effect.

The conversion of the molecule from Tb^{III}(oepH)(oep) to $Tb^{III}(oep)_2$ can be clearly seen in its spin properties. The STS spectra obtained in the vicinity of the Fermi level examined for the molecules in Fig. 4(b), at the arrows of I and II, are shown in Fig. 4(e). Only $Tb^{III}(oep)_2$ shows a sharp dip near the Fermi level, and no feature is observed for the entire Tb^{III}(oepH)(oep) molecule. For the $Tb^{III}(oep)_2$ molecule, we compare the spectra obtained at the lobe position and the center in Fig. 4(f). The dip features can be best analyzed using Fano resonance through the following equation [30,31]:

$$dI(V)/dV \propto \frac{\rho_0(\varepsilon+q)^2}{\varepsilon^2+1}, \quad \varepsilon = \frac{eV-\varepsilon_0}{\Gamma} \text{----------(1)}$$

where q is the Fano parameter, e_0 is the peak position, and G is the width parameter. The shapes of the spectra change through parameter q. The fitting results are indicated by red solid curves in Fig. 4(f). As shown in Figure 5, we assigned the dip feature to the Kondo feature appearing with the Fano dip shape by examining the temperature dependence. In order to prove that zero-bias peaks (ZBPs) originate from Kondo resonance, we examined the change in the peak widths with the sample temperature. The peaks were fitted using Fano functions; the fitted curves are plotted in Figure for the dip (peak) observed for the deprotonated (ethyl-detached) molecule. Nagaoka et al. have suggested a function to describe the dependence of the Kondo peak width (W) on the sample temperature (T) using Fermi liquid theory: [31] (Note that W corresponds to 2Γ, where Γ is the fitted parameter of the Fano function mentioned in the main text)

$$W(\mathrm{T}) = 2\sqrt{(\pi k_B T)^2 + 2(k_B T_K)^2} \quad \text{---------} (2)$$

where k_B is the Boltzmann constant and T_K is the Kondo temperature.

First, the zero-bias features measured for four sample temperatures were analyzed using Fano functions (these are shown in the left-hand panel), which gave W(T) for each temperature.

Next, the W(T) values were plotted as a function of the temperature (see the right-hand panel) and then fitted using Formula (2). The result is shown by the red solid curve in the plot. The curves are for the deprotonated and ethyl-detached molecules in Fig. 5(a) and 5(b). The fitting curves for the W vs. temperature relationship reproduce the measured points well within the accuracy of the error bars. This rationalizes the assignment of both the dip and the peak features to the Kondo resonance. T_K was determined to be 37 K (105 K) for the deprotonated (ethyl-detached) molecule.

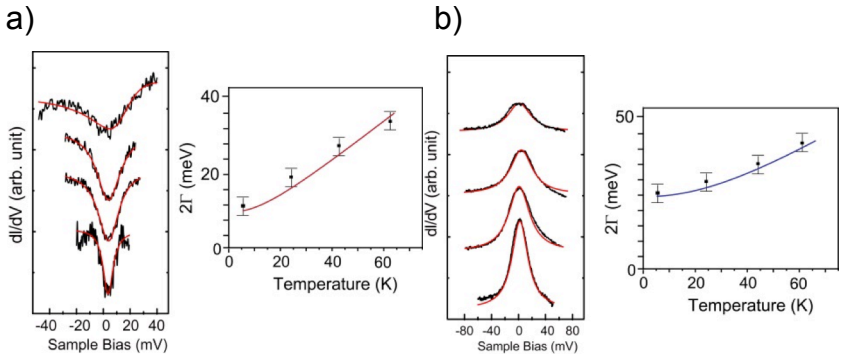

Figure 5. (a) Temperature dependence of the zero-bias features measured in the region 4.7–64 K for the deprotonated molecule. The peak width (2Γ) vs. temperature curve is also plotted in the right-hand panel along with error bars. The solid curve indicates the curve fitted using Formula (1) stated in the text, in which T_K is the fitting parameter. (b) Same as Fig. 5(a), but measured for the ethyl-detached molecule as the peak near the Fermi level.

The parameters of the fitting curves for the spectra obtained at the ligand and the center positions were similar, except that the amplitude observed for the former was 40 % lower than that for the latter. We estimated the parameters of $T_K \sim 37$ K and q ~ 0.03. *q* indicates the extent to which the tunneling current has the dominant path to the substrate instead of through the molecule. The Fano dip Kondo has been reported for the porphyrin family of the TBrPP-Co molecule *(13)*,[10] but $Tb^{III}(Pc)_2$ shows the Kondo peak.[4] For the Tb^{III}(oepH)(oep) molecule, Kondo resonance was observed neither at the lobe position nor at the center of the molecule, despite the existence of the spin of the Tb^{III} ion (the molecule was non-SMM, and the Tb atom had a spin of $J = 6$) [26]. From this result, we can conclude that the Kondo feature observed for the $Tb^{III}(oep)_2$ molecule was derived from an unpaired π spin of the ligand.

We calculated the spin-resolved partial density of states (PDOS) for several configurations of OEP complexes. In the upper two plots of Fig. 6(b), the results calculated for Tb^{III}(oepH)(oep) and $Tb^{III}(oep)_2$ molecules at the carbon atoms marked by arrows in Fig. 4(a) are shown. In these, the disappearance (appearance) of the unpaired π spin of the former (latter) molecule is reproduced, and can account for the behavior of the Kondo feature. The absence of the Kondo feature at the Tb position is likely because T_K for the Tb ion is too low to be detected at 4.7 K [4]. Even though we could not access the spin property of the Tb^{III} ion, it is obvious that we can create the SMM $Tb^{III}(oep)_2$ in the matrix of non-SMM Tb^{III}(oepH)(oep) molecules through a comparison with the bulk experiments [26]. This can be accomplished with high spatial precision in the tunneling electron that permits any shape of SMM assembly to be patterned. An example is shown in Fig. 6(a). Starting from a single converted $Tb^{III}(oep)_2$ in the matrix of non-SMM Tb^{III}(oepH)(oep) in the upper panel of Fig. 6(a), two parallel chains of SMM $Tb^{III}(oep)_2$ are created in the lower panel.

6-4 Conclusions

In this study, we showed the molecular patterning of SMMs at a designated site on a Tb^{III}(oepH)(oep) film with a sub-molecular precision. We observed several phenomena according to the different strength of the voltage of electron injection, that is, only dehydrogenation of Tb^{III}(oepH)(oep) molecules were caused by injecting tunneling electrons whose energy exceeds 1.5 eV. The $Tb^{III}(oep)_2$ molecule showed a Fano dip of the Kondo resonance originated from the unpaired spin of a π orbital. We also succeeded in patterning the $Tb^{III}(oep)_2$ molecules successively by continuous electron injection.

References

(1) DiLullo, A.; Chang, S. H.; Baadji, N.; Clark, K.; Klockner, J. P.; Prosenc, M. H.; Sanvito, S.; Wiesendanger, R.; Hoffmann, G.; Hla, S. W. *Nano Lett.* **2012**, *12*, 3174.

(2) Komeda, T.; Isshiki, H.; Liu, J.; Katoh, K.; Shirakata, M.; Breedlove, B. K.; Yamashita, M. *Acs Nano* **2013**, *7*, 1092.

(3) Kondo, J. *Phys. Rev.* **1968**, *169*, 437.

(4) Komeda, T.; Isshiki, H.; Liu, J.; Zhang, Y.-F.; Lorente, N. s.; Katoh, K.; Breedlove, B. K.; Yamashita, M. *Nat. Commun.* **2011**, *2*, 217.

(5) Komeda, T.; Isshiki, H.; Liu, J.; Katoh, K.; Yamashita, M. *ACS Nano* **2014**, *8*, 4866.

(6) Li, J. T.; Schneider, W. D.; Berndt, R.; Delley, B. *Phys. Rev. Lett.* **1998**, *80*, 2893.

(7) Madhavan, V.; Chen, W.; Jamneala, T.; Crommie, M. F.; Wingreen, N. S. *Science* **1998**, *280*, 567.

(8) Neel, N.; Kroger, J.; Limot, L.; Frederiksen, T.; Brandbyge, M.; Berndt, R. *Phys. Rev. Lett.* **2007**, *98*.

(9) Zhao, A. D.; Li, Q. X.; Chen, L.; Xiang, H. J.; Wang, W. H.; Pan, S.; Wang, B.; Xiao, X. D.; Yang, J. L.; Hou, J. G.; Zhu, Q. S. *Science* **2005**, *309*, 1542.

(10) Iancu, V.; Deshpande, A.; Hla, S. W. *Nano Lett.* **2006**, *6*, 820.

(11) Fernandez-Torrente, I.; Franke, K. J.; Pascual, J. I. *Phys. Rev. Lett.* **2008**, *101*.

(12) Cho, S.; Lim, J. M.; Hiroto, S.; Kim, P.; Shinokubo, H.; Osuka, A.; Kim, D. *J. Am. Chem. Soc.* **2009**, *131*, 6412.

(13) Li, Z. Y.; Li, B.; Yang, J. L.; Hou, J. G. *Acc. Chem. Res.* **2010**, *43*, 954.

(14) Mugarza, A.; Krull, C.; Robles, R.; Stepanow, S.; Ceballos, G.; Gambardella, P. *Nat. Commun.* **2011**, *2*.

(15) Tsukahara, N.; Shiraki, S.; Itou, S.; Ohta, N.; Takagi, N.; Kawai, M. *Phys. Rev. Lett.* **2011**, *106*.

(16) Christou, G.; Gatteschi, D.; Hendrickson, D. N.; Sessoli, R. *Mrs Bulletin* **2000**, *25*, 66.

(17) Bogani, L.; Wernsdorfer, W. *Nat. Mater.* **2008**, *7*, 179.

(18) Rinehart, J. D.; Long, J. R. *Chem. Sci.* **2011**, *2*, 2078.

(19) Woodruff, D. N.; Winpenny, R. E. P.; Layfield, R. A. *Chem. Rev.* **2013**, *113*, 5110.

(20) Vincent, R.; Klyatskaya, S.; Ruben, M.; Wernsdorfer, W.; Balestro, F. *Nature* **2012**, *488*, 357.

(21) Ganzhorn, M.; Klyatskaya, S.; Ruben, M.; Wernsdorfer, W. *Acs Nano* **2013**, *7*, 6225.

(22) Cornia, A.; Mannini, M.; Sainctavit, P.; Sessoli, R. *Chem. Soc. Rev.* **2011**, *40*, 3076.

(23) Domingo, N.; Bellido, E.; Ruiz-Molina, D. *Chem. Soc. Rev.* **2012**, *41*, 258.

(24) Ishikawa, N.; Sugita, M.; Ishikawa, T.; Koshihara, S.; Kaizu, Y. *J. Am. Chem. Soc.* **2003**, *125*, 8694.

(25) Tanaka, D.; Inose, T.; Tanaka, H.; Lee, S.; Ishikawa, N.; Ogawa, T. *Chem. Commun.* **2012**, *48*, 7796.

(26) Inose, T.; Tanaka, D.; Tanaka, H.; Ivasenko, O.; Nagata, T.; Ohta, Y.; De Feyter, S.; Ishikawa, N.; Ogawa, T. *Chem. Eur. J.* **2014**, *20*, 11362.

(27) Kresse, G.; Furthmuller, J. *Phys. Rev. B* **1996**, *54*, 11169.

(28) Kresse, G.; Joubert, D. *Phys. Rev. B* **1999**, *59*, 1758.

(29) Perdew, J. P.; Burke, K.; Ernzerhof, M. *Phys. Rev. Lett.* **1996**, *77*, 3865.

(30) Fano, U. *Phys. Rev.* **1961**, *124*, 1866.

(31) Nagaoka, K.; Jamneala, T.; Grobis, M.; Crommie, M. F. *Phys. Rev. Lett.* **2002**, *88*, 077205.

Chapter VII Conclusions

In this thesis new approaches to realize future molecular spintronic devices were suggested by using porphyrin based Tb^{III} double-decker SMMs.

First both a protonated form and an anionic form tetraphenylporphyrin double-decker complexes were synthesized. The molecular symmetry of a protonated form double-decker complex was lower than that of an anionic form double-decker complex. Such difference of molecular symmetry affects the SMM properties of porphyrin double-decker complexes and only an anionic form double-decker showed a SMM property in bulk state by the ac magnetic susceptibility measurement. Because Tb^{III} ion is non-Kramers ion and axial crystal symmetry is very important to keep a degenerate state, a protonated form double-decker complex with lower molecular symmetry did not show the SMM property. From this study drastic switching of SMM property by proton desorption was realized. Such drastic SMM switching was achieved for the first time by using porphyrin. Moreover a porphyrin double-decker complex with quinone dyad was designed to achieve the SMM switching in solid state. In this molecule it is expected to occur proton coupled electron transfer (PCET). Energy barrier between the ground state of both before and after PCET and transition state of a porphyrin with quinone dyad was estimated from TD-DFT calculations. From the calculation results, it was suggested the possibility of PCET in this double-decker complex.

To investigate 2D supramolecular structure of SMMs, three different electronic structures -a protonated, an anionic, and a radical form- octaethylporphyrin double-decker complexes were synthesized. From the magnetic measurement, similar SMM properties to tetraphenylporphyrin double-decker complexes were observed and proton-induced SMM switching was also possible of octaethylporphyrin double-decker complexes. STM measurement revealed that three double-decker complexes formed stable hexagonal packing 2D supramolecular structure on HOPG. Moreover new method to fabricate 2D structure of SMMs was suggested by using DBA as a host molecule on a surface. A radical form octaethylporphyrin double-decker complex was

used as a guest molecule and concentration dependence of a guest molecule was observed. This method can be used to control SMM density on a surface precisely.

Finally single-molecule manipulation of octaethylporphyrin double-decker complexes on Au(111) was demonstrated by UHV-STM. The electronic state of octaethylporphyrin double-decker complex was changed at single-molecule level from a protonated form which does not show the SMM property to a radical form which shows the SMM property by injecting electrons from a STM tip.

From these studies fabricating ordered 2D supramolecular structure of porphyrin double-decker SMMs was possible. This result is very important to find the most suitable 2D structure for future SMM devices. Furthermore basic perception to control the SMM property on a surface was suggested by changing the electronic structure of octaethylporphyrin double-decker complex at single-molecule level. This valuable progress was achieved by using porphyrin double-decker complex with unique-induced SMM property. These results can be groundwork for future SMM devices.

List of Publications

Chapter II

D. Tanaka, T. Inose, H. Tanaka, S. Lee, N. Ishikawa, T. Ogawa

Proton-induced Switching of the Single Molecule Magnetic Properties of a Porphyrin Based Tb^{III} Double-decker Complex

Chem. Commun., *48*, 7796-7798, **2012**

Chapter III

T. Inose, D. Tanaka, T. Ogawa

Computational Investigation of a Photo-switchable Single-Molecule Magnet Based on a Porphyrin Terbium Double-Decker Complex

Heterocycles, *86*, 1549-1554, **2012**

Chapter IV

T. Inose, D. Tanaka, H. Tanaka, O. Ivasenko, T. Nagata, Y. Ohta, S. De Feyter, N. Ishikawa, T. Ogawa

Switching of Single-Molecule Magnetic Properties of Tb^{III}-Porphyrin Double-Decker Complexes and Observation of Their Supramolecular Structures on a Carbon Surface

Chem. Eur. J., *20*, 11362-11369, **2014**.

Chapter V

T. Inose, D. Tanaka, O. Ivasenko, K. Tahara, S. De Feyter, Y. Tobe, H. Tanaka, T. Ogawa

Fabricating a New Supramolecular Structure of Tb^{III}-Porphyrin Double-Decker Single-Molecule Magnets on a Carbon Surface by Two-Component Network

To be submitted.

Chapter VI

T. Inose, D. Tanaka, L. Jie, M. Kajihara, P. Mishra, T. Ogawa, T. Komeda

Patterning for Assembly of Single-molecule Magnets of Porphyrin-Tb^{III} Double-decker Complex

To be submitted.

Other Publications

(1) D. Tanaka, T. Inose, S. Shimono, H. Tanaka, T. Tamaki, A. I. A. Abd El-Mageed, A. K. F. Dyab, N. Ishikawa, T. Ogawa

Surface Self-Assembly of Trans-Substituted Porphyrin Double-Decker Complexes Exhibiting Slow Magnetic Relaxation

e-Journal of Surface Science and Nanotechnology, *12*, 124-128, **2014**

(2) D. Tanaka, N. Aketa, H. Tanaka, T. Tamaki, T. Inose, T. Akai, H. Toyama, O. Sakata, Hiroo Tajiri, T. Ogawa

Thin Films of Spin-crossover Coordination Polymers with Large Thermal Hysteresis Loops Prepared by Nanoparticle Spin Coating

Chem. Commun., *50*, 10074-10077, **2014**.

(3) D. Tanaka, N. Sumitani, T. Inose, H. Tanaka, N. Ishikawa, and T. Ogawa[4]

Effect of Protonation on the Single-Molecule-Magnet Behavior of a Mixed (Phthalocyaninato)(porphyrinato) Terbium Double-Decker Complex

Chem. Lett., *44*, 668-670, **2015**.